

# Nanostructured Carbon Materials

Guest Editors: Myoung-Woon Moon, Ho-Young Kim, Aiyong Wang,  
and Ashkan Vaziri





---

# **Nanostructured Carbon Materials**

Journal of Nanomaterials

---

## **Nanostructured Carbon Materials**

Guest Editors: Myoung-Woon Moon, Ho-Young Kim,  
Aiyang Wang, and Ashkan Vaziri



---

Copyright © 2015 Hindawi Publishing Corporation. All rights reserved.

This is a special issue published in "Journal of Nanomaterials." All articles are open access articles distributed under the Creative Commons Attribution License, which permits unrestricted use, distribution, and reproduction in any medium, provided the original work is properly cited.

## Editorial Board

Domenico Acierno, Italy  
Katerina Aifantis, USA  
Sheikh Akbar, USA  
Nageh K. Allam, USA  
Margarida Amaral, Portugal  
Jordi Arbiol, Spain  
Raul Arenal, Spain  
Ilaria Armentano, Italy  
Lavinia Balan, France  
Thierry Baron, France  
Andrew R. Barron, USA  
Hongbin Bei, USA  
Stefano Bellucci, Italy  
Enrico Bergamaschi, Italy  
D. Bhattacharyya, New Zealand  
Giovanni Bongiovanni, Italy  
Theodorian Borca-Tasciuc, USA  
Mohamed Bououdina, Bahrain  
Torsten Brezesinski, Germany  
C. Jeffrey Brinker, USA  
Christian Brosseau, France  
Yibing Cai, China  
Chuanbao Cao, China  
Victor M. Castao, Mexico  
Albano Cavaleiro, Portugal  
Bhanu P. S. Chauhan, USA  
Yuan Chen, Singapore  
Wei Chen, China  
Tupei Chen, Singapore  
Shafiul Chowdhury, USA  
Kwang-Leong Choy, UK  
Jin-Ho Choy, Korea  
Yu-Lun Chueh, Taiwan  
Elisabetta Comini, Italy  
Giuseppe Compagnini, Italy  
David Cornu, France  
Miguel Correa-Duarte, Spain  
P. Davide Cozzoli, Italy  
Majid Darroudi, Iran  
Shadi A. Dayeh, USA  
Luca Deseri, USA  
Yong Ding, USA  
Bin Dong, China  
Zehra Durmus, Turkey  
Joydeep Dutta, Oman

Ali Eftekhari, USA  
Samy El-Shall, USA  
Farid El-Tantawy, Egypt  
Ovidiu Ersen, France  
Claude Estournès, France  
Andrea Falqui, Saudi Arabia  
Xiaosheng Fang, China  
Bo Feng, China  
Matteo Ferroni, Italy  
Wolfgang Fritzsche, Germany  
Alan Fuchs, USA  
Peng Gao, China  
Miguel A. Garcia, Spain  
Siddhartha Ghosh, Singapore  
P. K. Giri, India  
Russell E. Gorga, USA  
Jihua Gou, USA  
Alexander Govorov, USA  
Jean M. Greneche, France  
Changzhi Gu, China  
Lin Guo, China  
John Zhanhu Guo, USA  
Smrati Gupta, Germany  
K. Hamad-Schifferli, USA  
Michael Harris, USA  
Jr-Hau He, Taiwan  
Nguyen D. Hoa, Vietnam  
Michael Z. Hu, USA  
Shaoming Huang, China  
Nay Ming Huang, Malaysia  
Qing Huang, China  
David Hui, USA  
Zafar Iqbal, USA  
Balachandran Jeyadevan, Japan  
Xin Jiang, Germany  
Rakesh Joshi, Australia  
Myung-Hwa Jung, Korea  
Jeong-won Kang, Korea  
Hassan Karimi-Maleh, Iran  
Antonios Kelarakis, UK  
Alireza Khataee, Iran  
Ali Khorsand Zak, Iran  
Dojin Kim, Korea  
Wonbaek Kim, Korea  
Philippe Knauth, France

Ralph Krupke, Germany  
Christian Kbel, Germany  
Sanjeev Kumar, India  
Sushil Kumar, India  
Prashant Kumar, UK  
Subrata Kundu, India  
Michele Laus, Italy  
Eric Le Bourhis, France  
Burtrand Lee, USA  
Jun Li, Singapore  
Meiyong Liao, Japan  
Silvia Licocchia, Italy  
Wei Lin, USA  
Jun Liu, USA  
Zainovia Lockman, Malaysia  
Songwei Lu, USA  
Jue Lu, USA  
Ed Ma, USA  
Malik Maaza, South Africa  
Lutz Mädler, Germany  
Gaurav Mago, USA  
Morteza Mahmoudi, Iran  
Mohammad A. Malik, UK  
Devanesan Mangalaraj, India  
Sanjay R. Mathur, Germany  
Paulo Cesar Morais, Brazil  
Mahendra A. More, India  
Paul Munroe, Australia  
Jae-Min Myoung, Korea  
Rajesh R. Naik, USA  
Albert Nasibulin, Russia  
Toshiaki Natsuki, Japan  
Koichi Niihara, Japan  
Sherine Obare, USA  
Won-Chun Oh, Republic of Korea  
Atsuto Okamoto, Japan  
Abdelwahab Omri, Canada  
Ungyu Paik, Republic of Korea  
Edward A. Payzant, USA  
Ton Peijs, UK  
O. Perales-Pérez, Puerto Rico  
Wenxiu Que, China  
Peter Reiss, France  
Orlando Rojas, USA  
Marco Rossi, Italy



---

Cengiz S. Ozkan, USA  
Vladimir Šepelák, Germany  
Huaiyu Shao, Japan  
Prashant Sharma, USA  
Donglu Shi, USA  
Bhanu P. Singh, India  
Surinder Singh, USA  
Vladimir Sivakov, Germany  
Yanlin Song, China  
Ashok Sood, USA  
Marinella Striccoli, Italy  
Jing Sun, China  
Xuping Sun, Saudi Arabia  
Ashok K. Sundramoorthy, USA

Sabine Szunerits, France  
Nyan-Hwa Tai, Taiwan  
Bo Tan, Canada  
Ion Tiginyanu, Moldova  
Valeri P. Tolstoy, Russia  
Muhammet S. Toprak, Sweden  
Ramon Torrecillas, Spain  
Takuya Tsuzuki, Australia  
Tamer Uyar, Turkey  
Bala Vaidhyanathan, UK  
Luca Valentini, Italy  
Rajender S. Varma, USA  
Antonio Villaverde, Spain  
Ajayan Vinu, Australia

Shiren Wang, USA  
Ruibing Wang, Macau  
Yong Wang, USA  
Magnus Willander, Sweden  
Zhi Li Xiao, USA  
Ping Xiao, UK  
Yangchuan Xing, USA  
Doron Yadlovker, Israel  
Piaoping Yang, China  
Yoke K. Yap, USA  
Ramin Yousefi, Iran  
William W. Yu, USA  
Kui Yu, Canada  
Renyun Zhang, Sweden

## Contents

**Nanostructured Carbon Materials**, Myoung-Woon Moon, Ho-Young Kim, Aiyang Wang,  
and Ashkan Vaziri  
Volume 2015, Article ID 916834, 2 pages

**Preparation and Study of Electromagnetic Interference Shielding Materials Comprised of Ni-Co Coated on Web-Like Biocarbon Nanofibers via Electroless Deposition**, Xiaohu Huang, Bo Dai, Yong Ren, Jing Xu, and Pei Zhu  
Volume 2015, Article ID 320306, 7 pages

**Enhancement of Gas Sensing Characteristics of Multiwalled Carbon Nanotubes by CF<sub>4</sub> Plasma Treatment for SF<sub>6</sub> Decomposition Component Detection**, Xiaoxing Zhang, Xiaoqing Wu, Bing Yang, and Hanyan Xiao  
Volume 2015, Article ID 171545, 9 pages

**Synergetic Effects of Mechanical Properties on Graphene Nanoplatelet and Multiwalled Carbon Nanotube Hybrids Reinforced Epoxy/Carbon Fiber Composites**, Pin-Ning Wang, Tsung-Han Hsieh, Chin-Lung Chiang, and Ming-Yuan Shen  
Volume 2015, Article ID 838032, 9 pages

**Magnetic and Electrical Properties of Nitrogen-Doped Multiwall Carbon Nanotubes Fabricated by a Modified Chemical Vapor Deposition Method**, María Luisa García-Betancourt, Yadira Itzel Vega-Cantu, Sofía Magdalena Vega-Díaz, Aarón Morelos-Gómez, Mauricio Terrones, and Emilio Muñoz-Sandoval  
Volume 2015, Article ID 587416, 14 pages

**Applications of Nanostructured Carbon Materials in Constructions: The State of the Art**, Shu-Nan Lu, Ning Xie, Li-Chao Feng, and Jing Zhong  
Volume 2015, Article ID 807416, 10 pages

**A Review of the Application and Performance of Carbon Nanotubes in Fuel Cells**, Chong Luo, Hui Xie, Qin Wang, Geng Luo, and Chao Liu  
Volume 2015, Article ID 560392, 10 pages

**N-Type Conductive Ultrananocrystalline Diamond Films Grown by Hot Filament CVD**, Michael Mertens, Markus Mohr, Neda Wiora, Kai Brühne, and Hans-Jörg Fecht  
Volume 2015, Article ID 527025, 6 pages

## Editorial

# Nanostructured Carbon Materials

**Myoung-Woon Moon,<sup>1</sup> Ho-Young Kim,<sup>2</sup> Aiying Wang,<sup>3</sup> and Ashkan Vaziri<sup>4</sup>**

<sup>1</sup>*Korea Institute of Science and Technology (KIST), Seoul 136-791, Republic of Korea*

<sup>2</sup>*Seoul National University, Seoul 151-744, Republic of Korea*

<sup>3</sup>*Ningbo Institute of Materials Technology and Engineering (NIMTE), Chinese Academy of Sciences, Ningbo 315201, China*

<sup>4</sup>*Northeastern University, Boston, MA 02155, USA*

Correspondence should be addressed to Myoung-Woon Moon; [mwmoon@kist.re.kr](mailto:mwmoon@kist.re.kr)

Received 30 April 2015; Accepted 30 April 2015

Copyright © 2015 Myoung-Woon Moon et al. This is an open access article distributed under the Creative Commons Attribution License, which permits unrestricted use, distribution, and reproduction in any medium, provided the original work is properly cited.

Nanostructured carbon materials have attracted great attention due to their capability for use in various fields such as energy, environment, water, or biomedicine. Nanostructured carbon materials form various allotropes in zero-, one-, two-, and three-dimensional nanoscale such as fullerene, carbon nanotubes (CNTs), graphene or nanocarbon coating, and diamond or porous carbon, respectively. Furthermore, carbon materials can have new functions in electrical, physical, or chemical properties by assembling or architecturing with different functional nanomaterials, such as nanocomposites of CNTs with functional nanoparticles, carbon nanocoatings with functional metal element or graphene modified with carbon materials, and metal or oxide nanomaterials.

The major goals of this special issue are to find novel fabrication methods for nanostructured carbon materials and the assembling or architecturing of carbon nanomaterials with metal or oxide nanomaterials for novel functionalization in up-to-date applications. The issue includes research papers and article reviews covering a wide range of current progress on nanostructured carbon materials in the wide range of the topics from the fundamentals to the application with nanostructured carbon materials.

In this special issue, some articles are addressing the above-mentioned issues in the form of review. The contribution by S.-N. Lu et al. is providing a review for the state of the art on the applications of nanostructured carbon materials, including carbon nanotubes, carbon nanofibers, and graphene oxides. Its coverage ranges from the preparation process of the nanostructured materials to the applications such as mechanical reinforcement, self-sensing detectors, and

self-heating element. One of the review articles by C. Luo et al. is dealing with the application and performance of carbon nanotubes in fuel cells. The authors provide a review from the noble metals as catalysts to the performance of fuel cell. Treated are the method used to reduce the platinum, the effect of carbon nanotubes on the fuel cell, improving the performance of fuel cell catalysts, the interaction between catalyst and carbon nanotube support, and the synthetic conditions of carbon nanotube supported catalyst.

A research article by M. L. García-Betancourt et al. is presented on the magnetic and electrical properties of nitrogen-doped multiwall carbon nanotubes fabricated by a modified chemical vapor deposition method. By the modification of the CVD configuration, the authors suggested a synthesis way for the morphology control for the nitrogen-doped nanotubes. They suggested that the semiconducting nature of the nitrogen-doped CNT can be shown with water and low NaCl during synthesis processing. Another research article by X. Zhang et al. shows that the multiwalled CNTs (MWCNTs) by CF<sub>4</sub> plasma treatment for SF<sub>6</sub> decomposition component detection are presented on the enhancement of gas-sensing characteristics. MWCNTs, modified by dielectric barrier discharge of CF<sub>4</sub> plasma, show that the gas-sensing effect to H<sub>2</sub>S and SO<sub>2</sub> was effective for the treatment duration since modified MWCNTs contained a low number of impure particles on the surface as well as short length and grafted-F polar functional groups.

Synergetic effects of mechanical properties on graphene nanoplatelet and MWCNT hybrids reinforced epoxy/carbon fiber composites were explored by P.-N. Wang et al., who

provide an outstanding synergetic effect on the graphene nanoplatelets (GNPs) and MWCNTs hybrids. They reported that reinforced epoxy composite and epoxy/carbon fiber composite laminates enhance their mechanical properties over that of neat laminates.

Two research articles present the functional nanocarbon materials of diamond films and biocarbon nanofibers. A research on N-type conductive ultrananocrystalline diamond films grown by hot filament CVD is presented by M. Mertens et al. The research article contributed by X. Huang et al. explores the study of electromagnetic interference (EMI) shielding materials comprised of Ni-Co coated on web-like biocarbon nanofibers via electroless deposition. EMI shielding materials made of Ni-Co were coated on web-like biocarbon nanofibers prepared by electroless plating. Biocarbon nanofibers (CF) were obtained using bacterial cellulose pyrolyzed at 1200°C. The EMI shielding efficiencies of the composites were shown to be significantly higher than that of CF at the same mass fraction.

## **Acknowledgments**

The guest editors would like to thank the authors for their contributions to this special issue and the reviewers for their time and dedication.

*Myoung-Woon Moon  
Ho-Young Kim  
Aiyang Wang  
Ashkan Vaziri*

## Research Article

# Preparation and Study of Electromagnetic Interference Shielding Materials Comprised of Ni-Co Coated on Web-Like Biocarbon Nanofibers via Electroless Deposition

Xiaohu Huang, Bo Dai, Yong Ren, Jing Xu, and Pei Zhu

State Key Laboratory Cultivation Base for Nonmetal Composites and Functional Materials,  
Southwest University of Science and Technology, Mianyang 621010, China

Correspondence should be addressed to Bo Dai; [bodai31@vip.sina.com](mailto:bodai31@vip.sina.com)

Received 22 September 2014; Revised 11 December 2014; Accepted 11 December 2014

Academic Editor: Myoung-Woon Moon

Copyright © 2015 Xiaohu Huang et al. This is an open access article distributed under the Creative Commons Attribution License, which permits unrestricted use, distribution, and reproduction in any medium, provided the original work is properly cited.

Electromagnetic interference (EMI) shielding materials made of Ni-Co coated on web-like biocarbon nanofibers were successfully prepared by electroless plating. Biocarbon nanofibers (CF) with a novel web-like structure comprised of entangled and interconnected carbon nanoribbons were obtained using bacterial cellulose pyrolyzed at 1200°C. Paraffin wax matrix composites filled with different loadings (10, 20, and 30 wt%, resp.) of CF and Ni-Co coated CF (NCCF) were prepared. The electrical conductivities and electromagnetic parameters of the composites were investigated by the four-probe method and vector network analysis. From these results, the EMI shielding efficiencies (SE) of NCCF composites were shown to be significantly higher than that of CF at the same mass fraction. The paraffin wax composites containing 30 wt% NCCF showed the highest EMI SE of 41.2 dB (99.99% attenuation), which are attributed to the higher electrical conductivity and permittivity of the NCCF composites than the CF composites. Additionally, EMI SE increased with an increase in CF and NCCF loading and the absorption was determined to be the primary factor governing EMI shielding. This study conclusively reveals that NCCF composites have potential applications as EMI shielding materials.

## 1. Introduction

In recent years electromagnetic interference (EMI) has become a critical problem for electric devices because it may lead to malfunctions such as in airplane control panels, mobile phones, and many computers. In order to address these problems the development of EMI shielding materials received increasing attention [1–3]. Carbon composites have outstanding potential for use in EMI shielding [4–9] due to their excellent electrical properties, low density, high aspect ratio, and high strength and modulus. However the electrical conductivity of carbon materials is considerably lower than that of metals and therefore a greater amount of carbon material is needed to achieve the same shielding effect. Although satisfactory shielding capabilities can be obtained by simply adding more carbon materials, it is difficult to produce composites with high carbon volume fractions when using extrusion or injection molding. In addition, a high carbon volume fraction increases the composites cost and

thus limits its commercial use. To optimize the conductivity and EMI shielding effectiveness (SE) of composites, it is necessary to attach metal particles to the surface of carbon materials [10–12]. The introduction of metal particles onto carbon materials has previously been shown to lead to good wettability between the fillers and matrices [13], which implies that the dispersion of carbon materials can improve in the matrices. Amongst the common metal materials, nickel and cobalt are suitable for EMI shielding because these metals exhibit good conductivity and magnetic properties, as well as antioxidant properties. Such good conductivity and magnetic materials can produce a large induced current under perturbation by electromagnetic waves, and, according to Lenz's law, these currents will be effective at weakening the penetration of electromagnetic waves [14]. Therefore, it is expected that carbon materials coated with a layer of metal will have the advantages of good conductivity, magnetic, high intensity, and low density and they combine the properties of carbon materials and the magnetic metal together. Although

a variety of techniques are available for altering the chemical and physical properties of the surface of carbon materials, electroless plating has been found to be the most suitable method because of its ability to provide a uniform surface and the cost effectiveness of the process [15–17]. Thus, electroless plating is a convenient approach to produce Ni-Co coated carbon materials. However, the application of traditional metal-coated carbon materials for use as EMI shielding composites is hindered by a major obstacle: the cost and limited supply of carbon materials.

Recently, we developed a novel method of fabricating bio-carbon nanofiber (CF) with a web-like structure consisting of interconnected carbon nanoribbons using low-cost natural materials such as bacterial cellulose as carbonaceous sources. In this work, we report the preparation process of CF, and the electroless plating method was applied to deposit a layer of Ni-Co coating on the surface of CF. The microstructure, magnetic properties, electrical conductivity, electromagnetic parameters, and EMI SE of the composites were investigated.

## 2. Experimental Procedures

**2.1. Preparation of CF.** Web-like structure CF was obtained by heat treatment of bacterial cellulose in a high-temperature tube furnace for 4 h under a nitrogen atmosphere at 1200°C. Afterwards, dried CF was dispersed in absolute ethanol and mechanically milled into a slurry. The resulting CF was dried using a vacuum at 60°C. The bacterial cellulose was kindly provided by Hainan Ye Guo Foods Co., Ltd., Hainan, China.

**2.2. Pretreatments and Electroless Plating of CF with Ni-Co.** For metal-coated CF/polymer matrix composites, the most important factor affecting the SE of composites is the adhesion between the metal coating and CF. Good adhesion can reduce the delamination of metal deposits by shear stress during compounding and can maintain the conductive network. In order to enhance the interfacial adhesion between the CF and the coating, CF was subjected to an oxidation treatment before surface activation. The CF was immersed in an aqueous solution of 200 g/L  $(\text{NH}_4)_2\text{S}_2\text{O}_8$  and 100 mL/L of  $\text{H}_2\text{SO}_4$  (the acid solution readily etches the surface of CF) by sonication at 35°C for 80 min, then was filtered, and thoroughly washed with distilled water until the washings reached  $\text{pH} = 7$ . This procedure promotes the coarsening of the carbon fiber, which can form different functional groups on the CF surface. These surface functional groups can form anchoring sites for metallic nanoparticles, thereby improving the adhesion between the CF and the nanoparticles [18]. The coating procedure consisted of three stages: sensitization, activation, and metallization. The CF and the optimum operating conditions of the sensitized, activated, and plating solutions were listed in Table 1. Firstly, coarsened CF was sensitized for 30 min at 25°C to adsorb  $\text{Sn}^{2+}$  ions. The CF was then filtered and washed with distilled water, and the sensitized CF was placed in an activated solution at 25°C for 30 min to adsorb Pd nuclei on the CF surface. Sonication was applied during the sensitization and activation treatment to promote uniform coating of the surface of CF. Finally, the

TABLE 1: Composition and operating conditions for the different stages in nickel-cobalt electroless coating.

Stage	Solution
Sensitization	23 g/L $\text{SnCl}_2 \cdot 2\text{H}_2\text{O}$ 10 mL/L HCl
Activation	0.25 g/L $\text{PdCl}_2$ 30 mL/L HCl
Metallization	17 g/L $\text{NiSO}_4 \cdot 6\text{H}_2\text{O}$ 9 g/L $\text{CoSO}_4 \cdot 7\text{H}_2\text{O}$ 80 g/L $\text{Na}_3\text{C}_6\text{H}_5\text{O}_7 \cdot 2\text{H}_2\text{O}$ 35 g/L $\text{Na}_2\text{H}_2\text{PO}_4 \cdot \text{H}_2\text{O}$ 49 g/L $(\text{NH}_4)_2\text{SO}_4$

activated CF was washed with distilled water and then added to a bath for metallization, which was carried out at 35°C for 15 min with magnetic stirring. Ammonia solution was used as a buffer to maintain a pH value of 9. Chemicals used in the experiments were all of analytical grade and were purchased from Kelong Reagent Co. Ltd., Chengdu, China. After plating, the Ni-Co coated CF (NCCF) was washed with distilled water and then heat-treated at 450°C in a nitrogen atmosphere for 2 h in a high-temperature tube furnace. After heat treatment, the electrical conductivity of NCCF will improve due to the phase transformation of NCCF [19].

**2.3. Fabrication of Test Samples.** CF and NCCF were dispersed in dimethylbenzene with paraffin wax by sonication at 60°C for 50 min, respectively. Both CF and NCCF dispersed efficiently in the paraffin wax matrix. Test samples with different weight percentages of CF and NCCF (10, 20, and 30 wt%) were fabricated according to the above methods. For electrical conductivity characterization, rectangular plates (10 mm × 10 mm × 1.5 mm) of samples were molded under 7 MPa pressure. For EMI SE characterization, samples were pressed into cylindrical dies with 7.0 mm outer diameter, 3.0 mm inner diameter, and approximately 2.5 mm height at 2 MPa.

**2.4. Characterization.** The morphologies of CF and NCCF were analyzed by transmission electron microscopy (TEM, Libra 200FE, Carl Zeiss SMT Pte Ltd., Germany) coupled with energy dispersive spectroscopy (EDS). Raman spectra were recorded on a Raman spectrometer (Invia, Renishaw, UK), with an excitation laser wavelength of 514.5 nm. An X-ray diffractometer (XRD, X'pert PRO, PANalytical, Netherlands) equipped with a rotating anode and Cu  $K\alpha$  radiation ( $\lambda = 0.15406$  nm) over an incident angle ( $2\theta$ ) range of 10–80° was used to identify the crystalline phases of the coating. The static magnetic properties were determined using a vibration sample magnetometer (BKT-4500Z, Beijing Ze Tian Wei Ye Science and Technology Co., Ltd., China). The sheet resistance ( $R_s$ ) of the samples was measured by the four-probe method using a Keithley 2400 multimeter (Cleveland, OH, USA). The electromagnetic and scattering parameters of the samples were measured using a vector network analyzer (E5071C, Agilent Science and Technology Co., Ltd., USA) in the 8.2–12.4 GHz (X-band) frequency range.

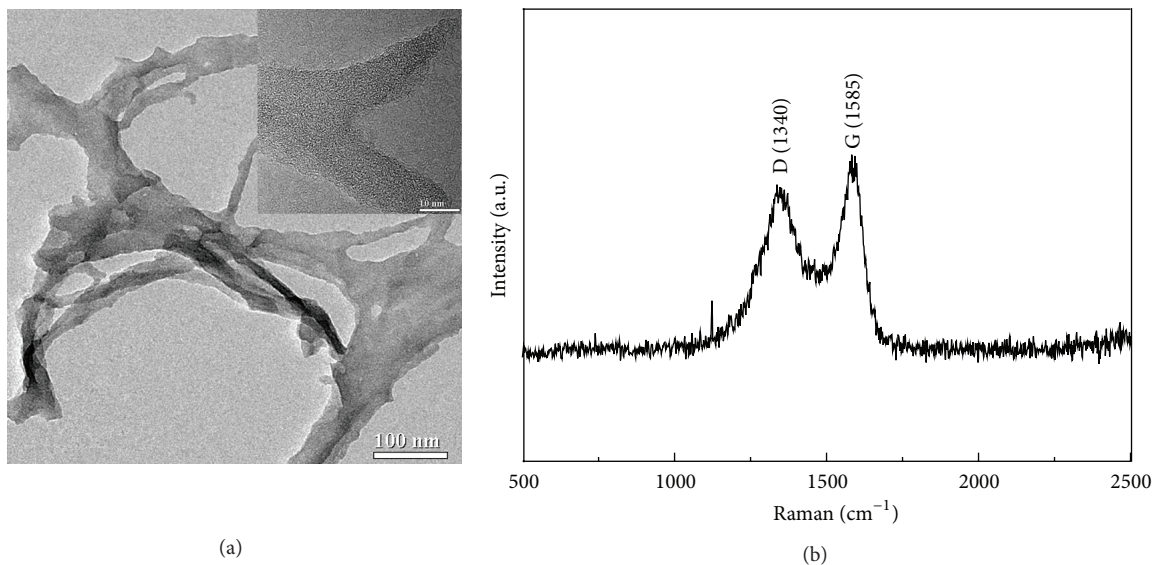


FIGURE 1: (a) TEM micrographs of CF and (b) Raman spectra of CF.

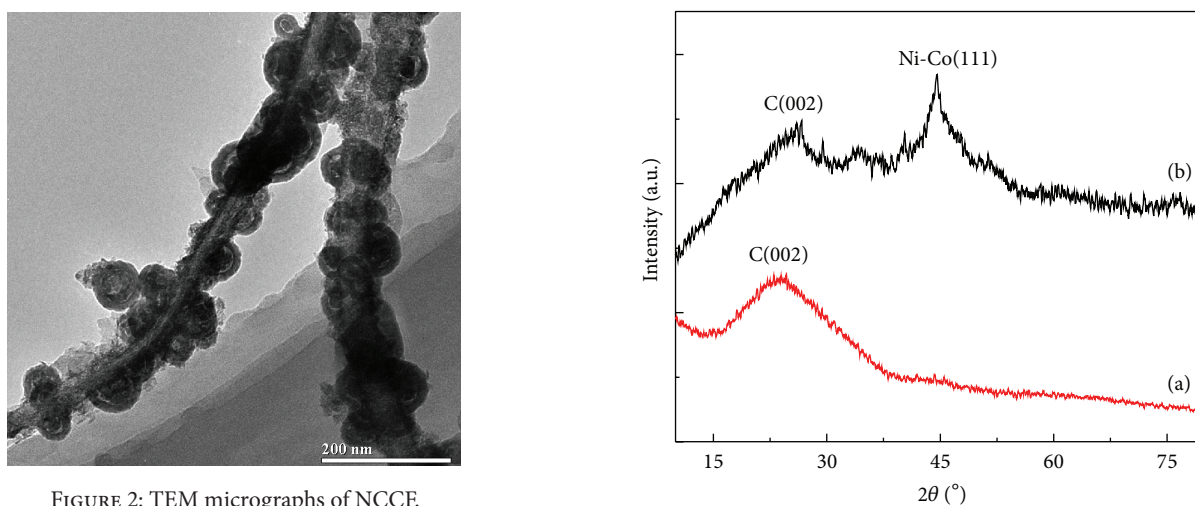


FIGURE 2: TEM micrographs of NCCF.

FIGURE 3: XRD patterns of (a) pristine CF and (b) NCCF.

### 3. Results and Discussions

The morphology of nanofibers is an important factor affecting the SE of fiber composites [20]. Figure 1(a) shows the TEM image of the obtained CF, which reveals that the CF are web-like and the diameters can be up to 20 nm. A higher magnification shows that a small amount of graphitic multilayer structure was seen as shown in the inset figure, showing that the CF is slightly graphitized. Figure 1(b) shows the Raman spectra of the obtained CF. In the Raman spectra, two fundamental vibrations are observed at  $1340\text{ cm}^{-1}$  and  $1585\text{ cm}^{-1}$  for CF, which are attributed to the D and G bands, respectively. The D peak can be assigned to the disorder-activated Raman mode, while the G peak arises from the  $\text{sp}^2$  hybridized carbon [21]. Figure 2 is a representative TEM image of NCCF, which clearly indicates that nickel-cobalt spherical grains were formed on the CF surface. The coating layer tended to form as spherical grains, perhaps because

the surface exhibits high curvature and on a curved surface the normal growth rate is higher than the lateral growth rate. Obviously the diameter of NCCF is wider than the obtained CF after electroless plating. These results indicate that the wider NCCF in the diameter is highly beneficial to the improvement electrical conductivity of the CF. The EDS spectrum showed that the major components in NCCF are carbon, nickel, cobalt, and oxygen.

The phase structures of both CF and NCCF have been determined by XRD. Figure 3 shows the XRD patterns of (a) the pristine CF and (b) NCCF. It suggests that the CF and NCCF display amorphous structures. In the diffraction pattern (Figure 3(a)) of pristine CF, a broad and weak peak at  $2\theta = 24.35^\circ$  is observed, which is assigned to the (002) plane of graphitic carbon, which is in good agreement with Figure 1(b). In the case of NCCF, a new broad peak other than the (002) diffraction peak of graphitized CF is clearly

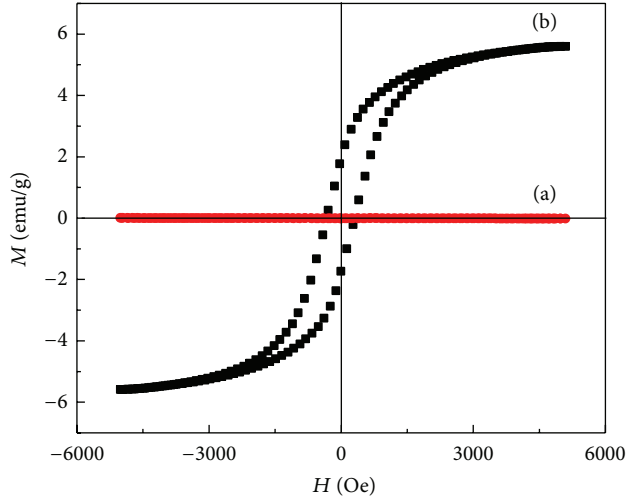


FIGURE 4: Magnetic hysteresis loop of (a) CF and (b) NCCF at 300 K.

observed at around  $44.57^\circ$  as shown in Figure 3(b), which originates from the deposited Ni-Co coating layer. The results of the XRD analyses indicate that the Ni-Co nanoparticles were successfully deposited on the surface of the CF.

Figure 4 shows the magnetic hysteresis loops of CF and NCCF. The CF exhibited very little magnetization or coercivity, while the NCCF exhibited obvious magnetization. The saturation magnetization and coercivity of NCCF were 312 Oe and 5.58 emu/g, respectively. The magnetic properties of NCCF are significantly higher than those of CF, which indicates that the CF has been covered successfully by a layer of ferromagnetic Ni-Co nanoparticles.

Conductivity is another factor affecting the shielding properties of a material [22]. Electrical conductivity is calculated according to the following equation:

$$\sigma = \frac{1}{R_s t}, \quad (1)$$

where  $\sigma$ ,  $R_s$ , and  $t$  represent the direct current conductivity, sheet resistance, and sheet thickness, respectively. The relationship between electrical conductivity and nanofibers (CF and NCCF) loading is illustrated in Figure 5, which shows that the electrical conductivity of NCCF is bigger than that of pure CF at the same mass fraction. The composites containing 30 wt% NCCF exhibit the highest electrical conductivity of 1313 S/m, suggesting that the addition of electrical Ni-Co nanoparticles onto CF is highly beneficial to the electrical conductivity of the composites. The electrical conductivity increases with nanofibers loading because the interfacial affinity between nanofibers and the paraffin wax matrix increases the number of conductive pathways for electron transfer. The excellent electrical conductivity of the composites can improve the electromagnetic energy absorption and dissipation capabilities, resulting in enhancement of microwave shielding effectiveness [23].

To evaluate the EMI performance of CF and the NCCF composites, we thus measured the permittivity ( $\epsilon = \epsilon' - j\epsilon''$  constitutes the real part ( $\epsilon'$ ) and imaginary part ( $\epsilon''$ ), resp.) of our composites in the frequency range of 8.2–12.4 GHz.

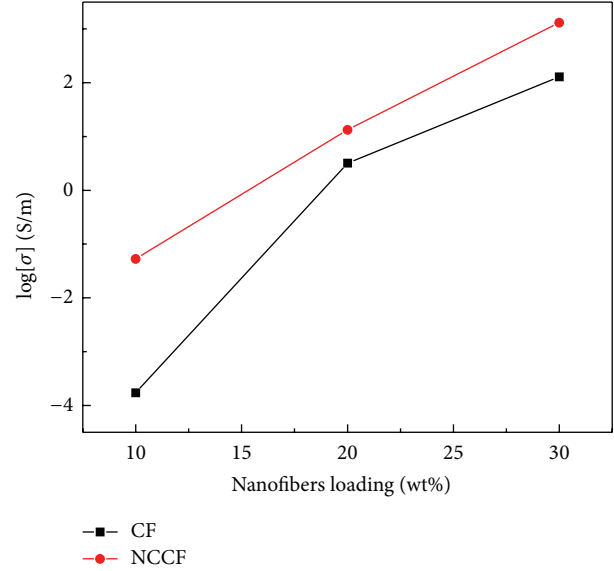


FIGURE 5: Electrical conductivity of CF and NCCF. The thickness of all the samples was 1.5 mm.

Figure 6 shows the room temperature permittivity of the pure CF and the NCCF composites. The results indicate that the real part and imaginary part of the permittivity of NCCF are bigger than those of pure CF at the same mass fraction. According to the theory of permittivity, when electromagnetic radiation is incident on metallic surface the electric field induces two types of electrical currents within the material (displacement currents and conduction). The former arises from bound charges, that is, polarization effects (real part of permittivity) which mainly involves unpaired point defects, and the latter arises due to free electrons giving rise to electric loss (imaginary part of permittivity) [24]. In other words, the real part of the composites permittivity is a measure of the number of the polarization centers inside the material originating from defects in the nanofibers structure. Therefore, the NCCF nanofibers increase the number of structural defects. The increase of the imaginary part of the permittivity can be attributed to the enhanced electrical conductivity of the composites. Both the real and imaginary parts of permittivity increase as the loading of the CF or NCCF was increased, which reflects an increase in both the number of polarization centers and dissipating mobile charge carriers, leading to higher permittivity. While this explanation implies that more structural defects and high conductivity result in high permittivity, nevertheless, it is noted that the permittivity decreases with increasing frequency. This behavior is due to the lag of the induced electric field in the composites in response to the reversing external E-field, which leads to a reduction in electronic oscillation at high frequency [25].

The EMI SE of a material is represented by the following equation:

$$SE_T = 10 \log \left( \frac{P_{in}}{P_{out}} \right) = SE_R + SE_A + SE_M, \quad (2)$$

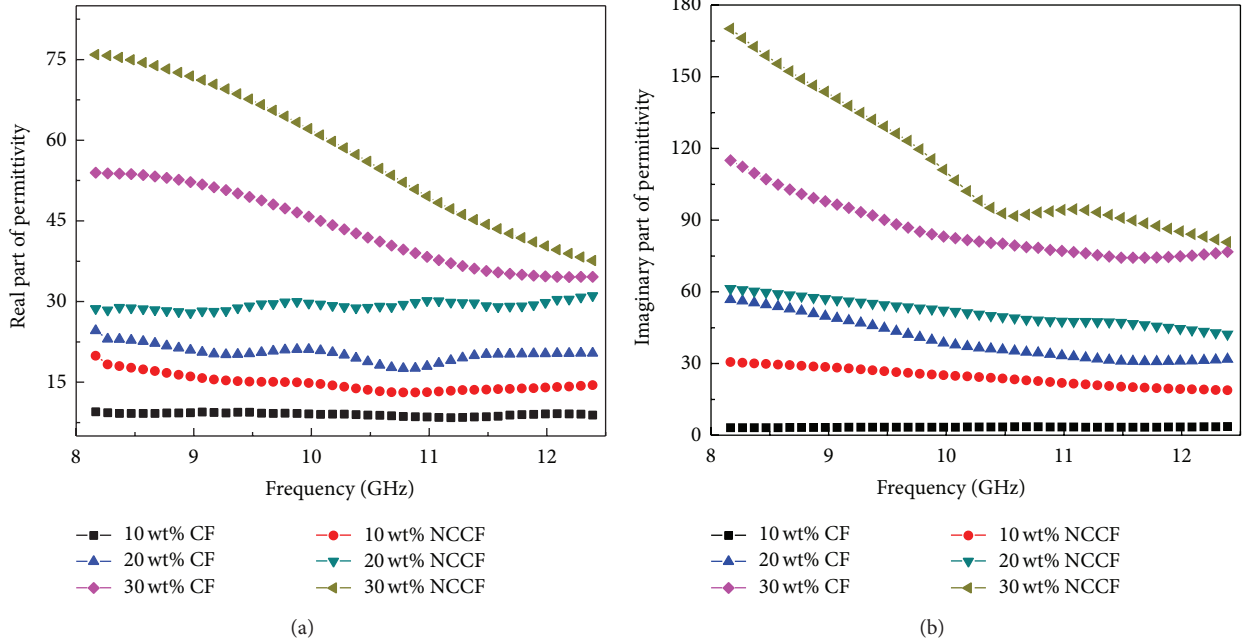


FIGURE 6: (a) The real and (b) the imaginary parts of the permittivity of the composites as a function of frequency.

where  $P_{in}$  and  $P_{out}$  are the power (electric or magnetic field) of incident and transmitted EM waves, respectively, and  $SE_R$ ,  $SE_A$ , and  $SE_M$  are the SE due to reflection, absorption, and multiple reflections, respectively [26]. Reflection occurs as a result of mobile charge carriers (electrons or holes) in the shield material which interact with the electromagnetic field in the radiation; the absorption is due to the energy dissipation when electromagnetic wave interacts with electric or magnetic dipoles in the shield material; the multiple reflections refer to the reflection at different surfaces or interfaces in the shield material [27].

$S_{11}$  (or  $S_{11}$ ) and  $S_{12}$  (or  $S_{21}$ ) are the scattering parameters (S-parameters) of the two-port vector network analyzer system and can be related to reflectance and transmittance as  $R = |S_{11}|^2 = |S_{22}|^2$  and  $T = |S_{21}|^2 = |S_{12}|^2$ . The absorbance ( $A$ ) can be written as  $A = (1 - R - T)$ . When  $SE_A$  is higher than 10 dB,  $SE_M$  can be ignored [28]. Therefore,  $SE_T$  can be conveniently expressed as  $SE_T = SE_R + SE_A$ . The EMI SE was calculated based on the S-parameters as follows:

$$SE_T = 10 \log \frac{1}{|S_{12}|^2} = 10 \log \frac{1}{|S_{21}|^2},$$

$$SE_R = 10 \log \left( \frac{1}{1 - |S_{11}|^2} \right), \quad (3)$$

$$SE_A = 10 \log \left( \frac{1 - |S_{11}|^2}{|S_{12}|^2} \right),$$

where  $|S_{ij}|^2$  represents the power transmitted from port  $i$  to port  $j$  [29].

The influence of mass fraction on the  $SE_T$  values of the composites at 10 GHz is shown in Figure 7. The experimental

trend is similar to the trend of the electric conductivity of the CF and NCCF composites. In line with the above data concerning conductivity and permittivity, the  $SE_T$  values of the CF and NCCF composites increased with the weight percentage. This may be ascribed to the increase of electrical conductivity of the composites. As was observed for the conductivity of composites, the  $SE_T$  of the NCCF composite is significantly higher than that of CF at the same mass fraction. The Ni-Co coating on the CF can lead to a decrease in the contact loss between CF due to the formation of metal-metal interfaces. This behavior can improve the electrical conductivity and subsequently the  $SE_T$  of the NCCF composites.

To clarify the EMI shielding mechanism of the CF and NCCF composites, the EMI  $SE_R$ ,  $SE_A$ , and total  $SE_T$  of the composites with 30 wt% conductive nanofibers in the 8.2–12.4 GHz range are shown in Figure 8. From the figure,  $SE_A$  was shown to be *ca.* 34.3 and 37.3 dB for CF and NCCF composites at 12.4 GHz, respectively. For the reflection component,  $SE_R$  was *ca.* 2.6 and 3.9 dB for CF and NCCF composites at 12.4 GHz, respectively. These results demonstrate that the  $SE_T$  of the NCCF composites can be up to 41.2 dB (99.99% attenuation), which is higher than that of the pristine CF composites [30]. It has been observed that, for conduct CF and NCCF composites, the  $SE_T$  is mainly dominated by absorption while the  $SE_R$  contributes little.

## 4. Conclusions

In conclusion, NCCF was successfully manufactured by electroless plating. This work demonstrates that both the electrical conductivity and the EMI SE increase with nanofibers loading and the paraffin wax composite containing 30 wt% NCCF exhibited the highest electrical conductivity of

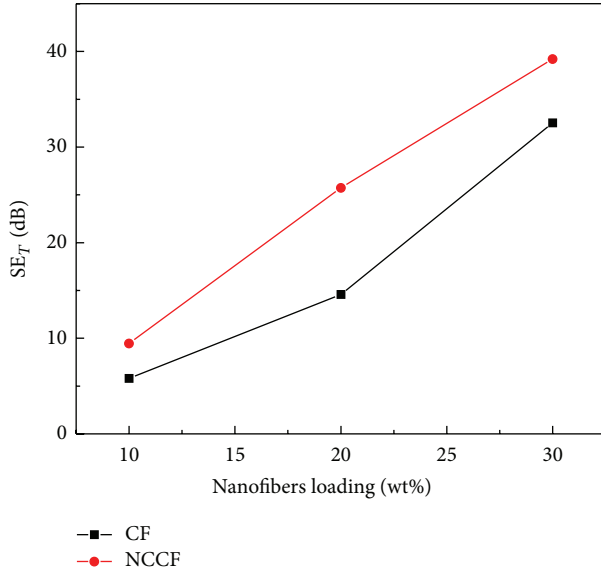


FIGURE 7: EMI shielding effectiveness of CF and NCCF composites at 10 GHz. The thickness of all the samples was 2.5 mm.

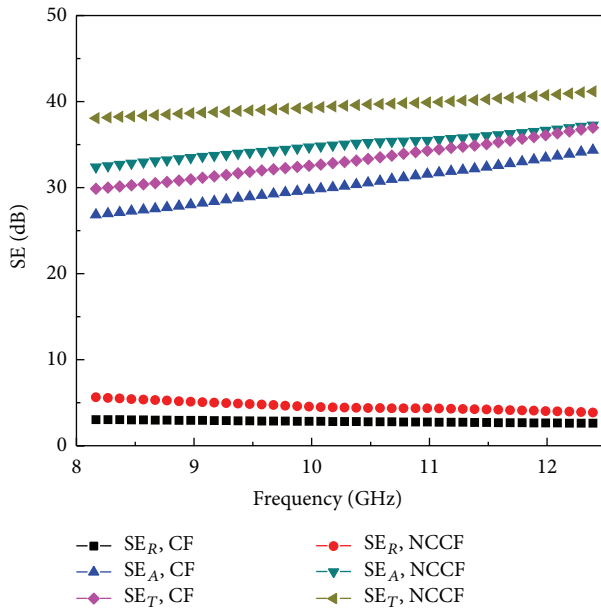


FIGURE 8: EMI shielding effectiveness of CF and NCCF composites with 30 wt% conductive nanofibers as a function of frequency. The thickness of all the samples was 2.5 mm.

1313 S/m and EMI SE value of 41.2 dB (99.99% attenuation). This result may be attributed to the presence of Ni-Co coated on the CF, which can lead to decrease in the contact loss between CF due to the formation of metal-metal interfaces. This behavior can improve the electrical conductivity and permittivity and subsequently improve the EMI SE. The SE of composites increases with nanofibers loading and the absorption is the primary factor governing EMI shielding. This study reveals that the NCCF composites have potential applications as EMI shielding materials.

## Conflict of Interests

The authors declare that there is no conflict of interests regarding the publication of this paper.

## Acknowledgment

This work was supported by the Program for New Century Excellent Talents in university (no. MCET-11-1061).

## References

- [1] N. Joseph and M. T. Sebastian, "Electromagnetic interference shielding nature of PVDF-carbonyl iron composites," *Materials Letters*, vol. 90, pp. 64–67, 2013.
- [2] S. X. Jiang and R. H. Guo, "Electromagnetic shielding and corrosion resistance of electroless Ni-P/Cu-Ni multilayer plated polyester fabric," *Surface and Coatings Technology*, vol. 205, no. 17-18, pp. 4274–4279, 2011.
- [3] M. H. Al-Saleh, G. A. Gelves, and U. Sundararaj, "Copper nanowire/polystyrene nanocomposites: lower percolation threshold and higher EMI shielding," *Composites Part A: Applied Science and Manufacturing*, vol. 42, no. 1, pp. 92–97, 2011.
- [4] G.-H. Kang and S.-H. Kim, "Electromagnetic wave shielding effectiveness based on carbon microcoil-polyurethane composites," *Journal of Nanomaterials*, vol. 2014, Article ID 727024, 6 pages, 2014.
- [5] W.-L. Song, M.-S. Cao, M.-M. Lu et al., "Flexible graphene/polymer composite films in sandwich structures for effective electromagnetic interference shielding," *Carbon*, vol. 66, pp. 67–76, 2014.
- [6] A. Gupta and V. Choudhary, "Electrical conductivity and shielding effectiveness of poly(trimethylene terephthalate)/multiwalled carbon nanotube composites," *Journal of Materials Science*, vol. 46, no. 19, pp. 6416–6423, 2011.
- [7] D.-X. Yan, H. Pang, L. Xu et al., "Electromagnetic interference shielding of segregated polymer composite with an ultralow loading of in situ thermally reduced graphene oxide," *Nanotechnology*, vol. 25, no. 14, Article ID 145705, 2014.
- [8] A. P. Singh, B. K. Gupta, M. Mishra, A. Chandra, R. B. Mathur, and S. K. Dhawan, "Multiwalled carbon nanotube/cement composites with exceptional electromagnetic interference shielding properties," *Carbon*, vol. 56, pp. 86–96, 2013.
- [9] D. D. L. Chung, "Carbon materials for structural self-sensing, electromagnetic shielding and thermal interfacing," *Carbon*, vol. 50, no. 9, pp. 3342–3353, 2012.
- [10] B.-J. Kim, K.-M. Bae, Y. S. Lee, K.-H. An, and S.-J. Park, "EMI shielding behaviors of Ni-coated MWCNTs-filled epoxy matrix nanocomposites," *Surface and Coatings Technology*, vol. 242, pp. 125–131, 2014.
- [11] R. R. Bonaldi, E. Siores, and T. Shah, "Characterization of electromagnetic shielding fabrics obtained from carbon nanotube composite coatings," *Synthetic Metals*, vol. 187, no. 1, pp. 1–8, 2014.
- [12] B.-J. Kim, W.-K. Choi, M.-K. Um, and S.-J. Park, "Effects of nickel coating thickness on electric properties of nickel/carbon hybrid fibers," *Surface and Coatings Technology*, vol. 205, no. 11, pp. 3416–3421, 2011.
- [13] B.-J. Kim, K.-M. Bae, M.-K. Seo, K.-H. An, and S.-J. Park, "Roles of Ni/CNTs hybridization on rheological and mechanical

- properties of CNTs/epoxy nanocomposites,” *Materials Science and Engineering: A*, vol. 528, no. 15, pp. 4953–4957, 2011.
- [14] K. Ji, H. Zhao, J. Zhang, J. Chen, and Z. Dai, “Fabrication and electromagnetic interference shielding performance of open-cell foam of a Cu-Ni alloy integrated with CNTs,” *Applied Surface Science*, vol. 311, pp. 351–356, 2014.
- [15] H. Bi, K.-C. Kou, K. K. Ostrikov, L.-K. Yan, and Z.-C. Wang, “Microstructure and electromagnetic characteristics of Ni nanoparticle film coated carbon microcoils,” *Journal of Alloys and Compounds*, vol. 478, no. 1-2, pp. 796–800, 2009.
- [16] F. Wang, S. Arai, and M. Endo, “Metallization of multi-walled carbon nanotubes with copper by an electroless deposition process,” *Electrochemistry Communications*, vol. 6, no. 10, pp. 1042–1044, 2004.
- [17] T. Homma, Y. Sezai, and T. Osaka, “A study on growth processes of CoNiP perpendicular magnetic anisotropy films electroless-deposited at room temperature,” *Electrochimica Acta*, vol. 42, no. 20-22, pp. 3041–3047, 1997.
- [18] Y. Li, C. Zhu, and C. Wang, “Controllable synthesis, characterization and microwave absorption properties of magnetic  $Ni_{1-x}Co_xP$  alloy nanoparticles attached on carbon nanotubes,” *Journal of Physics D: Applied Physics*, vol. 41, no. 12, Article ID 125303, 2008.
- [19] C.-Y. Huang, W.-W. Mo, and M.-L. Roan, “The influence of heat treatment on electroless-nickel coated fibre (ENCF) on the mechanical properties and EMI shielding of ENCF reinforced ABS polymeric composites,” *Surface and Coatings Technology*, vol. 184, no. 2-3, pp. 123–132, 2004.
- [20] W.-S. Jou, H.-Z. Cheng, and C.-F. Hsu, “The electromagnetic shielding effectiveness of carbon nanotubes polymer composites,” *Journal of Alloys and Compounds*, vol. 434-435, pp. 641–645, 2007.
- [21] D. C. Elias, R. R. Nair, T. M. G. Mohiuddin et al., “Control of graphene’s properties by reversible hydrogenation: evidence for graphane,” *Science*, vol. 323, no. 5914, pp. 610–613, 2009.
- [22] N. Li, Y. Huang, F. Du et al., “Electromagnetic Interference (EMI) shielding of single-walled carbon nanotube epoxy composites,” *Nano Letters*, vol. 6, no. 6, pp. 1141–1145, 2006.
- [23] B. P. Singh, V. Choudhary, P. Saini, and R. B. Mathur, “Designing of epoxy composites reinforced with carbon nanotubes grown carbon fiber fabric for improved electromagnetic interference shielding,” *AIP Advances*, vol. 2, no. 2, Article ID 022151, 2012.
- [24] S.-L. Shi and J. Liang, “The effect of multi-wall carbon nanotubes on electromagnetic interference shielding of ceramic composites,” *Nanotechnology*, vol. 19, no. 25, Article ID 255707, 2008.
- [25] C. Wang, X. J. Han, P. Xu, L. Zhang, Y. C. Du, and S. R. Hu, “The electromagnetic property of chemically reduced graphene oxide and its application as microwave absorbing material,” *Applied Physics Letters*, vol. 98, no. 7, Article ID 072906, 2011.
- [26] A. P. Singh, M. Mishra, A. Chandra, and S. K. Dhawan, “Graphene oxide/ferrofluid/cement composites for electromagnetic interference shielding application,” *Nanotechnology*, vol. 22, no. 46, Article ID 465701, 2011.
- [27] T. K. Gupta, B. P. Singh, R. B. Mathur, and S. R. Dhakate, “Multi-walled carbon nanotube-graphene-polyaniline multi-phase nanocomposite with superior electromagnetic shielding effectiveness,” *Nanoscale*, vol. 6, no. 2, pp. 842–851, 2014.
- [28] Y. Chen, Y. Li, M. Yip, and N. Tai, “Electromagnetic interference shielding efficiency of polyaniline composites filled with graphene decorated with metallic nanoparticles,” *Composites Science and Technology*, vol. 80, pp. 80–86, 2013.
- [29] M. H. Al-Saleh, W. H. Saadeh, and U. Sundararaj, “EMI shielding effectiveness of carbon based nanostructured polymeric materials: a comparative study,” *Carbon*, vol. 60, pp. 146–156, 2013.
- [30] B. Dai, Y. Ren, G. Wang, Y. Ma, P. Zhu, and S. Li, “Microstructure and dielectric properties of biocarbon nanofiber composites,” *Nanoscale Research Letters*, vol. 8, no. 1, pp. 1–6, 2013.

## Research Article

# Enhancement of Gas Sensing Characteristics of Multiwalled Carbon Nanotubes by CF<sub>4</sub> Plasma Treatment for SF<sub>6</sub> Decomposition Component Detection

Xiaoxing Zhang,<sup>1,2</sup> Xiaoqing Wu,<sup>1</sup> Bing Yang,<sup>3</sup> and Hanyan Xiao<sup>1</sup>

<sup>1</sup>State Key Laboratory of Power Transmission Equipment & System Security and New Technology, Chongqing University, Chongqing 400044, China

<sup>2</sup>School of Electrical Engineering, Wuhan University, Wuhan 430072, China

<sup>3</sup>Central Southern China Electric Power Design Institute, Wuhan 430071, China

Correspondence should be addressed to Xiaoxing Zhang; [xiaoxing.zhang@outlook.com](mailto:xiaoxing.zhang@outlook.com)

Received 2 July 2014; Accepted 30 November 2014

Academic Editor: Myoung-Woon Moon

Copyright © 2015 Xiaoxing Zhang et al. This is an open access article distributed under the Creative Commons Attribution License, which permits unrestricted use, distribution, and reproduction in any medium, provided the original work is properly cited.

H<sub>2</sub>S and SO<sub>2</sub> are important gas components of decomposed SF<sub>6</sub> of partial discharge generated by insulation defects in gas-insulated switchgear (GIS). Therefore, H<sub>2</sub>S and SO<sub>2</sub> detection is important in the state evaluation and fault diagnosis of GIS. In this study, dielectric barrier discharge was used to generate CF<sub>4</sub> plasma and modify multiwalled carbon nanotubes (MWNTs). The nanotubes were plasma-treated at optimum discharge conditions under different treatment times (0.5, 1, 2, 5, 8, 10, and 12 min). Pristine and treated MWNTs were used as gas sensors to detect H<sub>2</sub>S and SO<sub>2</sub>. The effects of treatment time on gas sensitivity were analyzed. Results showed that the sensitivity, response, and recovery time of modified MWNTs to H<sub>2</sub>S were improved, but the recovery time of SO<sub>2</sub> was almost unchanged. At 10 min treatment time, the MWNTs showed good stability and reproducibility with better gas sensing properties compared with the other nanotubes.

## 1. Introduction

Sulfur hexafluoride (SF<sub>6</sub>) is used as a gas medium in gas-insulated switchgear (GIS), which is widely used in substations and urban power grids because of its compact structure, high reliability, and low electromagnetic radiation [1, 2]. In the manufacture, transportation and installation processes inevitably lead to defects (e.g., metal burrs, protrusions, and suspended particles) in GIS equipment. Under long-term operation, these latent defects result in varying degrees of partial discharge (PD) that lead to SF<sub>6</sub> decomposition. Complex chemical reactions with trace amounts of air and water vapor in GIS generate SOF<sub>2</sub>, SO<sub>2</sub>F<sub>2</sub>, SO<sub>2</sub>, H<sub>2</sub>S, and HF [3–6]. These by-products accelerate insulation aging and corrode metal surfaces, thereby yielding GIS faults [7]. H<sub>2</sub>S and SO<sub>2</sub> are important gases of PD produced by latent insulation defects in GIS [8, 9]. Thus, H<sub>2</sub>S and SO<sub>2</sub> detection is significant in the state evaluation and fault diagnosis of GIS equipment.

Products of SF<sub>6</sub> discharge decomposition are often detected using test tube method [10], gas chromatography [11], and infrared absorption spectrometry [12], but these techniques have several disadvantages. Carbon nanotubes (CNTs) are ideal materials for nanosized gas sensors because of their high surface adsorption capacity, good conductivity, and electronic transmission characteristics [13–17]. Analyses on CNT gas sensors have focused on the repeatability and the improvement of sensitivity. However, untreated CNTs are only sensitive to several gases (e.g., NH<sub>3</sub>, NO<sub>2</sub>, and H<sub>2</sub>). Therefore, surface modification of CNTs should be explored to improve their sensitivity to other gases.

Gas discharge has been used to generate low-temperature plasma in material surface modification because of its low cost, efficiency, rapidity, and nonsignificant contribution to pollution. Dielectric barrier discharge (DBD) is employed to produce low-temperature plasma. The premodified materials are usually placed in the effective discharge area. O<sub>2</sub>, N<sub>2</sub>,

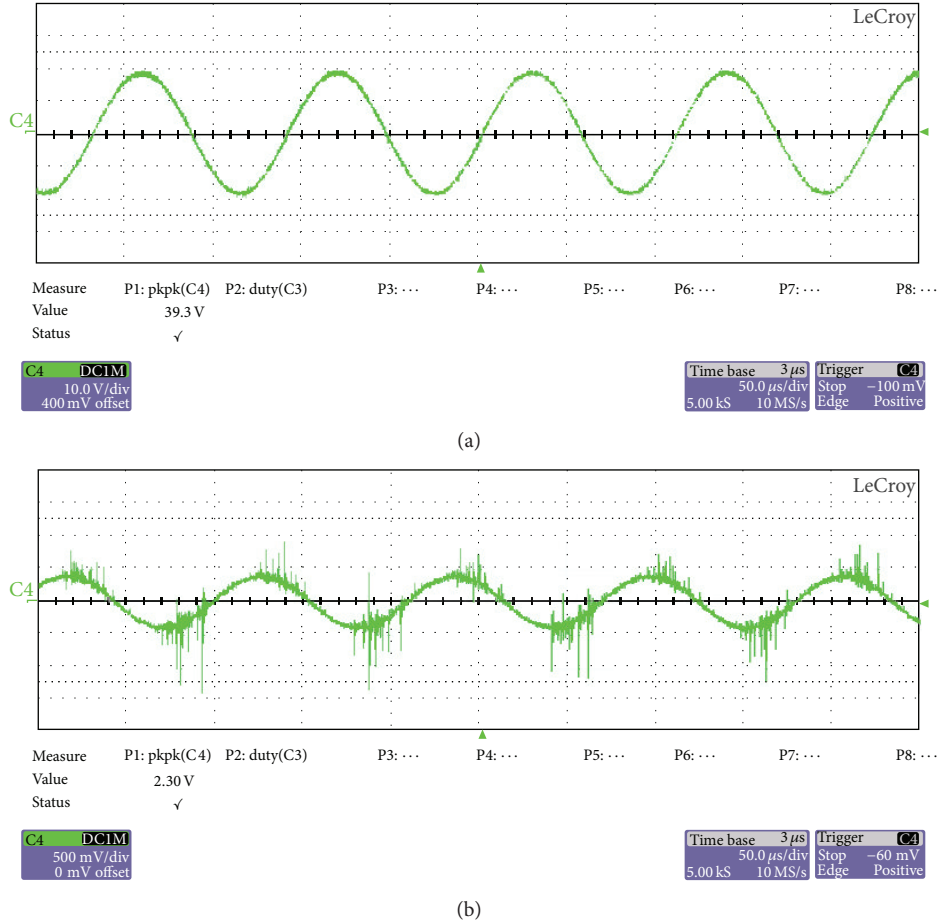


FIGURE 1: Discharge waveforms: (a) output voltage waveform and (b) output current waveform.

$\text{CF}_4$ , and Ar, plasma, and so forth are used to etch the material surface, induce roughness, and connect the active groups. In 2010, Leghrib et al. reported that metal-doped  $\text{O}_2$ -plasma-treated multiwalled carbon nanotubes (MWNTs) exhibited high sensitivity to benzene vapor [18]. Dong et al. (2012) found that Ar- and  $\text{O}_2$ -plasma-modified CNTs have good responses to  $\text{NO}_2$ , whereas  $\text{CF}_4$ - and  $\text{SF}_6$ -treated CNTs are highly sensitive to  $\text{NH}_3$  to achieve good selectivity [19]. In 2012, Zhang et al. used air-plasma-modified MWNTs that were generated by DBD under atmospheric pressure to detect  $\text{H}_2\text{S}$  and  $\text{SO}_2$  [20]. They found that MWNTs-based gas sensors obtained higher responses to  $\text{H}_2\text{S}$  than those based on pristine nanotubes, but these sensors were not sensitive to  $\text{SO}_2$ .

$\text{CF}_4$  is a commonly used plasma etching gas. It is a kind of fluoride gas. In this study, the surface of the MWNTs is modified by  $\text{CF}_4$  plasma generated by DBD. Then gas sensors based on MWNTs were fabricated to detect the products of  $\text{SF}_6$  decomposition in GIS. Results showed that after plasma modification the sensitivity and response time of MWNTs gas sensors towards  $\text{H}_2\text{S}$  and  $\text{SO}_2$  are greatly improved. MWNTs gas sensors with 10 min treatment time showed good stability and reproducibility with better gas sensing properties compared with other sensors.

## 2. Experiment

**2.1. Surface Modification.** MWNTs (tube diameter, 20 nm to 30 nm; length, 10  $\mu\text{m}$  to 30  $\mu\text{m}$ ; purity, >95%) were grown by chemical vapor deposition (CVD) in black powder and purchased from the Chengdu Institute of Organic Chemistry Chengdu, China. CNTs are one-dimensional (1D) nanomaterials. Hence, appropriate surface processing parameters should be selected. Under strong plasma treatments, high power and long treatment time can destroy the tubular structure and carbonization of CNTs [21, 22]. In this study, a DBD plasma generator was used to modify MWNTs. Figure 1 shows the schematic for the test device. Low-temperature plasma experimental power (CTP-2000K) used in this experiment was produced from Nanjing Rongman Electronics Co., Ltd., China. The input voltage of the experimental power is controlled by a voltage regulator. Adjust the voltage to 30 V, which can be reading from the voltmeter (power input) in the power device. Adjust output frequency knob in the experimental power until frequency is around 10 kHz. Then we can get an optimum DBD discharge. Read the input current of 1.96 A from Ammeter in the power device. Use oscilloscope to obtain the output voltage and current waves, displayed in Figure 1. We should point out that there is

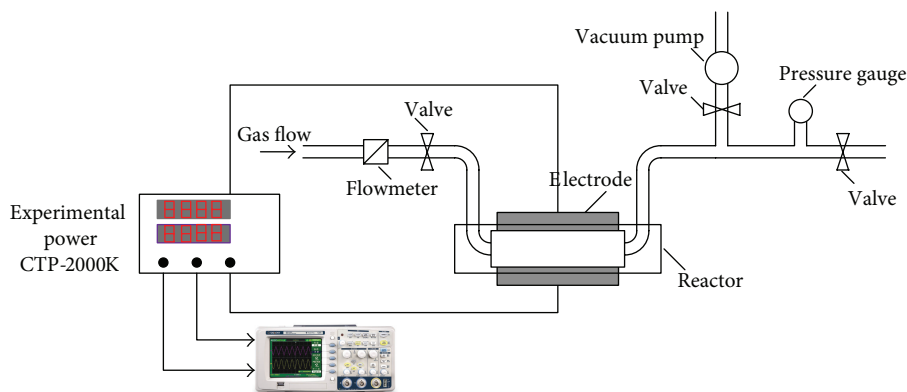


FIGURE 2: Schematic of the DBD experiment setup.

an attenuator in this experimental power and the attenuation coefficient is 1000. So the output peak-to-peak voltage is 39.3 kV. The discharge power in DBD plasma reactor can be calculated by Lissajou curve. However, due to the poor laboratory conditions we do not have enough oscilloscope attenuation probes to protect oscilloscope from breakdown. So other methods should be explored and we try to get in touch with the equipment manufacturers. According to the experience of the manufacturer's data, the plasma treatment power is approximately 0.8 times the input power at the same experimental conditions. Therefore, we can calculate the discharge power, which is 47 W.

Figure 2 reveals that the shape of the reactor is similar to a Petri dish. The reactor electrodes formed a parallel-plate structure and were made of 2 mm thick quartz glass. The upper and bottom electrodes were 8 mm apart. The bottom quartz glass electrode adhered to the reaction kettle, whereas the upper electrode is removable. In the modified experiment, an adequate amount of MWNTs was placed in a reaction kettle and sealed with silicone to ensure gas tightness. Air was released from the reactor to induce a vacuum state.  $\text{CF}_4$  flow rate was controlled at 150 sccm. The parameters of the experimental power were adjusted, and MWNTs were, respectively, treated for 0.5, 1, 2, 5, 8, 10, and 12 min. The upper quartz glass was removed, and modified MWNTs were obtained after the treatment.

**2.2. Preparation of MWNT Sensors.** MWNT sensors were made of printed circuit board, and the substrate material is epoxy resin. Cu interdigital electrodes were etched in the substrate. The width and spacing of the electrodes are both 0.2 mm. First, MWNTs were placed into a beaker containing the appropriate ethanol solution. The beaker was placed in an ultrasonic bath for 1 h. Then, the sensor substrate was repeatedly cleaned with deionized water to remove impurities on the electrode surface. Next, the mixed solution was dropped on the substrate surface. Finally, the MWNT-coated substrates were baked in an oven at  $80^\circ\text{C}$  for a specific time. This process was repeated several times until uniform MWNTs films were deposited on the surface. Seven pristine and treated MWNTs with different modification times were used to fabricate the gas sensors.

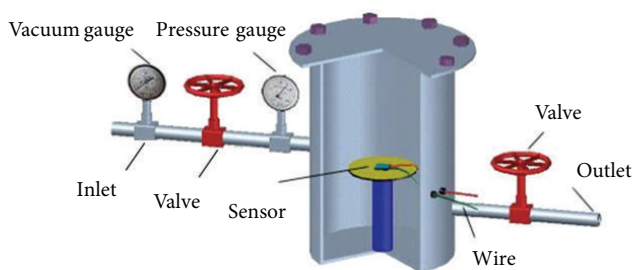


FIGURE 3: Structure of the gas sensor detecting device.

**2.3. Sensitivity Measurement.** Experiments on gas sensitivity were performed to test the resistance rate of the sensor upon exposure in the corresponding gas atmosphere. The gas sensing detection device mainly comprised a steel chamber, which was designed by our group and could be sealed by screws (Figure 3). The MWNTs sensors were placed in the gas chamber and connected to CHI660 electrochemical analyzer through the wires. The impedance-time function of the analyzer was used to record the changes in sensor resistance. Experiments were performed at room temperature.

Sensor sensitivity  $S$  is defined as

$$S = \frac{(R - R_0)}{R_0} \times 100\%, \quad (1)$$

where  $R$  represents the resistance upon exposure to the test gases and  $R_0$  is the initial resistance of the sensor in vacuum.

For resistance-type sensors, the response time comes from the sensor in contact with target gas until 90% of the stable resistance is attained. The recovery time represents the speeds of gas desorption and is defined as the time by which the resistance returns to 90% of the initial value after escaping from the corresponding gas.

### 3. Results and Analysis

**3.1. Fourier-Transform Infrared (FTIR) Spectrum.** FTIR spectra are highly useful tools to analyze the characteristics of CNTs. Figure 4 shows the FTIR spectra of pristine MWNTs

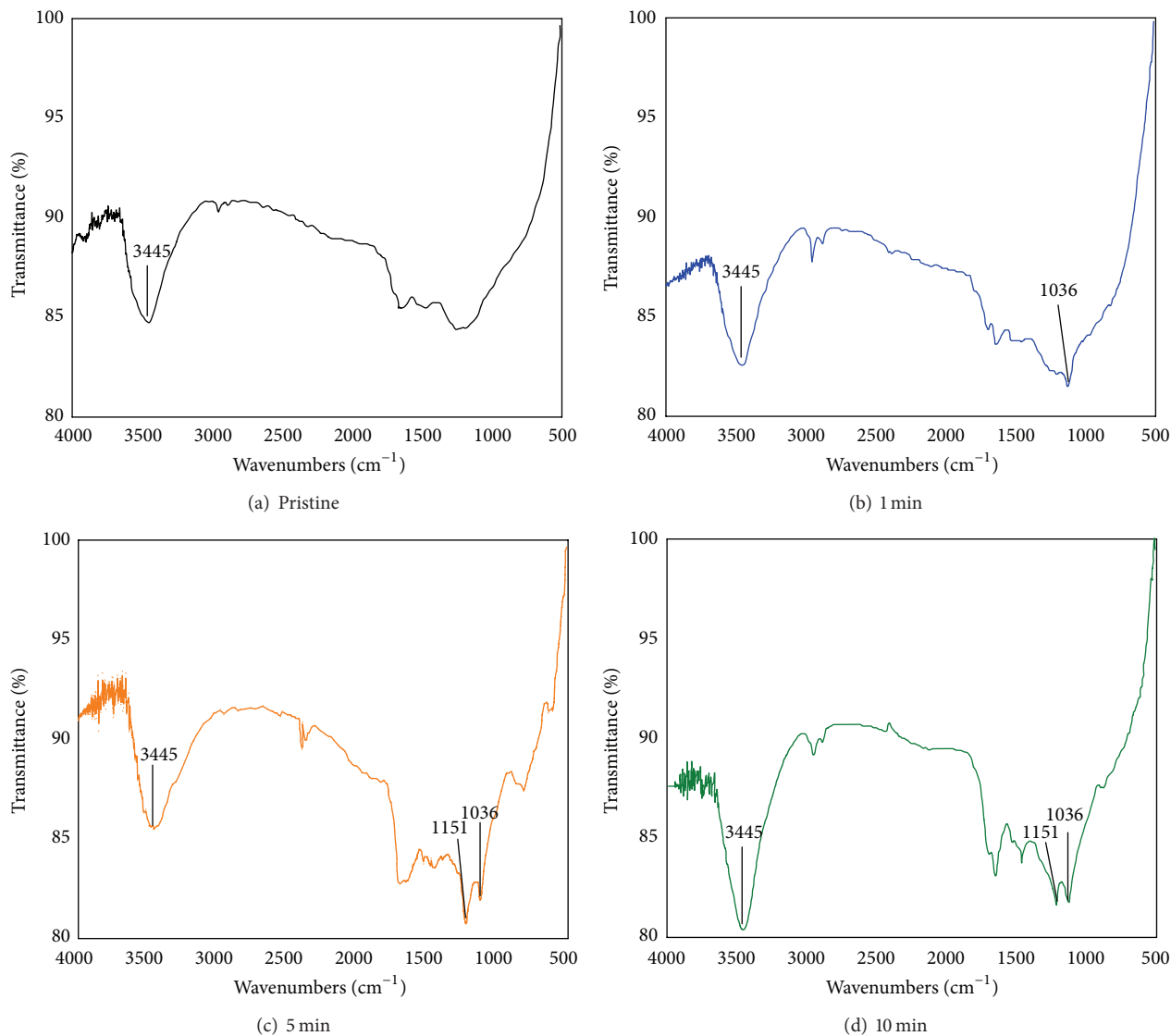


FIGURE 4: Infrared spectra of pristine and modified MWNTs.

and those generated by  $\text{CF}_4$  plasma etching for 1, 5, and 10 min with a Nicolet 5DXC FT-IR spectrometer.

Diverse functional groups and types of bonding were observed in the FTIR spectra of MWNTs (Figure 4). The absorption peaks at  $3445\text{ cm}^{-1}$  corresponded to the  $-\text{OH}$  groups in pristine and treated nanotubes. The absorption peaks at  $1036$  and  $1151\text{ cm}^{-1}$  were ascribed to the respective C-F and symmetric  $-\text{CF}_2$  stretching vibrations because of the  $\text{CF}_4$ -plasma treatment.

**3.2. SEM Analysis.** The surface morphologies of the pristine and plasma-treated MWNTs were analyzed using Zeiss Auriga focused ion beam and double-beam emission scanning electron microscopy (SEM). The SEM images of pristine MWNTs (Figure 5(a)) indicated the presence of several small particles, which included amorphous carbons and residual catalysts during preparation. Figures 5(b) and 5(c) show the SEM images of  $\text{CF}_4$  plasma treated for 10 min. The impurities

and dopant on the nanotube surfaces were removed, and MWNTs became shorter. Plasma treatment retained the nanotube structures.

### 3.3. Gas Sensing Properties of MWNTs Sensors to $\text{H}_2\text{S}$ and $\text{SO}_2$ .

We used eight kinds of MWNTs-based gas sensors (pristine MWNTs and MWNTs modified by plasma for different time) to detect  $\text{H}_2\text{S}$  and  $\text{SO}_2$  whose concentrations are 50 ppm for them both. The gas response curves are shown in Figure 6. It can be seen from Figures 6(a) and 6(b) that the sensitivity of pristine MWNTs and those modified by  $\text{CF}_4$  plasma for 0.5, 1, and 2 min to  $\text{H}_2\text{S}$  are 3%, 3.2%, 3.4%, and 3.5%, respectively, and to  $\text{SO}_2$  are 2.3%, 2.4%, 2.6%, and 2.7%. Obviously, after modification the gas sensitivities of MWNTs are not markedly enhanced. Under small discharge power, these phenomena may have been caused by the insufficient treatment time and poor surface modification. Therefore, if the discharge power remains unchanged, in order to achieve

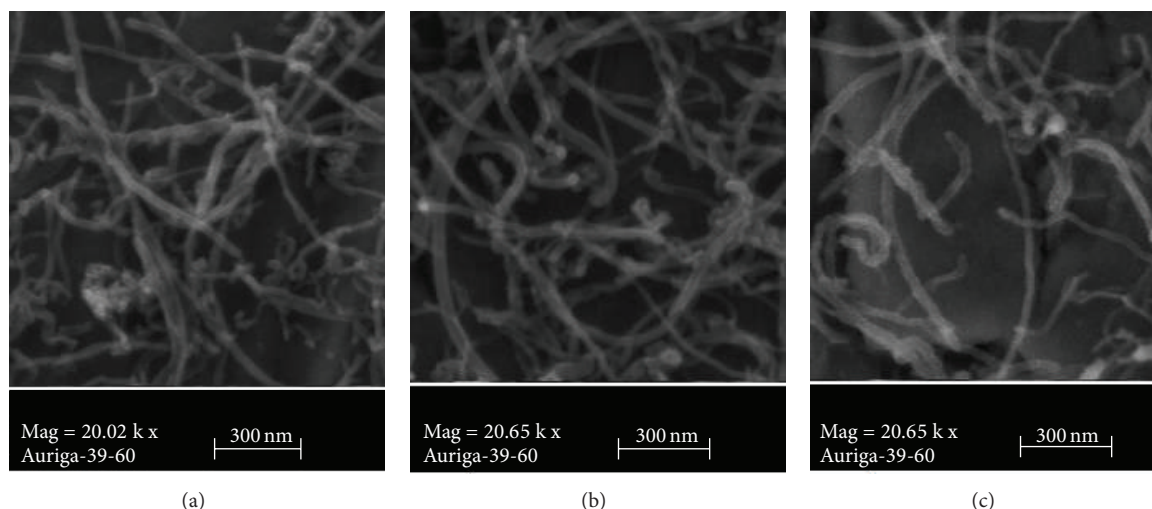


FIGURE 5: SEM images: (a) pristine and (b and c) modified MWNTs for 10 min.

a better surface modification plasma treatment time should be extended.

In consequence, Figures 6(c) and 6(d) show the response curves of pristine MWNTs and these treated for 5, 8, 10, and 12 min to  $\text{H}_2\text{S}$  and  $\text{SO}_2$ . We can see that when the treatment time is less than 10 min, the sensitivities of MWNTs sensors increased with increasing of treatment time. Meanwhile, the MWNTs modified by  $\text{CF}_4$  plasma for 10 min exhibited the best sensitivity to both  $\text{H}_2\text{S}$  and  $\text{SO}_2$ . However, the sensitivities decreased when the treatment time is over 10 min. Possible reasons may be that after longer treatment time the structure of the nanotubes was destroyed and nanotubes were partly carbonized [21] under the bombardment of energetic particles in prolonged plasma treatments, which result in a reduction of active adsorption sites on MWNTs surface for gas molecules. Hence, the gas sensing properties of the MWNTs were affected.

Figure 6 reveals that the response time of  $\text{CF}_4$  plasma-modified MWNTs sensors to  $\text{H}_2\text{S}$  and  $\text{SO}_2$  was shorter. For treatment times ranging from 0 min to 10 min, the response time decreased with increasing treatment time. Besides, the shortest response times to  $\text{H}_2\text{S}$  and  $\text{SO}_2$  are 70 and 150 s, respectively.

**3.4. Responses of MWNTs-Based Sensors to  $\text{H}_2\text{S}$  and  $\text{SO}_2$  at Different Concentrations.** MWNT sensors modified by  $\text{CF}_4$  plasma for 10 min (Section 3.3) were selected to detect  $\text{H}_2\text{S}$  and  $\text{SO}_2$  at 10, 25, 50, and 100 ppm because these sensors yielded the best sensitivities. Figures 7(a) and 7(b) indicate that the sensitivity of the sensors increases with the gas concentration.

Figure 8 shows that the gas concentration and sensor sensitivity were linearly correlated for  $\text{H}_2\text{S}$  and  $\text{SO}_2$  concentrations of 10 ppm to 100 ppm with correlation coefficients ( $R^2$ ) of 0.97183 and 0.9739, respectively.

**3.5. Desorption and Repeatability of MWNTs-Based Sensors.** To analyze the desorption properties of modified MWNTs

gas sensors, these modified by  $\text{CF}_4$  plasma for 10 min were chosen to test the recovery curve, as shown in Figure 9. The experiment steps are as follows. Firstly, the chamber was pumped into vacuum and was standing for a period of time. After resistance of the sensor remains unchanged, in the second minute 50 ppm  $\text{H}_2\text{S}$  was introduced into the chamber and the resistance showed a quick decrease. Few minutes later, the resistance of sensor remains stable. Currently,  $\text{H}_2\text{S}$  gas molecules reach adsorption equilibrium at the surface of MWNTs. In the fifth minute, pure  $\text{N}_2$  was injected into the gas chamber, and the sensor resistance can generally recover near the initial value. There is still a small amount of residual gas accumulating on the surface of the sensor which affects the sensitivity. In order to obtain a complete desorption, place the sensor under UV irradiation. By irradiating with UV light, the residual gas absorbs energy, which enables it to “escape” from the “trapped” state where almost no residual gas remains on the surface of the tested sensor. After  $\text{N}_2$  and UV treatments, the sensor resistance was gradually restored to its initial value. The recovery time was about 25 min, which was less than that of the pristine MWNTs sensor to  $\text{H}_2\text{S}$  (40 min; data not shown).

The MWNTs sensor modified by plasma for 10 min that was most sensitive to  $\text{SO}_2$  was selected to illustrate the repeatability process (Figure 10). The resistance-change trends remained similar, and the maximum resistance-change rate remained the same and stable. Hence, the gas sensor could be repeatedly used with good response and stability. However, the recovery time was approximately 35 min and was not greatly enhanced in contrast to that of pristine MWNT-based sensors.

**3.6. Gas Sensing Mechanism.** The  $\text{CF}_4$ -plasma-modified MWNTs sensors exhibited high sensitivities to  $\text{H}_2\text{S}$  and  $\text{SO}_2$  because of the following reasons: (1) the accelerated electrons, ions, and free radicals cleaned the MWNT surface by etching some amorphous carbon and catalyst particles during plasma treatment; (2) the bombardment of energetic particles

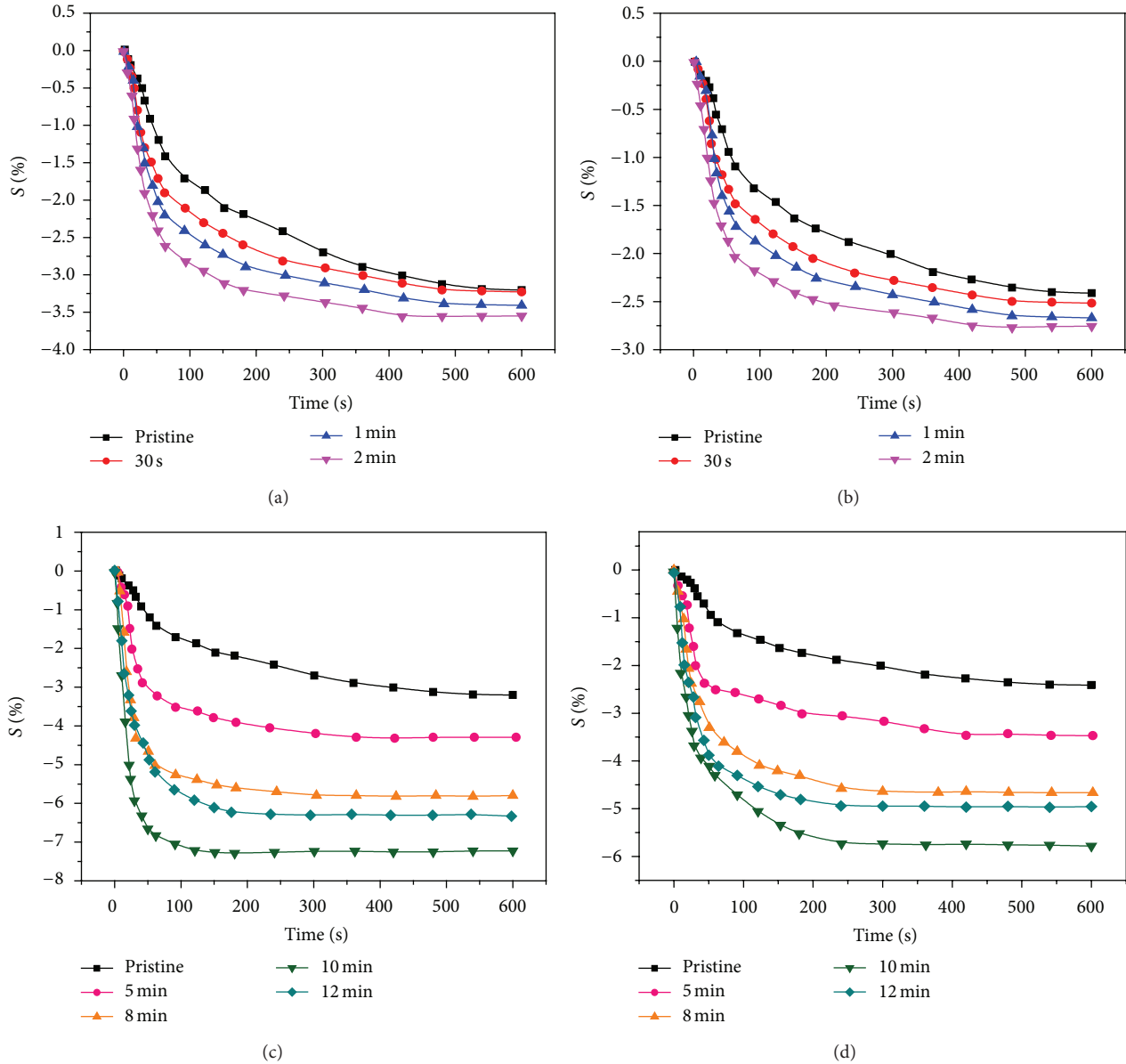


FIGURE 6: Responses of MWNTs-based gas sensors: (a, c) 50 ppm  $H_2S$  and (b, d) 50 ppm  $SO_2$ .

destroyed some of the nanotubes and increased the defects on their surfaces, which generated effective adsorption sites for gas molecules; and (3)  $CF_4$ , a fluorinated gas [22], was ionized to generate fluoride ions in DBD and react with carbon atoms on the MWNTs surface to yield C-F bonds [23] without destroying the tubular structure. Given the strong polarity and reactivity of F atoms, fluorinated MWNTs exhibited strong adsorption capacities and high gas sensing properties.

The response and recovery time of plasma-modified MWNT sensors to  $H_2S$  were remarkably reduced, but only the response time to  $SO_2$  decreased, and recovery time was not reduced (Section 3.5). Theoretically,  $H_2S$  molecules were physically adsorbed on the surface of MWNTs through van der Waals interaction. However, some hydroxyls existed on the surfaces of the nanotubes during growth by CVD. F

atoms were introduced onto the MWNTs surface after fluorination. C-F bonds possessed high polarity because of the strong electronegativity of the F atom, during which -F was essential. Stable hydrogen bonds (C-F...H-S) were formed between H atoms in  $H_2S$  molecules and F atoms when  $H_2S$  molecules were adsorbed on the surface of modified MWNTs. Subsequently, the van der Waals forces were replaced, and the adsorption of  $H_2S$  molecules was accelerated to reduce the response time (Figure 11(a)). In addition, O atoms in the hydroxyl groups in MWNTs surfaces exhibited small atomic radii and high electronegativities. Hydrogen bonds (C-O...H-S) were formed between O atoms in hydroxyl and H atoms in  $H_2S$  molecules (Figure 11(a)). The recovery time of plasma-based MWNTs sensors to  $H_2S$  decreased possibly because of the effect of UV irradiation that the H-F

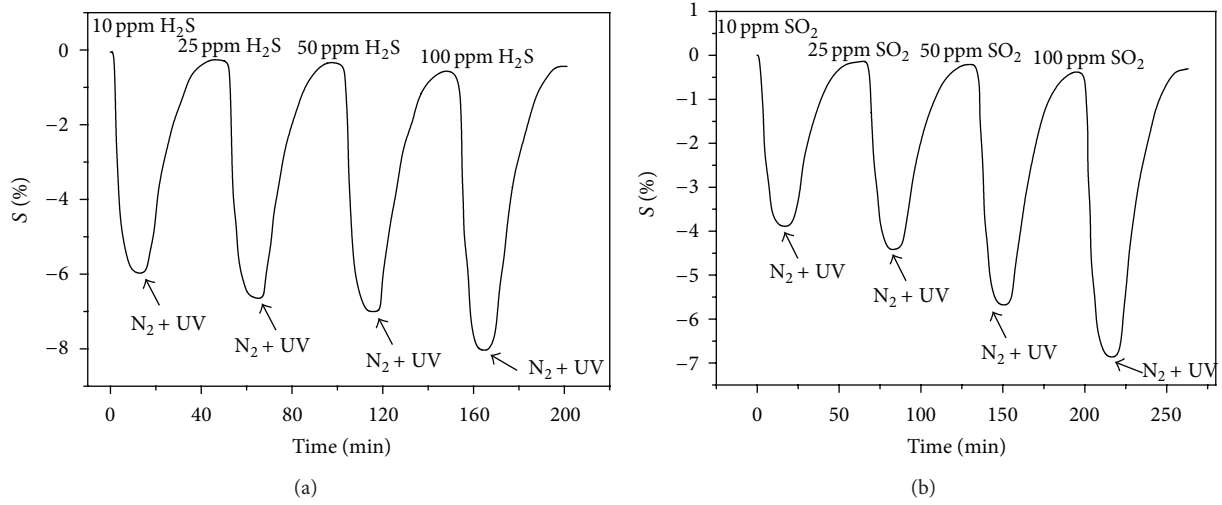


FIGURE 7: Response curves of MWNTs-based sensors to different concentrations of (a)  $H_2S$  and (b)  $SO_2$ .

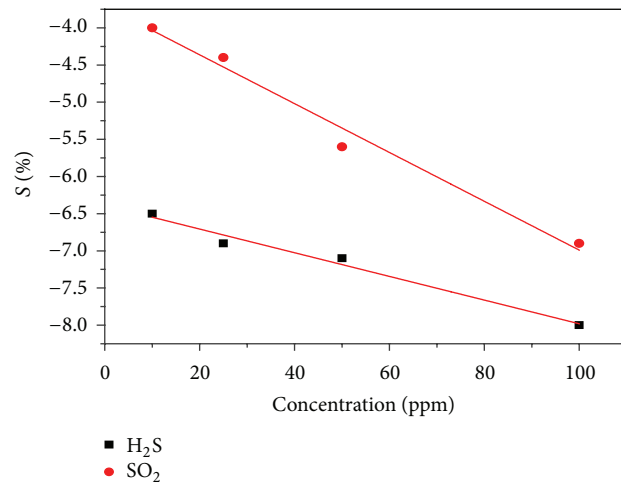


FIGURE 8: Linear relationship sensitivity of MWNT-based sensors for different concentrations of  $SO_2$  and  $H_2S$ .

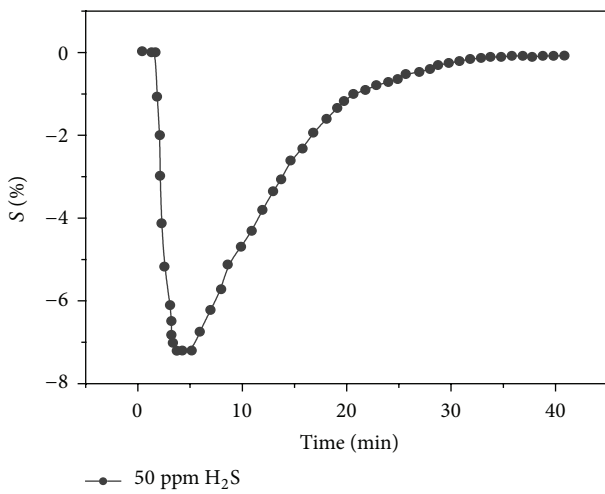


FIGURE 9: Recovery curve of plasma-modified MWNTs to  $H_2S$ .

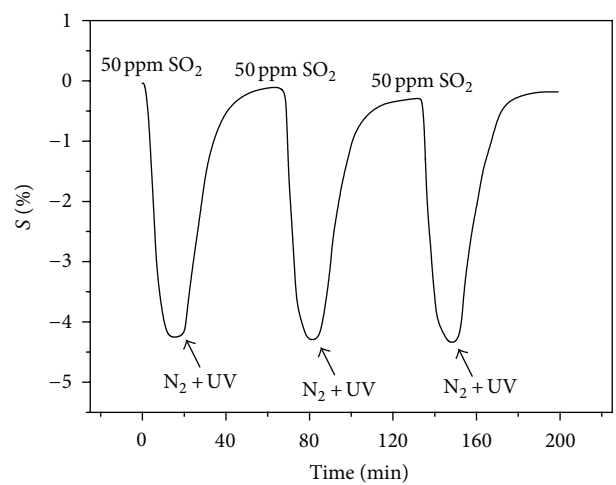


FIGURE 10: Reversibility curve of modified MWNTs to 50 ppm  $SO_2$ .

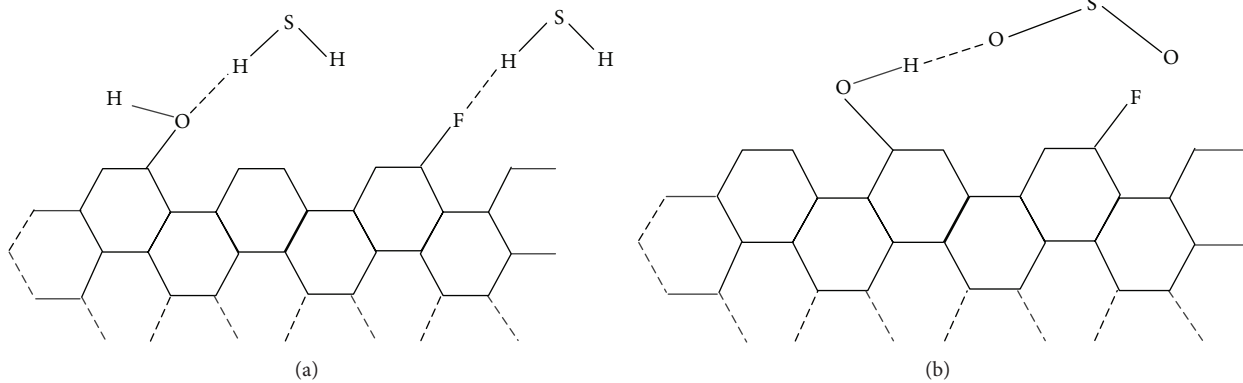


FIGURE 11: Schematic of the absorption of (a)  $\text{H}_2\text{S}$  and (b)  $\text{SO}_2$  in modified MWNTs.

bond is easier to disintegrate. For  $\text{SO}_2$ , only O atoms in the  $\text{SO}_2$  molecules and H atoms of hydroxyl were combined to form hydrogen bonds ( $\text{O}-\text{H}\cdots\text{O}-\text{S}$ ; Figure 11(b)). F atoms on the surfaces of modified MWNT increased the number of effective adsorption sites for gas molecules, accelerated the adsorption, and reduced the response time. However, the recovery time remained invariant.

#### 4. Conclusions

MWNTs were modified by DBD  $\text{CF}_4$  plasma for 0.5, 1, 2, 5, 8, 10, and 12 min. The gas sensitivities of the treated MWNTs sensors to  $\text{H}_2\text{S}$  and  $\text{SO}_2$  were evaluated. The following conclusions were drawn.

- (1) Modification effects were closely related to the treatment time under a small plasma discharge power. The gas sensitivities of MWNTs did not improve significantly under short treatment times compared with those of pristine counterparts.
- (2) For <10 min treatment times, the sensitivities of MWNT sensors increased with the treatment time. MWNTs treated for 10 min exhibited the best sensitivity to  $\text{H}_2\text{S}$  and  $\text{SO}_2$  with good recovery and stability.
- (3) SEM micrographs and FTIR analyses of pristine and modified MWNTs revealed that modified MWNTs contained a low number of impure particles on the surface as well as short length and grafted  $-\text{F}$  polar functional groups. Hence, gas adsorption was highly convenient for the nanotubes, and gas sensitivity was improved.

#### Conflict of Interests

The authors declare that there is no conflict of interests regarding the publication of this paper.

#### Acknowledgments

The authors gratefully acknowledge the financial support from National Natural Science Foundation of P. R. China (Project no. 51277188), New Century Excellent Talents in

University Program (NCET-12-0590), and Project Supported by the Funds for Innovative Research Groups of China (51321063).

#### References

- [1] Y. Martin, Z. Li, T. Tsutsumi et al., "Detection of  $\text{SF}_6$  decomposition products generated by DC corona discharge using a carbon nanotube gas sensor," *IEEE Transactions on Dielectrics and Electrical Insulation*, vol. 19, no. 2, pp. 671–676, 2012.
- [2] X. Zhang, J. Ren, J. Tang, and C. Sun, "Kernel statistical uncorrelated optimum discriminant vectors algorithm for GIS PD recognition," *IEEE Transactions on Dielectrics and Electrical Insulation*, vol. 16, no. 1, pp. 206–213, 2009.
- [3] C. Beyer, H. Jenett, and D. Klockow, "Influence of reactive  $\text{SF}_x$  gases on electrode surfaces after electrical discharges under  $\text{SF}_6$  atmosphere," *IEEE Transactions on Dielectrics and Electrical Insulation*, vol. 7, no. 2, pp. 234–240, 2000.
- [4] M. Piemontesi and L. Niemeyer, "Sorption of  $\text{SF}_6$  and  $\text{SF}_6$  decomposition products by activated alumina and molecular sieve 13X," in *Proceedings of the IEEE International Symposium on Electrical Insulation*, pp. 828–838, IEEE, Quebec, Canada, June 1996.
- [5] X. X. Zhang, W. T. Liu, J. Tang, and P. Xiao, "Study on PD detection in  $\text{SF}_6$  using multi-wall carbon nanotube films sensor," *IEEE Transactions on Dielectrics and Electrical Insulation*, vol. 17, no. 3, pp. 833–838, 2010.
- [6] R. J. Van Brunt, "Production rates for oxy-fluorides  $\text{SOF}_2$ ,  $\text{SO}_2\text{F}_2$  and  $\text{SOF}_4$  in  $\text{SF}_6$  corona discharges," *Journal of Research of the National Bureau of Standards*, vol. 90, no. 3, pp. 229–253, 1985.
- [7] J. M. Braun, F. Y. Chu, and R. Seethapathy, "Characterization of GIS spacers exposed to  $\text{SF}_6$  decomposition products," *IEEE transactions on electrical insulation*, vol. 22, no. 2, pp. 187–193, 1986.
- [8] X.-X. Zhang, Y. Yao, J. Tang, C.-X. Sun, and L.-Y. Wan, "Actuamity and perspective of proximate analysis of  $\text{SF}_6$  decomposed products under partial discharge," *High Voltage Engineering*, vol. 34, no. 4, pp. 664–747, 2008.
- [9] X. X. Zhang, C. C. Luo, and J. Tang, "Sensitivity characteristic analysis of adsorbent-mixed carbon nanotube sensors for the detection of  $\text{SF}_6$  decomposition products under PD conditions," *Sensors (Switzerland)*, vol. 13, no. 11, pp. 15209–15220, 2013.

- [10] I. A. Metwally, "Status review on partial discharge measurement techniques in gas-insulated switchgear/lines," *Electric Power Systems Research*, vol. 69, no. 1, pp. 25–36, 2004.
- [11] A. Derdouri, J. Casanovas, R. Hergli, R. Grob, and J. Mathieu, "Study of the decomposition of wet SF<sub>6</sub>, subjected to 50-Hz ac corona discharges," *Journal of Applied Physics*, vol. 65, no. 5, pp. 1852–1857, 1989.
- [12] H. M. Heise, R. Kurte, P. Fischer, D. Klockow, and P. R. Janissek, "Gas analysis by infrared spectroscopy as a tool for electrical fault diagnostics in SF<sub>6</sub> insulated equipment," *Fresenius' Journal of Analytical Chemistry*, vol. 358, no. 7-8, pp. 793–799, 1997.
- [13] C. T. White and T. N. Todorov, "Carbon nanotubes as long ballistic conductors," *Nature*, vol. 393, no. 6682, pp. 240–241, 1998.
- [14] P. G. Collins, K. Bradley, M. Ishigami, and A. Zettl, "Extreme oxygen sensitivity of electronic properties of carbon nanotubes," *Science*, vol. 287, no. 5459, pp. 1801–1804, 2000.
- [15] P. Qi, O. Vermesh, M. Grecu et al., "Toward large arrays of multiplex functionalized carbon nanotube sensors for highly sensitive and selective molecular detection," *Nano Letters*, vol. 3, no. 3, pp. 347–351, 2003.
- [16] J. Kong, N. R. Franklin, C. Zhou et al., "Nanotube molecular wires as chemical sensors," *Science*, vol. 287, no. 5453, pp. 622–625, 2000.
- [17] P. Slobodian, P. Riha, A. Lengalova, P. Svoboda, and P. Saha, "Multi-wall carbon nanotube networks as potential resistive gas sensors for organic vapor detection," *Carbon*, vol. 49, no. 7, pp. 2499–2507, 2011.
- [18] R. Leghrib, A. Felten, F. Demoisson, F. Reniers, J.-J. Pireaux, and E. Llobet, "Room-temperature, selective detection of benzene at trace levels using plasma-treated metal-decorated multi-walled carbon nanotubes," *Carbon*, vol. 48, no. 12, pp. 3477–3484, 2010.
- [19] K.-Y. Dong, D.-J. Ham, B. H. Kang et al., "Effect of plasma treatment on the gas sensor with single-walled carbon nanotube paste," *Talanta*, vol. 89, pp. 33–37, 2012.
- [20] X. X. Zhang, B. Yang, X. J. Wang, and C. C. Luo, "Effect of plasma treatment on multi-walled carbon nanotubes for the detection of H<sub>2</sub>S and SO<sub>2</sub>," *Sensors (Switzerland)*, vol. 12, no. 7, pp. 9375–9385, 2012.
- [21] A. Felten, C. Bittencourt, J. J. Pireaux, G. van Lier, and J. C. Charlier, "Radio-frequency plasma functionalization of carbon nanotubes surface O<sub>2</sub>, NH<sub>3</sub>, and CF<sub>4</sub> treatments," *Journal of Applied Physics*, vol. 98, no. 7, Article ID 074308, 2005.
- [22] L. Valentini, D. Puglia, I. Armentano, and J. M. Kenny, "Sidewall functionalization of single-walled carbon nanotubes through CF<sub>4</sub> plasma treatment and subsequent reaction with aliphatic amines," *Chemical Physics Letters*, vol. 403, no. 4–6, pp. 385–389, 2005.
- [23] Y. M. Shulga, T.-C. Tien, C.-C. Huang et al., "XPS study of fluorinated carbon multi-walled nanotubes," *Journal of Electron Spectroscopy and Related Phenomena*, vol. 160, no. 1–3, pp. 22–28, 2007.

## Research Article

# Synergetic Effects of Mechanical Properties on Graphene Nanoplatelet and Multiwalled Carbon Nanotube Hybrids Reinforced Epoxy/Carbon Fiber Composites

Pin-Ning Wang,<sup>1</sup> Tsung-Han Hsieh,<sup>2</sup> Chin-Lung Chiang,<sup>3</sup> and Ming-Yuan Shen<sup>4</sup>

<sup>1</sup>Department of Creative Fashion Design, Taoyuan Innovation Institute of Technology, Jhongli, Taoyuan 32091, Taiwan

<sup>2</sup>Department of Mold and Die Engineering, National Kaohsiung University of Applied Science, Kaohsiung 80778, Taiwan

<sup>3</sup>Department of Safety, Health and Environmental Engineering, Hung Kuang University, Taichung 43302, Taiwan

<sup>4</sup>Department of Aviation Mechanical Engineering, China University of Science and Technology, Hsinchu 31241, Taiwan

Correspondence should be addressed to Ming-Yuan Shen; hbj678@gmail.com

Received 24 September 2014; Revised 11 January 2015; Accepted 12 January 2015

Academic Editor: Myoung-Woon Moon

Copyright © 2015 Pin-Ning Wang et al. This is an open access article distributed under the Creative Commons Attribution License, which permits unrestricted use, distribution, and reproduction in any medium, provided the original work is properly cited.

Graphene nanoplatelets (GNPs) and carbon nanotubes (CNTs) are novel nanofillers possessing attractive characteristics, including robust compatibility with most polymers, high absolute strength, and cost effectiveness. In this study, an outstanding synergetic effect on the graphene nanoplatelets (GNPs) and multiwalled carbon nanotubes (CNTs) hybrids were used to reinforce epoxy composite and epoxy/carbon fiber composite laminates to enhance their mechanical properties. The mechanical properties of CNTs/GNPs hybrids on a fixed weight fraction (1 wt%) with mixing different ratio reinforced epoxy nanocomposite, such as ultimate tensile strength and flexure properties, were investigated. The mechanical properties of epoxy/carbon fiber composite laminates containing different proportions of CNTs/GNPs hybrids (0.5, 1.0, 1.5 wt%) were increased over that of neat laminates. Consequently, significant improvement in the mechanical properties was attained for these epoxy resin composites and carbon fiber-reinforced epoxy composite laminates.

## 1. Introduction

CNTs are one-dimensional carbon nanomaterials that possess high strength, high flexibility, low mass density, and large aspect ratio [1]. CNTs have a unique combination of mechanical, electrical, and thermal properties that render them excellent candidates to substitute or complement conventional nanofillers in fabricating multifunctional polymer nanocomposites [2–4]. However, the development of CNT reinforced polymer nanocomposites has been impeded by their cost and aggregation in polymer matrix. CNTs tend to agglomerate due to their large aspect ratio and Van der Waals forces, which leads to their dispersion difficultly in polymer matrix [5].

The GNPs planar structure provides a two-dimensional path for phonon transport, and the ultrahigh surface area allows a large surface contact area with polymer resulting in enhancement of the composite thermal conductivity [6–8].

However, the large surface area between GNPs which is GNP planar nanosheets results in large Van der Waals forces and strong  $\pi$ - $\pi$  interactions [9–11]. Thus, the performance of GNPs based polymer composites is limited by the aggregation and stacking of GNP sheets. Since the physicochemical properties of aggregated GNPs are similar to those of graphite with its relatively low-specific surface area, the performance of GNPs will suffer significantly from reduced performance. This is an important issue if GNPs potential as a polymer composite reinforcing materials is realized [12, 13].

Epoxy is widely applied in advanced carbon fiber reinforced plastic (CFRP) due to their good mechanical performance, process-ability, compatibility with most fibers, chemical resistance, wear resistance, and low cost. However, these materials are relatively brittle, which is detrimental to the interlaminar properties between matrix and reinforcement. The addition of CNTs or GNPs to improve the interfacial

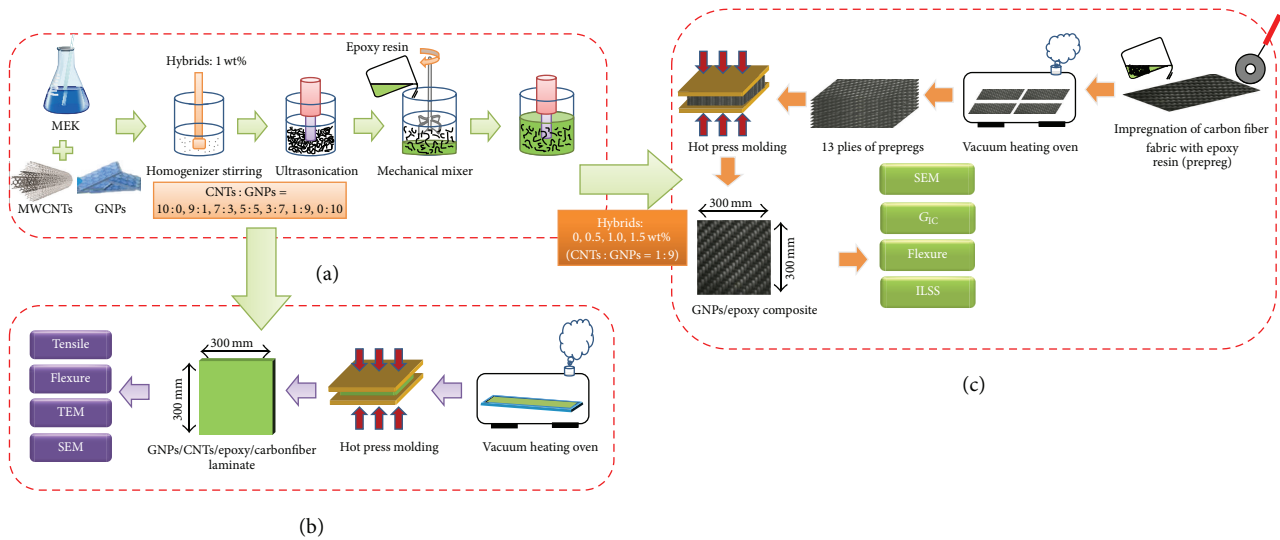


FIGURE 1: A schematic illustration of the fabrication of composites: (a) CNTs/GNPs/epoxy resin solution; (b) CNTs/GNPs/epoxy nanocomposites; (c) CNTs/GNPs/epoxy/carbon fiber composite laminates.

strength of laminates has been demonstrated. Adding carbon base nanofillers, such as CNTs and GNPs, can improve mechanical properties of polymer composites, due to their unique nanostructures, and superior properties.

In our previous research [14], GNPs were used to reinforce epoxy composite and epoxy/carbon fiber composite laminates to enhance their mechanical properties. The mechanical properties of GNPs/epoxy nanocomposite, such as ultimate tensile strength and flexure properties, were investigated.

To the best of our knowledge, very few studies have so far been reported on the fabrication of CNTs/GNPs hybrids reinforced CFRP composites using manufacturing of prepregs [15]. GNPs and CNTs are difficult to process because of the issues associated with agglomeration and lack of interfacial interactions with polymers. None of the previous studies, nevertheless, have given due attention to the influence of adding CNTs/GNPs hybrids on the solvent type prepreg process. Therefore, it is necessary to understand the role of adding CNTs/GNPs hybrids into the polymer matrix, which will largely affect the impregnation of fibres and prepreg processing conditions.

In this study, epoxy resin containing uniformly dispersed 1 wt% CNTs/GNPs hybrids with different mixing ratio (i.e., 10:0, 9:1, 7:3, 5:5, 3:7, 1:9, and 0:10) and prepared the CNTs/GNPs/epoxy nanocomposites. Mechanical properties of the nanocomposite, including ultimate tensile strength, flexural strength, and flexural modulus, were investigated.

The solution of epoxy resin containing the fixed mixing ratio of CNTs/GNPs hybrids (1:9) on the different contents (i.e., 0, 0.5, 1.0, and 1.5 wt%) permeate through a carbon fiber cloth was used to prepare the epoxy/carbon fiber composite laminates. The process was used to investigate if CNTs/GNPs hybrids improved the mechanical properties of carbon fiber-reinforced epoxy resin composite laminates.

Finally, the fracture surface of the specimen was investigated using scanning electron microscopy (SEM) and transmission electron microscopy (TEM) to determine the role of adding CNTs/GNPs hybrids into the epoxy and epoxy/carbon fibers composite laminates.

## 2. Experimental

**2.1. Preparation of CNTs/GNPs/Epoxy Resin Solution.** The maleic anhydride, MA, was used to modify carbon nanomaterials. Graphene nanoplatelets, GNPs with a thickness of 5–25 nm are obtained from Xiamen Knano Graphene Technology Co., Ltd. China. Multiwalled carbon nanotubes, CNTs, with 1–25  $\mu\text{m}$  in length and 20 nm in diameter are obtained from Nanocyl Co., Ltd. Belgium. The GNPs and CNTs were modified by Hanyu Material Co., Ltd. Taiwan. The CNTs/GNPs hybrids were used for reinforcement in this study. The CNTs/GNPs/methyl ethyl ketone (MEK) solution was stirred for 10 minutes using a homogenizer. The solution was then vibrated by ultrasonication for 90 minutes to enable the CNTs/GNPs hybrids to disperse uniformly throughout the MEK solution. The CNTs/GNPs/MEK solution was mixed with epoxy resin and hardener (EPO-622 epoxy resin and 2-ethyl-4-methylimidazole hardener, Epotech Composite Co., Ltd, Taiwan) for 90 minutes using a mechanical stirrer and then vibrated by ultrasonication for 90 minutes to enable the CNTs/GNPs hybrids to disperse uniformly throughout the epoxy solution. A schematic illustration of the fabrication of the CNTs/GNPs/epoxy resin is shown in Figure 1(a).

**2.2. Preparation of CNTs/GNPs/Epoxy Nanocomposites.** The CNTs/GNPs/epoxy resin solution was placed in a heating oven for exposure at 83°C for three hours to evaporate all of the solvent and then placed in a vacuum heating oven and vacuum pumping was performed for 5 minutes

to eliminate air bubbles. The resin solution was poured into molds and then placed on a hot press machine to form the CNTs/GNPs/epoxy nanocomposites (pressed at 1500 psi and 150°C for 30 minutes). The nanocomposites were then placed in a heating oven at 140°C for 3 hours to eliminate the internal stress (postcure). A schematic illustration of the fabrication of the CNTs/GNPs/epoxy nanocomposite is shown in Figure 1(b).

### 2.3. Preparation of CNTs/GNPs/Epoxy/Carbon Fiber Composite Laminates

**2.3.1. Impregnation of Carbon Fiber Fabric with Epoxy Resin (Prepreg).** A piece of 3 k carbon fiber fabric of the desired dimensions was placed on a release paper and the MEK/CNTs/GNPs/epoxy resin solution was evenly permeated on it. The carbon fiber fabric with uniformly dispersed MEK/CNTs/GNPs/epoxy resin (prepreg) was then placed in a heating oven for exposure at 83°C for three hours to evaporate all of the solvent.

**2.3.2. Hot Press Molding and Postcuring.** Thirteen pieces of prepregs were piled in a mold and placed on a hot press machine to prepare a CNTs/GNPs/epoxy/carbon fiber composite laminate (pressed at 1500 psi and 150°C for 30 mins). The composite laminate was then placed in a heating oven at 140°C for three hours to eliminate the internal stress of laminate (postcure) [16]. A schematic illustration of the fabrication of the composite laminate is shown in Figure 1(c).

### 2.4. Experimental Process

**2.4.1. Experimental Process of CNTs/GNPs/Epoxy Nanocomposites.** CNTs/GNPs hybrids reinforced epoxy nanocomposites containing the fixed weight fraction of CNTs/GNPs hybrids (1 wt%) with different mixing ratio (i.e., 10 : 0, 9 : 1, 7 : 3, 5 : 5, 3 : 7, 1 : 9, and 0 : 10) were fabricated. The mechanical properties of the nanocomposites, such as ultimate tensile strength, flexural strength, and flexural modulus, were investigated.

The fracture surface of the specimen was investigated using transmission electron microscopy (TEM) and field emission scanning electron microscopy (FESEM) to determine the dispersion of the CNTs/GNPs hybrids in the nanocomposites.

**2.4.2. Experimental Process of Composite Laminates.** CNTs/GNPs hybrids reinforced epoxy/carbon fiber composite laminates containing the fixed mixing ratio (1 : 9) and adding three proportions of CNTs/GNPs hybrids (i.e., 0.5, 1.0, and 1.5 wt%) were fabricated. The mechanical properties of the composite laminates, such as flexure properties and interlaminar shear strength, ILSS, were investigated. A double cantilever beam (DCB) specimen was employed using corrected beam theory (CBT) method for calculating  $G_{IC}$  (Mode I) in order to determine interlaminar fracture toughness evaluation of composite laminates without and with CNTs/GNPs hybrids added.

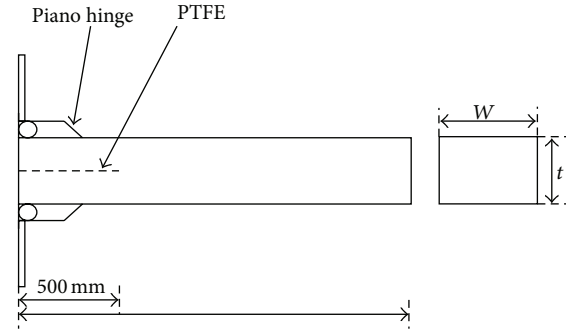


FIGURE 2: The schematic representation of the DCB specimen for Mode I ( $G_{IC}$ ) test.

The fracture surface of the specimens was investigated using SEM to determine if the CNTs/GNPs hybrids would prevent the formation of pores in the laminates and makes CNTs/GNPs hybrids effective in delivering stress to improve the mechanical properties of composite laminates.

**2.4.3.  $G_{IC}$  Test of Composite Laminates.** Double cantilever beam (DCB) tests were used to determine the fracture resistant under Mode I opening load, in which Mode I delamination fracture energy,  $G_{IC}$ , can be followed from the British Standard, BS7991:2001. Specimen geometries were controlled to be 165 mm long beams with a 20 mm width and 3 mm thick. The specimen was prepared with a pre-inserted starter crack by a 60  $\mu$ m thick nonstick film made of polytetrafluoroethylene (PTFE) to make a delamination length of 50 mm from load line, as shown in Figure 2. Two steel-alloy loading-piano hinges were bonded on either side of the specimen. DCB tests require that load, displacement, and crack length measurements are taken. To compare the  $G_{IC}$  of various amounts of CNTs/GNPs hybrids reinforced epoxy/carbon fiber composite laminates, the  $G_{IC}$  when stable crack growth reached 50 mm from the load line (i.e., the end of insert PTFE precrack) was designated as the initial  $G_{IC}$  value ( $G_{IC}$ -init).  $G_{IC}$ -init was used to analyze the influence of mixed carbon nanomaterials on the fracture toughness of epoxy resin/carbon fiber composite laminates.

$G_{IC}$  was initially calculated by using the area method [17], which represents the area under the load-displacement curve. Area method is based on linear fracture mechanics simple beam theory, which assumes a perfectly built-in DCB specimen:

$$G_{IC} = \frac{3P\delta}{2ba}, \quad (1)$$

where  $P$  is the load (N),  $\delta$  is the crack opening displacement (mm),  $b$  is the specimen width (mm), and  $a$  is the delamination length (mm). However, this underestimates the compliance ( $C = \delta/P$ ) as the beam is not perfectly built-in. A means of correcting this effect is to apply a slightly longer delamination length of  $\alpha + |\Delta|$ . The  $|\Delta|$  is found experimentally by plotting the cube root of compliance ( $C^{1/3}$ ) against delamination length ( $\alpha$ ). The extrapolation of a linear fit through data yields  $\Delta$  as the  $x$ -axis intercept.

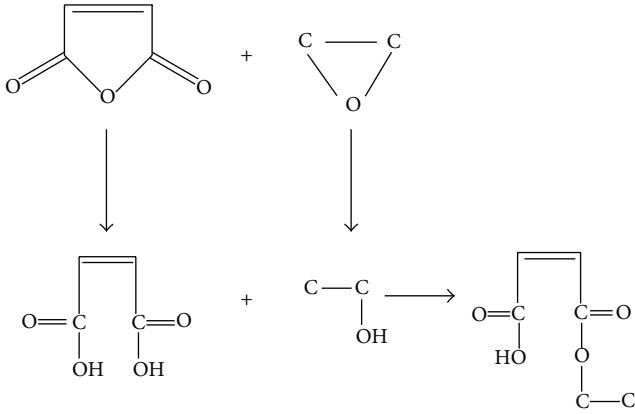


FIGURE 3: Reaction of maleic anhydride and epoxide group.

The delamination propagation values from Mode I pre-crack were used for the linear fit data. In addition, large displacement correction ( $F$ ) was applied for all specimens, which contributed significantly if the  $\delta/p$  ratio was larger than 0.4. This method of calculating  $G_{IC}$  is known as corrected beam theory (CBT). All initiation and propagation values were calculated according to

$$G_{IC} = \frac{3P\delta}{2b(a + |\Delta|)}F. \quad (2)$$

### 3. Results and Discussion

**3.1. Characterization of CNTs and GNPs.** Figure 3 shows the reaction of maleic anhydride (MA) and the epoxide group. This confirmed that MA can react with epoxy resin reinforcing the interfacial strength between carbon nanomaterials and the resin. The Fourier transform infrared (FT-IR) spectra images were shown in Figures 4 and 5. FT-IR was utilized to characterize the modification of CNTs and GNPs powders. The figures showed that the key absorption peak near 1,600–1,850  $\text{cm}^{-1}$  was the  $-\text{C}=\text{O}$  functional group, a standard absorption peak of acid anhydrides; these results indicated the successful MA modification of GNPs and CNTs.

**3.2. Mechanical Properties of CNTs/GNPs/Epoxy Nanocomposites.** Figures 6–8 and Table 1 show the flexure properties and tensile strengths of nanocomposites with CNTs/GNPs hybrids for a fixed weight fraction (1 wt%). The mechanical properties with various mixture ratios of CNTs/GNPs hybrids were collectively superior to pure resin or single type of carbon nanomaterial reinforced resins (10 : 0 and 0 : 10). This is because the reaction of MA and epoxy resin effectively strengthened the interface between the carbon nanomaterials and the resin, noticeably increasing the mechanical properties of nanocomposites. After sufficient dispersion of CNTs/GNPs hybrids in nanocomposites, the CNTs were able to permeate between the GNPs. The GNPs were also able to infiltrate between the CNTs, forming complementary structures that are able to interact and prevent restacking as a result of Van der Waals attraction [18]. Thus, the mechanical

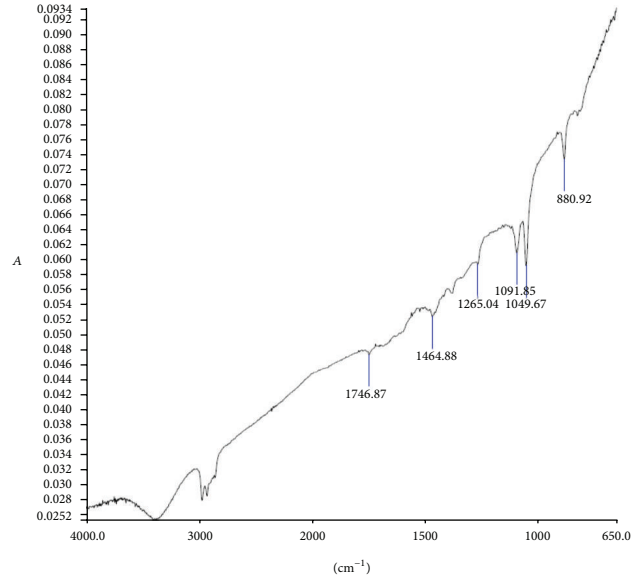


FIGURE 4: FT-IR spectra of CNTs-MA.

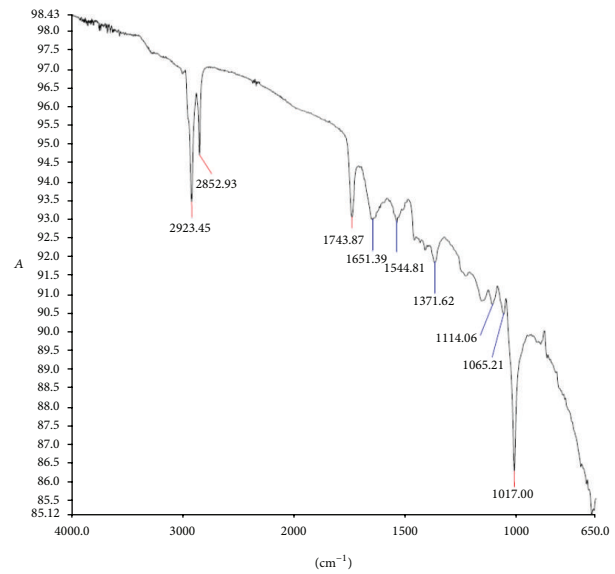


FIGURE 5: FT-IR spectra of GNPs-MA.

properties of nanocomposites containing 1 wt% CNTs/GNPs hybrids were collectively superior to nanocomposites containing 1 wt% single carbon nanomaterial and neat composite.

In Figures 7–9, when the CNTs/GNPs hybrids mixing ratios were 5 : 5 and 1 : 9 (1 wt%), the increase in mechanical properties were collectively greater than 20% of neat composite, thus inferring that these two mixing ratios can effectively inhibit the agglomeration of the two carbon nanomaterials and effectively reinforcing the epoxy resin. Two factors were proposed to explain the synergetic enhancement of CNTs/GNPs/epoxy composites: (1) flexible CNTs can construct GNPs to form 3D hybrid structure, which inhibit face to face aggregation of multigraphene platelets. This results

TABLE 1: Mechanical properties of CNTs/GNPs/epoxy nanocomposites with different carbon nanomaterials mixing ratio.

Test item (unit)	CNTs/GNPs hybrids content (fixed weight fraction: 1 wt%)							
	Neat	10:0	9:1	7:3	5:5	3:7	1:9	0:10
TS (MPa)	54.9	60.2	61.2	64.1	73.4	58.1	67.0	55.6
FS (MPa)	105.9	118.1	114.5	102.7	127.8	125.7	133.8	104.5
FM (GPa)	2.2	2.59	2.62	2.40	2.71	2.64	2.76	2.53

TS: tensile strength, FS: flexural strength, and FM: flexural modulus.

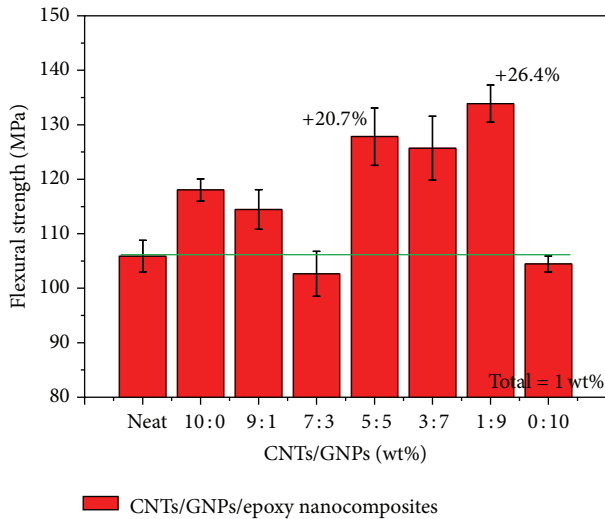


FIGURE 6: Flexural strength of CNTs/GNPs/epoxy nanocomposites.

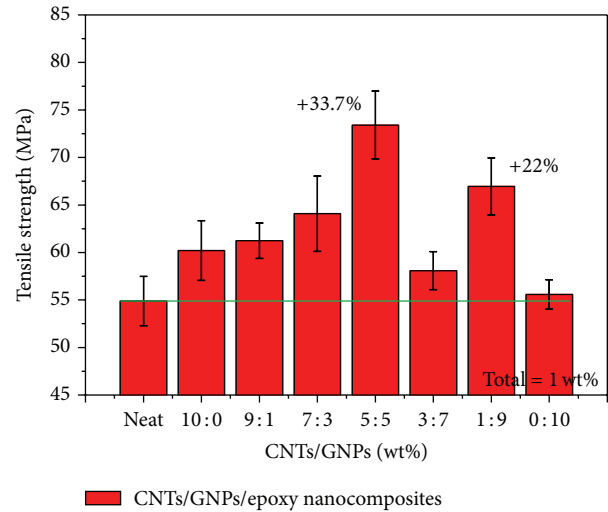


FIGURE 8: Tensile strength of CNTs/GNPs/epoxy nanocomposites.

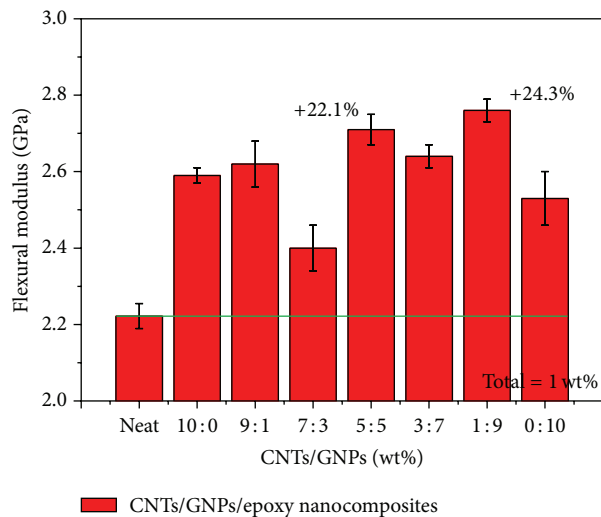


FIGURE 7: Flexural modulus of CNTs/GNPs/epoxy nanocomposites.

in a large surface area, thus increasing the contact surface area between CNTs/GNPs hybrids and epoxy matrix; (2) the CNTs can act as extended tentacles for the 3D hybrid architectures, which can become entangled with the polymer chain resulting in better interaction between CNTs/GNPs and the epoxy matrix [18].

However, the lower mechanical properties of nanocomposite with CNTs/GNPs hybrids mixing ratios were 7:3 and 0:10 (1 wt% of GNPs) which can be attributed to following effects. (1) The properties of GNPs rapidly devolve as sheets aggregate, because aggregated sheets behave like micrometer-size fillers with relatively low surface area. (2) The GNPs agglomerates would form steric obstacles, restricting polymer to flow into the agglomerates and resulting in the formation of holes and voids between GNPs and epoxy [18].

**3.3. Fracture Surface of CNTs/GNPs/Epoxy Nanocomposites.** Figure 9 shows the SEM images of nanocomposites containing fixed weight fraction (1 wt%) with a CNTs/GNPs hybrids mixing ratio of 5:5. Figure 10 is SEM images of nanocomposites with a CNTs/GNPs hybrids mixing ratio of 1:9. Figures 9(a) and 10(a) show that CNTs and GNPs cross-link in crevices among the corrugation area to restrain the creviced growth. Corrugation and CNTs/GNPs hybrids can increase the interfacial friction between carbon fiber and matrix to enhance the mechanical properties. However, when 0.5 wt% (5:5) and 0.1 wt% (1:9) of CNTs are mixing with GNPs and added to epoxy resins, CNTs bridged the GNPs layers as well as resin cracks, as seen in Figures 9(b) and 10(b). Moreover, Figures 9(b) and 10(b) also showed that major cracks in the laminates were restrained by GNPs; CNTs can effectively suppress minor cracks regardless of the CNTs contents which were 0.5 wt% or 0.1 wt%. Figure 11 shows the TEM images of the fracture surfaces of CNTs/GNPs/epoxy

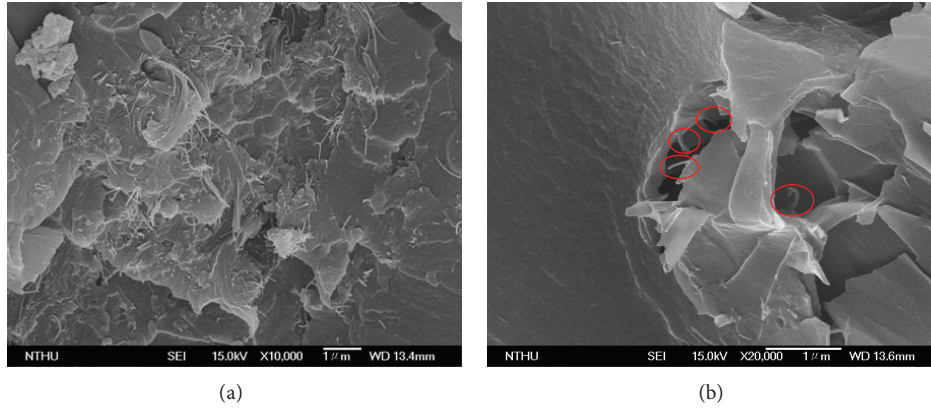


FIGURE 9: SEM images of CNTs/GNPs/epoxy nanocomposite (CNTs/GNPs = 5 : 5). (a)  $\times 10,000$ . (b)  $\times 20,000$ .

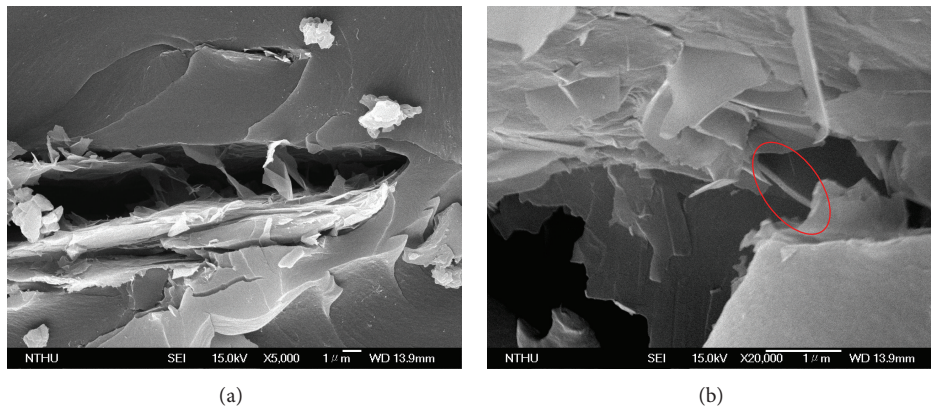


FIGURE 10: SEM images of CNTs/GNPs/epoxy nanocomposite (CNTs/GNPs = 1 : 9). (a)  $\times 5,000$ . (b)  $\times 20,000$ .

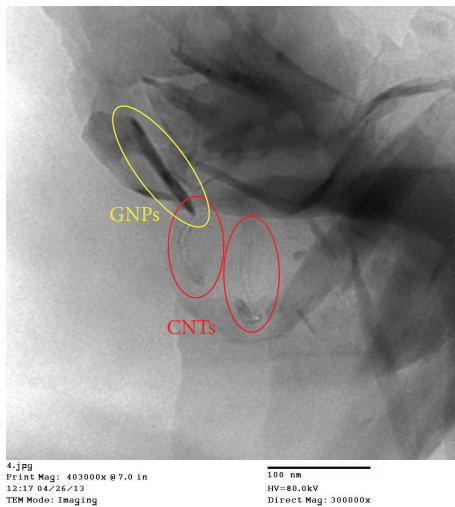


FIGURE 11: TEM image of CNTs/GNPs/epoxy nanocomposite. (CNTs/GNPs = 1 : 9).

resin nanocomposite (CNTs/GNPs = 1 : 9). For nanocomposite containing CNTs/GNPs hybrids, the TEM shows the CNTs entangled around the GNPs.

**3.4. Mechanical Properties of CNTs/GNPs/Epoxy/Carbon Fiber Composite Laminates.** In the previous section, CNTs/GNPs hybrids reinforced epoxy nanocomposite containing the fixed content of CNTs/GNPs hybrids (1 wt%) with different mixing ratio were fabricated and investigate their mechanical properties. The results showed that CNTs/GNPs hybrids mixing ratios of 5 : 5 and 1 : 9 were superior to other ratios. Based on the average of each mechanical property and the reference data obtained from the literature [18], CNTs/GNPs hybrids ratio of 1 : 9 with different added proportions (i.e., 0, 0.5, 1.0, and 1.5 wt%) was used for fabricating CNTs/GNPs/epoxy/carbon fiber composite laminates. Subsequently, static mechanical properties such as flexure, interlaminar shear strength (ILSS), and fracture toughness ( $G_{IC}$ ) were investigated. This provided further understanding regarding the mixtures of 1D and 2D carbon nanomaterials and how their synergetic effects reinforce carbon fiber composite laminates.

Figure 12 and Table 2 show the influence of adding CNTs/GNPs hybrids on the flexural strength of epoxy/carbon fiber composite laminates. The results showed that the flexural strength of carbon fiber composite laminates increased when the amount of CNTs/GNPs hybrids added was increased. When 1 wt% of CNTs/GNPs hybrids was added,

TABLE 2: Mechanical properties of CNTs/GNPs/CFRP composite laminates.

Test item (unit)	CNTs/GNPs hybrids content (wt%) CNTs : GNPs = 1 : 9			
	0	0.5	1.0	1.5
FS (MPa)	580.6	624.8 (+7.6%)	682.1 (+17.5%)	633.8 (+9.2%)
FM (GPa)	31.3	33.4 (+6.8%)	33.7 (+7.7%)	34.4 (+10.0%)
ILSS (MPa)	54.6	76.1 (+39.3%)	76.5 (+40.0%)	72.5 (+32.7%)
$G_{IC}$ (J/m <sup>2</sup> )	468.9	648.7 (+38.3%)	866.8 (+84.9%)	938.0 (+100%)

FS: flexural strength, FM: flexural modulus, and ILSS: interlaminar shearing strength.  $G_{IC}$ : initial fracture toughness  $G_{IC}$ .

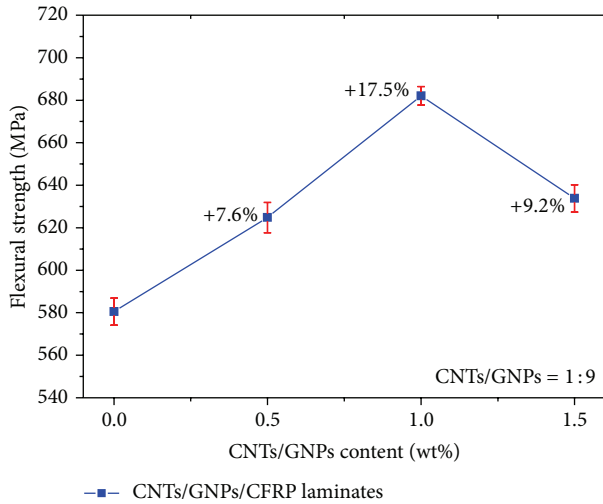


FIGURE 12: Flexural strength of CNTs/GNPs/carbon fiber composite laminates.

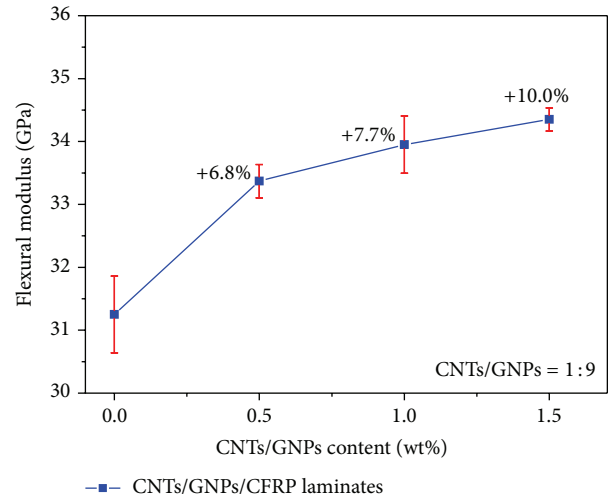


FIGURE 13: Flexural modulus of CNTs/GNPs/carbon fiber composite laminates.

the flexural strength of composite laminates increased up to 17.5%.

Figure 13 and Table 2 show the flexural modulus measured from the flexural test of CNTs/GNPs/epoxy/carbon fiber composite laminates, which is plotted as a function of CNTs/GNPs hybrids content. The modulus grew rapidly with increasing CNTs/GNPs hybrids content. When the hybrids content increased to 1.5 wt%, the highest flexural modulus was reached, and the enhancement was increased by 10%.

Figure 14 and Table 2 present the experimental results of the interlaminar shear strength (ILSS) of the epoxy/carbon fiber composite laminates without and with the three proportions of CNTs/GNPs hybrids contents. The ILSS test have seen implemented in accordance with ASTM D2344. Adding CNTs/GNPs hybrids effectively increased the ILSS of composite laminates. The ILSS of composite laminates were similar when 0.5 and 1.0 wt% of CNTs/GNPs hybrids were added, both increased up to 40%. When 1.5 wt% of CNTs/GNPs hybrids was added to composite laminates, the ILSS were slightly inferior compared to those of the former compositions, but still increased by 32.7%.

Based on the flexure properties of epoxy/carbon fiber composite laminates and results from ILSS, several contributing factors were identified.

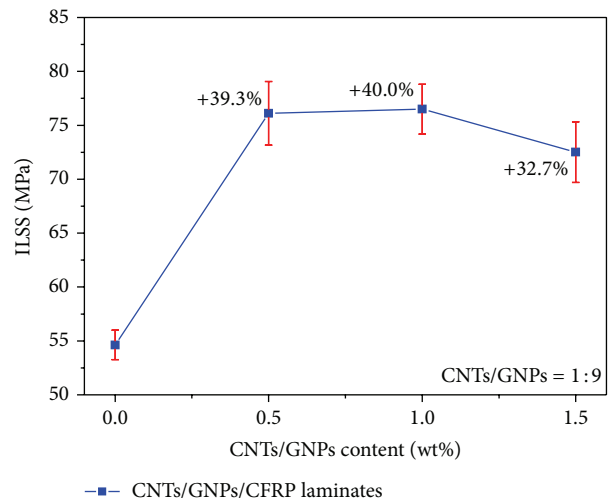


FIGURE 14: Interlaminar shear strength (ILSS) of CNTs/GNPs/carbon fiber composite laminates.

- (1) The first factor was the entanglement and the complementary between CNTs and GNPs. When CNTs were added to the GNPs, they entangled the GNPs and filled gaps between GNPs' interlayer. In addition

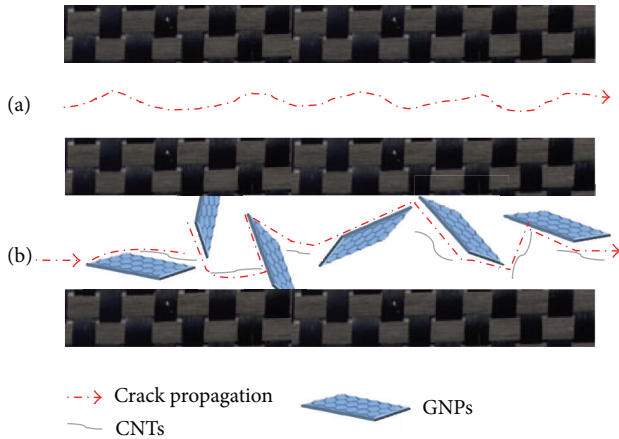


FIGURE 15: Crack propagation on carbon nanomaterials reinforced epoxy/CFRP laminate interface. (a) Neat CFRP laminate; (b) CNTs/GNPs/CFRP composite laminate.

to that CNTs/GNPs hybrids restricting cracks growth in resin, these hybrids could effectively suppress or deter crack propagation. Specifically, when GNPs restrained the development of major cracks, CNTs suppress minor cracks, as shown in Figure 15.

- (2) In general, the addition of inorganic nanoparticles (e.g., GNPs or CNTs), which results in the decrement of mobility of polymer chains, gradually became brittle and increased the modulus of the composite. Thus, the modulus of the polymer composites followed the increase with increasing proportions of carbon nanomaterials added [19, 20].

**3.5. Fracture Toughness of CNTs/GNPs/Epoxy/Carbon Fiber Composite Laminates.** A double cantilever beam was used in this study to investigate Mode I interlaminar fracture toughness of various amounts of CNTs/GNPs hybrids reinforced epoxy/carbon fiber composite laminates.

Figure 16 and Table 2 indicate that the  $G_{IC}$  of composites laminate without added CNTs/GNPs hybrids is approximately  $468.9 \text{ J/m}^2$ . The  $G_{IC}$  of the CNTs/GNPs hybrids added reinforced composite laminate was 100% higher at  $938 \text{ J/m}^2$  than without added CNTs/GNPs hybrids when the carbon nanomaterials content was 1.5 wt%.

A comprehensive knowledge about the influence of nanoparticles on the micromechanics is required in order to explain the observed toughening effect of nanoparticles. The mechanisms of increasing the fracture toughness of polymers via the incorporation of particles have been extensively studied within the last three decades [21–24]. The application of microparticles (spherical or fibrous) exhibits the highest effect in brittle (e.g., thermosetting) matrix systems. Several theories have been developed to explain and understand the effects of particle-toughening and they are often in good agreement with experimental results. The most important micromechanical mechanisms leading to an increase in fracture toughness are (i) localised inelastic matrix deformation and void nucleation, (ii) particle/fibre debonding, (iii) crack

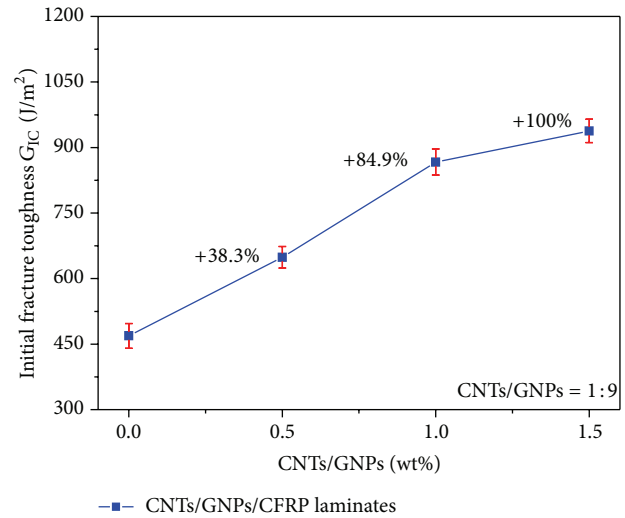


FIGURE 16: Initial fracture toughness ( $G_{IC}$ ) of CNTs/GNPs/CFRP composite laminates.

deflection, (iv) crack pinning, (v) fibre pull-out, (vi) crack tip blunting (or crack tip deformation), and (vii) particle/fibre deformation or breaking at the crack tip. In this study, CNTs/GNPs hybrids mixed to reinforce epoxy/carbon fiber composite laminates and investigate their interlaminar crack suppression properties. Based on the aforementioned literature and experimental results, the crack growth suppression behavior in composite laminate was primarily caused by the crack deflection of GNPs. When cracks begin to grow, the cracks in the interlaminations of composite laminate deflect due to the interactions of GNPs, consequently suppressing crack growth effectively. In addition, regarding size effect, GNPs primarily suppress the growth of major cracks and CNTs resist the propagation of smaller cracks. Thus, under the synergetic effect of CNTs and GNPs, the interlaminar energy of the fiber composite laminate can be suitably reinforced. This is the reason that the reinforcement effect of Mode I fracture toughness became increasingly noticeable as the carbon nanomaterial content increased.

## 4. Conclusion

The experimental results showed that the mechanical properties of CNTs/GNPs/epoxy nanocomposites and CNTs/GNPs/epoxy/carbon fiber composite laminates have optimal characteristics with reinforcement through CNTs/GNPs hybrids addition; furthermore, the ultimate tensile strength, flexure properties, and interlaminar shear strength (ILSS) were all improved. Based on the experimental results, adding the present CNTs/GNPs hybrids to the epoxy resin and epoxy/carbon fiber composite laminates provides a considerable synergetic effect. Therefore, when CNTs were added to the GNPs, they entangled the GNPs and filled gaps between GNPs' interlayer. In addition to that CNTs/GNPs hybrids restricting cracks growth in resin, these hybrids could effectively suppress or deter crack propagation in the composite laminates.

## Conflict of Interests

The authors declare that they have no conflict of interests.

## Acknowledgment

This research was supported by the Ministry of Science and Technology of Taiwan (National Science Council of Taiwan), under Grant no. MOST 103-2221-E-253-009.

## References

- [1] M. Moniruzzaman and K. I. Winey, "Polymer nanocomposites containing carbon nanotubes," *Macromolecules*, vol. 39, no. 16, pp. 5194–5205, 2006.
- [2] Y. Li, T. Yu, T. Pui, P. Chen, L. Zheng, and K. Liao, "Fabrication of transparent and conductive carbon nanotube/polyvinyl butyral films by a facile solution surface dip coating method," *Nanoscale*, vol. 3, no. 6, pp. 2469–2471, 2011.
- [3] T. Yu, Y. Gong, T. Lu et al., "Recognition of carbon nanotube chirality by phage display," *RSC Advances*, vol. 2, no. 4, pp. 1466–1476, 2012.
- [4] Y. Li, T. Yu, T. Pui, P. Chen, L. Zheng, and K. Liao, "Fabrication and characterization of recyclable carbon nanotube/polyvinyl butyral composite fiber," *Composites Science and Technology*, vol. 71, no. 14, pp. 1665–1670, 2011.
- [5] Y. Li, R. Umer, A. Isakovic, Y. A. Samad, L. Zheng, and K. Liao, "Synergistic toughening of epoxy with carbon nanotubes and graphene oxide for improved long-term performance," *RSC Advances*, vol. 3, no. 23, pp. 8849–8856, 2013.
- [6] A. Yu, P. Ramesh, M. E. Itkis, E. Bekyarova, and R. C. Haddon, "Graphite nanoplatelet-epoxy composite thermal interface materials," *Journal of Physical Chemistry C*, vol. 111, no. 21, pp. 7565–7569, 2007.
- [7] C. Lin and D. D. L. Chung, "Graphite nanoplatelet pastes vs. carbon black pastes as thermal interface materials," *Carbon*, vol. 47, no. 1, pp. 295–305, 2009.
- [8] M.-T. Hung, O. Choi, Y. S. Ju, and H. T. Hahn, "Heat conduction in graphite-nanoplatelet-reinforced polymer nanocomposites," *Applied Physics Letters*, vol. 89, no. 2, Article ID 023117, 2006.
- [9] Y. Si and E. T. Samulski, "Exfoliated graphene separated by platinum nanoparticles," *Chemistry of Materials*, vol. 20, no. 21, pp. 6792–6797, 2008.
- [10] Y. Si and E. T. Samulski, "Synthesis of water soluble graphene," *Nano Letters*, vol. 8, no. 6, pp. 1679–1682, 2008.
- [11] D. Li, M. B. Müller, S. Gilje, R. B. Kaner, and G. G. Wallace, "Processable aqueous dispersions of graphene nanosheets," *Nature Nanotechnology*, vol. 3, no. 2, pp. 101–105, 2008.
- [12] M. A. Rafiee, J. Rafiee, Z. Wang, H. Song, Z.-Z. Yu, and N. Koratkar, "Enhanced mechanical properties of nanocomposites at low graphene content," *ACS Nano*, vol. 3, no. 12, pp. 3884–3890, 2009.
- [13] J. Li, M. L. Sham, J.-K. Kim, and G. Marom, "Morphology and properties of UV/ozone treated graphite nanoplatelet/epoxy nanocomposites," *Composites Science and Technology*, vol. 67, no. 2, pp. 296–305, 2007.
- [14] M.-Y. Shen, T.-Y. Chang, T.-H. Hsieh et al., "Mechanical properties and tensile fatigue of graphene nanoplatelets reinforced polymer nanocomposites," *Journal of Nanomaterials*, vol. 2013, Article ID 565401, 9 pages, 2013.
- [15] T. Yokozeki, Y. Iwahori, S. Ishiwata, and K. Enomoto, "Mechanical properties of CFRP laminates manufactured from unidirectional prepregs using CSCNT-dispersed epoxy," *Composites Part A: Applied Science and Manufacturing*, vol. 38, no. 10, pp. 2121–2130, 2007.
- [16] B. C. Ray, "Temperature effect during humid ageing on interfaces of glass and carbon fibers reinforced epoxy composites," *Journal of Colloid and Interface Science*, vol. 298, no. 1, pp. 111–117, 2006.
- [17] G. E. Morris, "Determining fracture directions and fracture origins on failed graphite/epoxy surfaces," in *Nondestructive Evaluation and Flaw Criticality for Composite Materials*, R. B. Pipes, Ed., ASTM STP 696, pp. 274–297, ASTM International, 1979.
- [18] S.-Y. Yang, W.-N. Lin, Y.-L. Huang et al., "Synergetic effects of graphene platelets and carbon nanotubes on the mechanical and thermal properties of epoxy composites," *Carbon*, vol. 49, no. 3, pp. 793–803, 2011.
- [19] V. K. Rangari, T. A. Hassan, Q. Mayo, and S. Jeelani, "Size reduction of WO<sub>3</sub> nanoparticles by ultrasound irradiation and its applications in structural nanocomposites," *Composites Science and Technology*, vol. 69, no. 14, pp. 2293–2300, 2009.
- [20] R. M. Rodgers, H. Mahfuz, V. K. Rangari, N. Chisholm, and S. Jeelani, "Infusion of SiC nanoparticles into SC-15 epoxy: an investigation of thermal and mechanical response," *Macromolecular Materials and Engineering*, vol. 290, no. 5, pp. 423–429, 2005.
- [21] A. C. Moloney, H. H. Kausch, T. Kaiser, and H. R. Beer, "Parameters determining the strength and toughness of particulate filled epoxide resins," *Journal of Materials Science*, vol. 22, no. 2, pp. 381–393, 1987.
- [22] S. Bandyopadhyay, "Review of the microscopic and macroscopic aspects of fracture of unmodified and modified epoxy resins," *Materials Science and Engineering A*, vol. 125, no. 2, pp. 157–184, 1990.
- [23] D. A. Norman and R. E. Robertson, "Rigid-particle toughening of glassy polymers," *Polymer*, vol. 44, no. 8, pp. 2351–2362, 2003.
- [24] B. Fiedler, F. H. Gojny, M. H. G. Wichmann, M. C. M. Nolte, and K. Schulte, "Fundamental aspects of nano-reinforced composites," *Composites Science and Technology*, vol. 66, no. 16, pp. 3115–3125, 2006.

## Research Article

# Magnetic and Electrical Properties of Nitrogen-Doped Multiwall Carbon Nanotubes Fabricated by a Modified Chemical Vapor Deposition Method

María Luisa García-Betancourt,<sup>1</sup> Yadira Itzel Vega-Cantu,<sup>2</sup> Sofía Magdalena Vega-Díaz,<sup>3</sup> Aarón Morelos-Gómez,<sup>4</sup> Mauricio Terrones,<sup>4,5,6</sup> and Emilio Muñoz-Sandoval<sup>1</sup>

<sup>1</sup>Advanced Materials Division, IPICYT, Camino a la Presa, San Jose 2055, 78216 San Luis Potosí, SLP, Mexico

<sup>2</sup>Department of Chemistry, Federal University of Pernambuco, Cidade Universitária, 50670-901 Recife, PE, Brazil

<sup>3</sup>CONACYT-Lectures, Technological Institute of Celaya, Avenida Tecnológico Esquina con Garcia Cubas S/N, 38010 Celaya, GTO, Mexico

<sup>4</sup>Institute for Carbon Science and Technology, Shinshu University, 4-17-1 Wakasato, Nagano City 380-8553, Japan

<sup>5</sup>Department of Physics and Center for 2-Dimensional and Layered Materials, The Pennsylvania State University, University Park, PA 16802-6300, USA

<sup>6</sup>Department of Chemistry, Department of Materials Science and Engineering & Materials Research Institute, The Pennsylvania State University, University Park, PA 16802-6300, USA

Correspondence should be addressed to Emilio Muñoz-Sandoval; [ems@ipicyt.edu.mx](mailto:ems@ipicyt.edu.mx)

Received 27 September 2014; Revised 13 January 2015; Accepted 19 January 2015

Academic Editor: Myoung-Woon Moon

Copyright © 2015 María Luisa García-Betancourt et al. This is an open access article distributed under the Creative Commons Attribution License, which permits unrestricted use, distribution, and reproduction in any medium, provided the original work is properly cited.

Chemical vapor deposition (CVD) is a preferential method to fabricate carbon nanotubes (CNTs). Several changes have been proposed to obtain improved CNTs. In this work we have fabricated nitrogen-doped multiwall carbon nanotubes (N-MWCNTs) by means of a CVD which has been slightly modified. Such modification consists in changing the content of the by-product trap. Instead of acetone, we have half-filled the trap with an aqueous solution of NaCl (0–26.82 wt.%). Scanning electron microscope (SEM) characterization showed morphological changes depending upon concentration of NaCl included in the trap. Using high resolution transmission electron microscopy several shape changes on the catalyst nanoparticles were also observed. According to Raman spectroscopy results N-MWCNTs fabricated using pure distillate water exhibit better crystallinity. Resistivity measurements performed on different samples by physical properties measurement Evercool system (PPMS) showed metallic to semiconducting temperature dependent transitions when high content of NaCl is used. Results of magnetic properties show a ferromagnetic response to static magnetic fields and the coercive fields were very similar for all the studied cases. However, saturation magnetization is decreased if aqueous solution of NaCl is used in the trap.

## 1. Introduction

After the discovery, structural identification, and bulk production of carbon nanotubes (CNTs) the interest of researchers about these nanostructures increased exponentially, and the big quest for novel applications started [1–4]. Enormous and exhaustive work, carried out by several important groups, have exhibited their unique thermal, magnetic, mechanical, chemical, and electronic properties [5–7], thus leading to the design of new devices for biosensing,

nanoprobng, spintronics, field emission, and other important applications [8–11].

One of the most important challenges in nanotube science nowadays is the control of the morphology because this is the route to control the physicochemical properties [10–12]. Depending on the desired applications, modifications in the chemical vapor deposition (CVD) method offer an optional approach to induce some important properties to carbon nanostructures, such as the introduction of water vapor together with the inert gas flow to grow very large carbon

nanotubes [13, 14], or the modulation of the shape, size, and crystallinity of catalytic metallic nanoparticles determining the chiral-selective growth of CNTs [15]. In the case of the introduction of contaminants, some authors used alkali chlorides in order to deform the straight carbon nanofibers into helical structure or belts [16, 17]; Lv and coworkers employed Cl as a cleaner of nanoparticles when introduced into the CVD, which evaporates during the process [18, 19]. In other cases it is desirable to have defects in carbon nanotubes such as nonhexagonal rings, dangling bonds, doping, non- $sp^2$ , and folding because they are the origin of producing many forms and new carbon architectures [12–21] by adjusting some parameters in the chemical vapor deposition (CVD) method. For example, the introduction of sulfur in the atomizer solution allowed the synthesis of random 3D structures [22]. A two-step CVD was used for the production of three-dimensional networks [23] and long tipped CNTs [24]. Pressure and temperature fluctuations can produce branched junctions [25, 26]. Currently, the versatility of CVD has been exploited widely, allowing modifications in their involved parameters in order to produce highly defective N-MWCNTs. Notwithstanding, research about this method continues increasing because the mechanism of growth of CNT remains unclear.

In the present work, following previous research [27, 28] we are proposing a simple modification of the CVD synthesis to alter the morphology and properties of N-MWCNTs, also known as  $CN_x$ ; the modification consists in changing the solution of the by-product trap in the synthesis. We used deionized water and aqueous solutions of NaCl at different weight concentrations, low (1 wt.%), half-saturated (15.84 wt.%), and saturated (26.92 wt.%); instead of acetone which has been normally employed, we used water and aqueous solutions of NaCl at different weight concentrations. We also proposed the growth mechanism of these nanostructures.

## 2. Materials and Methods

Forests of nitrogen-doped carbon nanotubes (N-MWCNTs) were produced by a slightly modified CVD method using the one-furnace configuration with a by-product trap at the outlet of the quartz tube. The pyrolyzed solution containing 94% of benzylamine ( $C_7H_9N$ , Sigma Aldrich), as a source of carbon and nitrogen, and 6% ferrocene ( $FeCp_2$ , Sigma Aldrich) for the catalytic nanoparticles was prepared and placed in a reservoir plugged in to a pulse generator. The reaction was performed during 30 min and using a one-furnace system as is shown in Figure 1. The mixture solution of ferrocene and benzylamine was placed into the atomizer reservoir (see Figure 1). In order to obtain enough material to be characterized a small piece of  $SiO_2/Si$  was placed inside the quartz tube at the middle of the furnace. In this zone, the temperature is stable ( $850^\circ C \pm 3^\circ C$ ). In a first experiment 200 mL of acetone was put inside the trap. We present some images of such CNT in Supplementary Information (see Figure S1 in Supplementary Material available online at <http://dx.doi.org/10.1155/2015/587416>). In a second experiment, we half-filled the trap with deionized water (Fermont)

instead of acetone. For the following experiments, the density of deionized water was increased by adding NaCl at different weight concentrations (1 wt.%, 15.84 wt.%, and 26.92 wt.%). The obtained samples were called in agreement with the density of the liquid in the trap as  $CN_{x-1}$  for acetone (density  $0.79 \text{ g/cm}^3$ ),  $CN_{x-2}$  for deionized water (density  $1.00 \text{ g/cm}^3$ ),  $CN_{x-3}$ ,  $CN_{x-4}$ , and  $CN_{x-5}$  for the cases of aqueous solutions of NaCl and densities of  $1.01 \text{ g/cm}^3$ ,  $1.21 \text{ g/cm}^3$ , and  $1.56 \text{ g/cm}^3$ , respectively. In all cases the total mixture poured in the trap was 200 mL, which is equivalent to a half-filled trap. For the purpose of having an inert atmosphere inside of the quartz tube (see Figure 1), a constant argon flow rate of 2.5 L/min was established. In all experiments, the temperature was  $850^\circ C$  inside of the furnace where the substrates were situated. The solution mixture was atomized from the solution container by an ultrasonic generator during 30 min. In each case, the substrate was taken out for characterization using scanning electron microscopy (SEM-FEI XL 30 SFEG). In order to prepare the samples for high resolution transmission electron microscopy (HRTEM-FEI TECNAI F30) a small quantity was scraped from the substrates and incorporated into a vial with ethanol, ultrasonicated for 5 minutes and drop-cast on the grids. In the case of X-ray diffraction (RX Advance) characterization the whole substrate was used; the settings follow:  $2\theta$  from  $10^\circ$  to  $90^\circ$  and step size of 0.04 during 5 seconds. Raman characterization was performed using a laser of 514 nm in a Raman Renishaw Micro-Raman equipment. Thermogravimetric analysis was achieved using a TGA-Thermo Cahn, model Versa Therm apparatus. The magnetic and resistivity measurements were carried out in a physical properties measurement system (PPMS, Quantum Design). In order to verify the substance effect in the morphology and physical properties of N-MWCNTs we carried out additional experiments as following: (i) the trap was filled with 300 mL of mixture solution of benzylamine and ferrocene (2.5% wt.%); (ii) there was not any substance in the atomizer reservoir; (iii) several clean substrates were placed inside of quartz tube; (iv) the experimental setup was run normally. The resultant sample (substrate and CNT) from this experiment were characterized by SEM (Figure S4 of Supplementary Information) and analyzed in an optical emission spectrophotometer (OES) in order to measure ppm of Na or Cl.

## 3. Results

Figure 2 exhibits SEM images of N-MWCNTs obtained from the different synthesis conditions described above. Figure 2(a) is SEM images of N-MWCNTs fabricated using acetone in the trap ( $CN_{x-1}$  sample); such CNTs are vertically aligned and in general they present bamboo morphology [29, 30] with diameters around 50 nm; sometimes it is possible to observe CNTs with smaller diameters enrolled to the thicker CNTs. In the case when the trap is half-filled with distilled water ( $CN_{x-2}$  sample), the fabricated CNTs have larger diameters and present morphologies which are showed in Figure 2(b); some collapsed structures can be present (see inset). If an aqueous solution of NaCl is used in the trap an additional phenomena could be observed ( $CN_{x-3}$  sample). In this case, sharp morphologies of N-MWCNTs were observed.

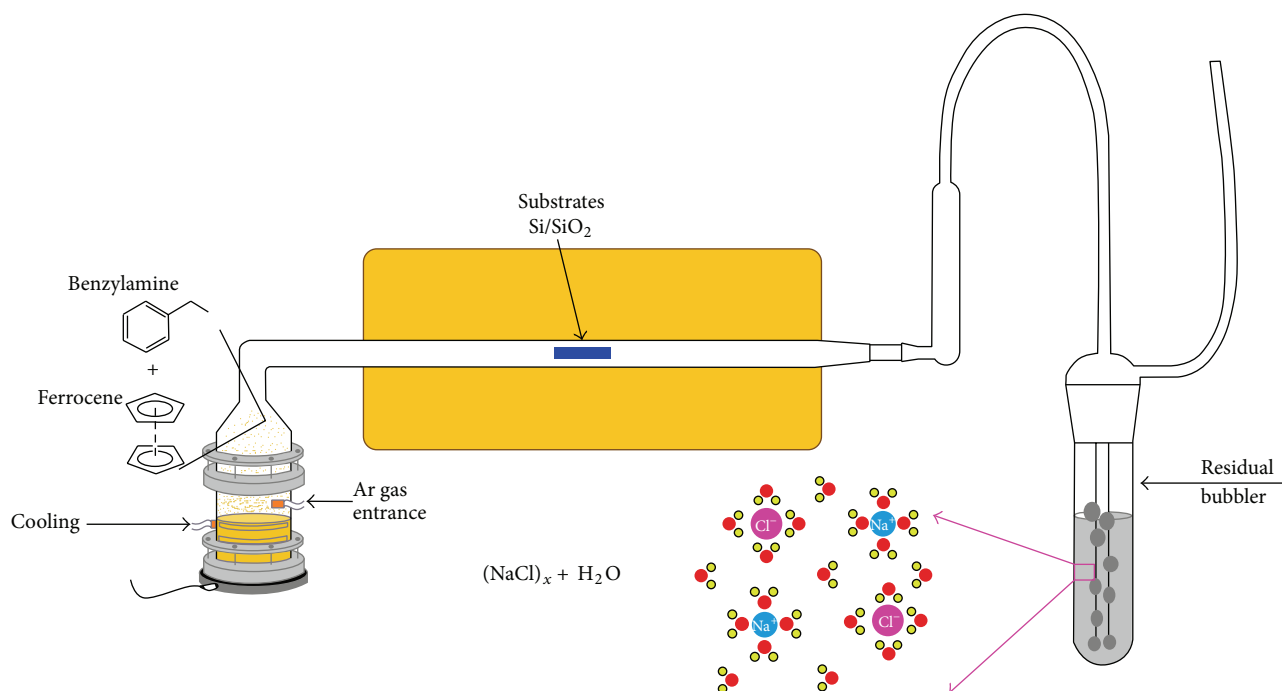


FIGURE 1: Typical CVD setup for carbon nanotubes synthesis using one furnace. Each component used for producing our samples is indicated in the figure. The size of the trap is only representative. The level used in the trap is an important parameter for all our experiments because they are determining the structure and physical properties of resultant N-MWCNTs nanotubes. The substrate is 10 cm long and was placed inside the quartz tube at the middle of the furnace (20 cm).

It seems that such morphologies are formed because the end compartments of the bamboo structure are damaged. Apparently, small nanoparticles play an important role to form sharp CNTs. Another well detectable defect mostly observed in the  $CN_{x-4}$  samples is nanoparticles attached to the external walls of N-MWCNTs known as “nanolumps” [31, 32]. Such nanoparticles may abundantly appear forming “lumpy” nanostructures as is shown in Figure 2(d); Li and coworkers obtained lumpy CNT as a result of air-assisted synthesis [33]. It is probable that these lumps could catalyze thin N-MWCNTs forming the branch morphology [34]. More complex defects were detected in the sample  $CN_{x-5}$ . Coalescence of N-MWCNTs and ruptures of thick CNTs with arms or branches were observed (Figure 2(e)). As can be seen at this figure very thin N-MWCNTs with few layers are emerging from such coalesced nanotubes. In Figure 2(f) the catalytic nanoparticles responsible for the growth of  $CN_{x-5}$  are shown. Notice the sharp nail structure as claws. This situation can be one of the main effects of putting saturated NaCl aqueous solution inside the trap.

Figure 3 displays representative TEM images of the different fabricated N-MWCNTs. Figure 3(a) contains a micrograph of the case  $CN_{x-2}$  (water), showing N-MWCNTs with diameters as small as 2 nm and as big as 60 nm. Most of N-MWCNTs exhibited bamboo-type morphology, some of them with conical and other with cylindrical compartments. It is difficult to say how nitrogen is incorporated into the N-MWCNTs without X-ray photoelectron spectroscopy (XPS) analysis of the samples. However, there are some studies showing that the shape of compartments can be associated

with the type of nitrogen inclusion in the graphitic structure of CNT [35]. Both shapes of compartments are also observed in N-MWCNTs fabricated when acetone is used in the trap (see Figure S1, Supplementary Information). Figure 3(b) also exhibits representative TEM images of N-MWCNTs corresponding to the  $CN_{x-2}$  (water). Here, it is possible to observe a thin CNT with two collapsed sites and a CNT with lumps of different sizes (Figure 3(b)). In the case of aqueous solution with NaCl 1 wt.% (distilled water slightly altered with NaCl) another morphology of N-MWCNTs is observed, namely, broken CNTs with a sharp end where an encapsulated conical-shape nanoparticle is observed (Figure 3(c)); for the case  $CN_{x-4}$  using aqueous solution of NaCl 15.84 wt.% (water with NaCl at half-saturation) the sample shows a lump attached to CNT (Figure 3(d)). The sample  $CN_{x-5}$ , when the trap was filled with aqueous solution of NaCl at 26.92 wt.% (saturated water of NaCl), exhibited complex morphologies as displayed in Figures 3(e) and 3(f). Apparently coaxial CNTs with large diameters and ruptures are formed in this case (Figure 3(e)). These CNTs can be coalesced with others to form the structure presented in the right part of Figure 3(e). In addition, it is probable to find multiterminal junctions containing different shapes and sized metallic nanoparticles (Figure 3(f)).

The diameter distribution corresponding to the different obtained N-MWCNTs samples is presented in Figure S5. The diameter distribution has a Gaussian-type shape in the case of  $CN_{x-1}$ , which is the sample produced using a trap with acetone. In the case of  $CN_{x-2}$  and  $CN_{x-3}$  the respective diameter distribution curves exhibit bimodal behaviors. In

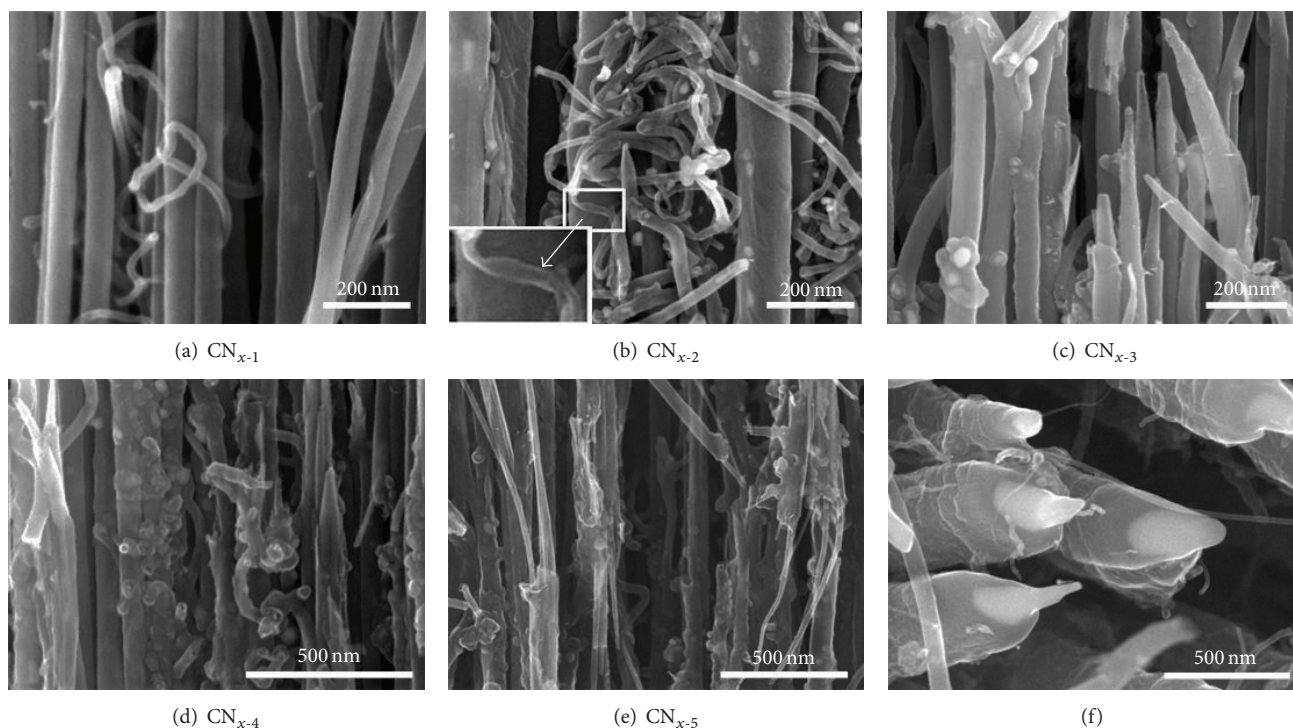


FIGURE 2: SEM images of the aligned N-MWCNTs grew over Si/SiO<sub>2</sub> substrates displaying the different morphologies observed in our samples: (a) typical morphology of N-MWCNTs produced with acetone in the trap (CN<sub>x-1</sub>); (b) N-MWCNTs fabricated using deionized water in the trap (CN<sub>x-2</sub>); (c) image showing tip morphology of N-MWCNTs formed when an aqueous solution of NaCl is used (1.0 wt.% case; CN<sub>x-3</sub>); (d) image of N-MWCNTs in the case of CN<sub>x-4</sub> case: here lumps are the main defects detected; (e) image of CN<sub>x-5</sub> case (aqueous solution of NaCl 26.92 wt.%): complex structures are observed with very thin CNTs; (f) root part of CN<sub>x-5</sub>: N-MWCNTs also fabricated with aqueous solution of NaCl 26.92 wt.%, showing dramatic changes in the catalytic nanoparticles. More related SEM figures can be seen in SI (Figure S4).

the cases of CN<sub>x-4</sub> and CN<sub>x-5</sub> the diameter distributions are also bimodal however with lower pronounced differences. The average diameters for the different cases were  $62 \pm 2$  nm,  $47 \pm 3$  nm,  $61 \pm 2$  nm,  $36 \pm 2$  nm, and  $37 \pm 2$  nm for CN<sub>x-1</sub>, CN<sub>x-2</sub>, CN<sub>x-3</sub>, CN<sub>x-4</sub>, and CN<sub>x-5</sub>, respectively.

It is probable that the different CNT morphologies found in our samples could be attributed to the catalytic metallic nanoparticles. The final shape of these nanoparticles could give us information about the process involved in the growth of different N-MWCNTs observed. Figure 4 depicts TEM images of some encapsulated metallic nanoparticles found in distinct N-MWCNTs samples. Long nanowires with more than 500 nm length (Figure 4(a)) were observed in the samples CN<sub>x-2</sub> and CN<sub>x-3</sub> (low content of NaCl in the trap). Encapsulated nanoparticles with irregular morphologies distort the CNT structure (Figure 4(b)) or can form junctions (Figure 4(c)). These types of nanoparticles were observed in CN<sub>x-4</sub> which were produced with a moderate quantity of aqueous solution NaCl in the trap. Very small encapsulated nanoparticles along the CNTs (internal multiparticles) were detected in N-MWCNTs fabricated with a saturated aqueous solution NaCl in the trap (Figure 4(d)). Also lumps encapsulating nanoparticles with oval morphology or nanoparticles incrustrated in the wall could be found in this saturated case (Figures 4(e) and 4(f)). It seems that the inclusion of NaCl in

the trap with water produces effects among the nanoparticles. However, it is not possible to be sure about that, unless more sophisticated experiments are performed to elucidate the real growth mechanism.

Figure 5 shows the X-ray diffractograms for all the samples obtained from the diverse situations. CN<sub>x-1</sub> presents the two typical predominant phases characteristic of N-MWCNTs fabricated with acetone in the trap, namely, C and Fe<sub>3</sub>C; possibly  $\alpha$ -Fe phase is also present. Probably the most intense peak of (110) of  $\alpha$ -Fe around 45° is spliced with the plane (103) of Fe<sub>3</sub>C. The inclusion of distilled water inside of the trap (CN<sub>x-2</sub>) changes the diffraction patterns and some peaks of Fe<sub>3</sub>C were relatively increased such as (112), (021), (200), and (120) planes for  $2\theta$ : 37.73°, 38.03°, 40.09°, and 41.28°, respectively; the peaks for the planes (140) and (313) at 78.27° and 78.78° present a relative higher intensity as well. Note that the Fe<sub>3</sub>O<sub>4</sub> is clearly present in this case. For CN<sub>x-3</sub>, which is the case when the aqueous solution contains 1.0 wt.%, the appearance of iron oxides (maghemite  $\gamma$ -Fe<sub>2</sub>O<sub>3</sub> and magnetite Fe<sub>3</sub>O<sub>4</sub>) in the samples is clearly seen in Figure 5 (green plot). However, if the percentage of NaCl is increased in the aqueous solution used in the trap, the intensities of peaks corresponding to iron oxides phase are reduced or in some cases they disappear. This situation could be due to the Na<sup>+</sup> and Cl<sup>-</sup> ions saturated in the water molecules, limiting

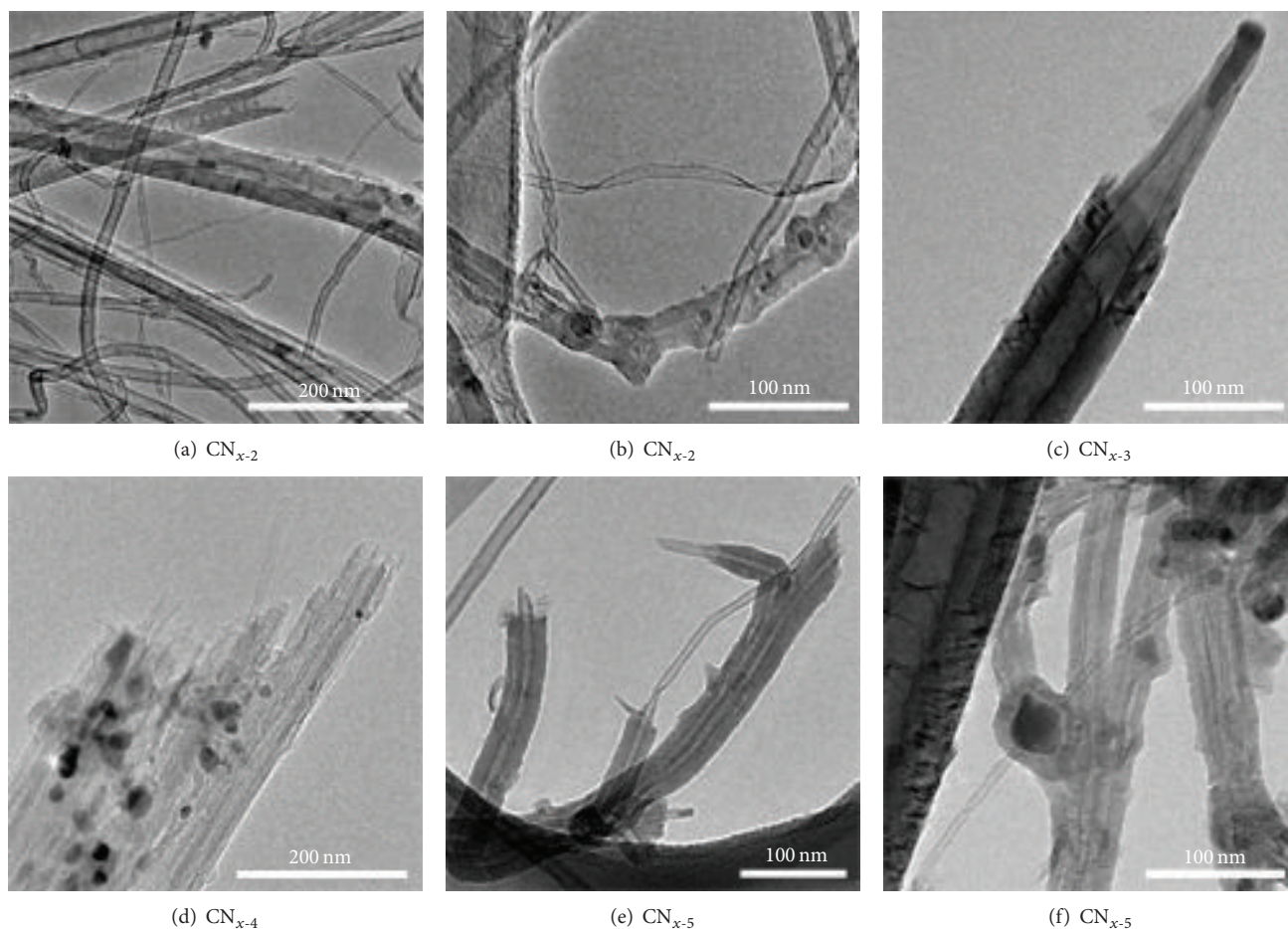


FIGURE 3: TEM images displaying the representative morphologies of fabricated N-MWCNTs over Si/SiO<sub>2</sub> substrates using different aqueous solutions of NaCl in the trap, namely, (a) and (b) CN<sub>*x-2*</sub>; (c) CN<sub>*x-3*</sub>; (d) CN<sub>*x-4*</sub>; and (e) and (f) CN<sub>*x-5*</sub>.

the oxygen reflux entrance to the system. This could be the reason why the X-ray diffractogram of CN<sub>*x-1*</sub> is very similar to the respective CN<sub>*x-5*</sub>.

In order to analyze the thermal stability and reactivity of our N-MWCNTs we have carried out thermogravimetric analysis (TGA) under oxygen atmosphere. The samples were analyzed using a rate heating of 10 C/min. Figure 6 shows the degradation curve for each sample, plotted as loss mass (%) versus temperature. All curves are similar with some differences related to the samples, such as the degradation temperature, obtained from the maximum value of the first loss mass derivative (see inferior inset at the left), calculated from the degradation plots. The maximum values of first loss mass derivative are plotted for each sample at the top inset at the right. As can be seen, the plot has in general a decreasing behavior as the weight percent of NaCl was increased, showing a maximum value of 458°C for CN<sub>*x-2*</sub> (only water in the trap), revealing that this sample is the least reactive compared to the other cases. It seems that water in the trap produces CNTs more resistant to oxidation with fewer defects or nitrogen atoms in the walls. Possibly this result could be correlated with the fact that the compartments of CN<sub>*x-2*</sub> are longer than the other cases (see Figure 4(b)). The decrease of degradation

temperature in the samples CN<sub>*x-3*</sub>, CN<sub>*x-4*</sub>, and CN<sub>*x-5*</sub> could be attributed to the introduction of additional defects to the graphitic surface of CNTs. The mass loss at lower temperatures could be imputed by the quantity of amorphous carbon in the sample. We observed that CN<sub>*x-2*</sub> contains the higher percentage of amorphous carbon (~1.24%), higher than CN<sub>*x-1*</sub> (~1.04%) and CN<sub>*x-3*</sub>, CN<sub>*x-4*</sub>, and CN<sub>*x-5*</sub> (0.62%, no observable%, 0.85%, resp.). The residual mass observed at the final degradation temperature corresponds to the iron oxide; the content was also different for each sample. CN<sub>*x-1*</sub> exhibits the lowest residual mass (7.41%), while for CN<sub>*x-2*</sub> and CN<sub>*x-3*</sub> the percentage is very similar (7.94% and 8.08%, resp.) and for CN<sub>*x-4*</sub> and CN<sub>*x-5*</sub> the percentage of residual was increasing (8.44% and 8.72%, resp.). The reason for this increase can be associated with the agglomeration of metallic nanoparticles in the later cases, as was observed with the presence of nanolumps which are bigger for these cases.

For the purpose of studying the microstructure and crystalline order of our carbon nanotubes we performed Raman spectroscopy measurements. We used excitation energy of 514 nm over the samples of N-MWCNTs synthesized with the different liquids in the residual bubbler. The Raman spectra are presented in Figure 7(a), plotted between 100 and

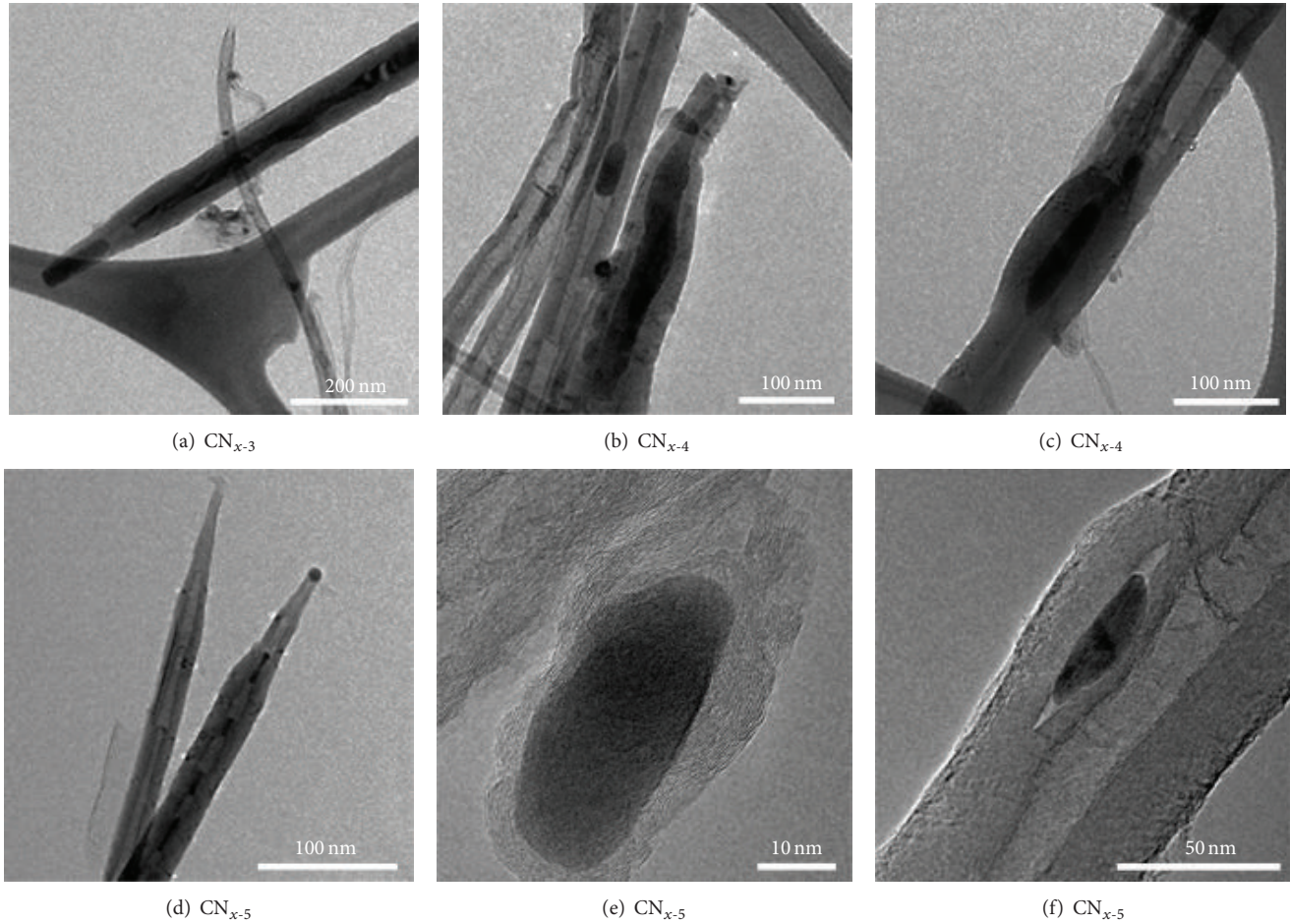


FIGURE 4: (a) Sharp N-MWCNTs encapsulating a nanowire longer than 500 nm followed by a cylinder nanoparticle at the tip of the CNT; (b) N-MWCNTs with irregular-shaped metallic nanoparticles; (c) oval-shaped nanoparticle followed by two N-MWCNTs forming a junction; (d) two N-MWCNTs with sharp morphology: one of them has multiple encapsulated metallic nanoparticles; (e) oval lump that shows the graphitic carbon shells formed in the compartments; (f) “oval” nanoparticle encapsulated laterally in the walls of the bamboo structure of N-MWCNTs.

$3500\text{ cm}^{-1}$ . The typical characteristic bands of carbonaceous materials are indicated in the plot, the D band situated at  $1352\text{ cm}^{-1}$  (defect mode), G band situated at  $1580\text{ cm}^{-1}$  (graphite mode), and  $G'$  located near  $2500\text{--}2800\text{ cm}^{-1}$  (second order mode). The peaks appeared in the range  $200\text{--}500\text{ nm}$  in two of the spectra ( $\text{CN}_{x-2}$  and  $\text{CN}_{x-3}$ , marked with asterisks) which very probably correspond to the presence of iron oxides compounds [36–38], as X-ray diffraction analysis results have shown in such samples. The D band, G band, and  $G'$  shifts are within the intervals of  $1353\text{ cm}^{-1}$  to  $1359\text{ cm}^{-1}$ ,  $1587\text{ cm}^{-1}$  to  $1590\text{ cm}^{-1}$ , and  $1795\text{ cm}^{-1}$  to  $1712\text{ cm}^{-1}$ , respectively. We can observe a small shifting towards lower frequencies for the samples synthesized using deionized water or aqueous solution with NaCl with respect to the as-produced with acetone in the residual bubbler, but specifically the G shifting to lower frequencies indicates a reduction of N doping for  $\text{CN}_{x-2}$  (produced with water). This situation is concomitant with the observation in TGA, where a less reactive sample was observed. We studied the sample from the rates in intensities  $I_D/I_G$  and  $I_{G'}/I_G$ ; such values are plotted

in Figures 7(b) and 7(c) as a function of the sample. In each sample, the D band intensity is lower than G band intensity. At the same time  $G'$  band intensity increases as the weight concentration of NaCl increases. The sample with high degree of disorder or with nongraphitic carbon is the  $\text{CN}_{x-2}$  (matches with TGA analysis), followed by  $\text{CN}_{x-3}$  whose values are 0.83 and 0.75, respectively. The most crystalline sample resulted in the  $\text{CN}_{x-4}$  with a rate  $I_D/I_G$  value of 0.38. The rate  $I_{G'}/I_G$  increases with the increment of density in the liquid, probably indicating that we have quite crystalline samples when substances other than acetone are used in the trap. The  $G'$  band is a particular mark of carbonaceous materials; it is higher in pure materials, such as nondoped CNT and graphene.

Figures 8(a)–8(f) exhibit the hysteresis loops measured in the interval  $\pm 1\text{ T}$  for 2 K, 100 K, and 300 K for the N-MWCNTs samples synthesized with different substances in the trap. For each plot, we have included the corresponding SEM images of N-MWCNTs forest grown on  $\text{Si}/\text{SiO}_2$  (Figures 8(f)–8(j)). In addition, we have drawn the encapsulated nanoparticles observed by TEM to each case. In each

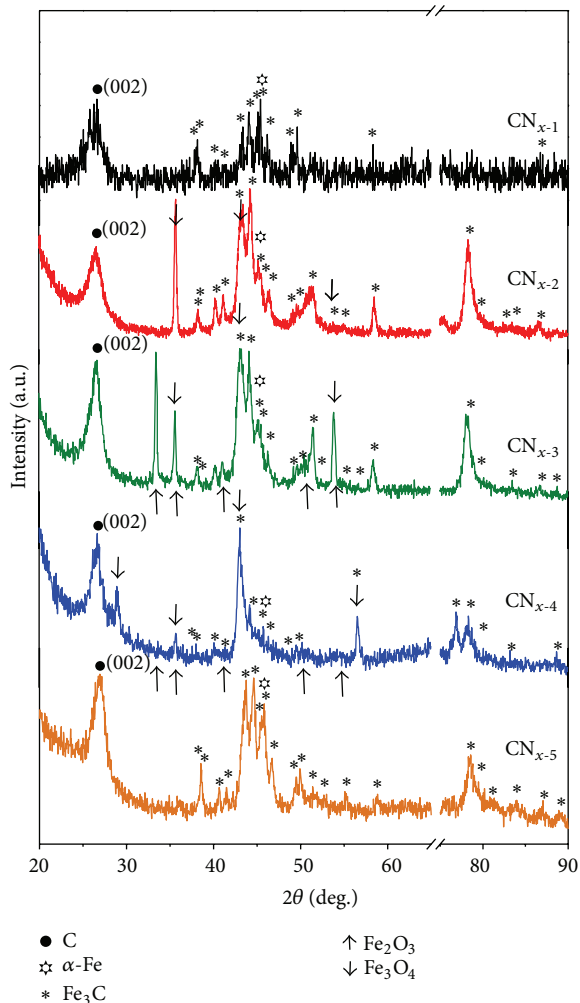


FIGURE 5: X-ray diffractograms for the N-MWCNTs samples synthesized with different liquids in the residual bubbler (trap):  $CN_{x-1}$  (acetone),  $CN_{x-2}$  (water),  $CN_{x-3}$  (low 1 wt.% of NaCl),  $CN_{x-4}$  (half-saturation, 15.84 wt.% of NaCl), and  $CN_{x-5}$  (saturation, 26.92 wt.% of NaCl).

group of nanoparticles, their intervals of dimensions ( $D$ -diameter and  $L$ -length) and aspect ratio (AR) obtained from each sample are listed. In general the magnetic measurements confirm the ferromagnetic nature of the samples.  $CN_{x-1}$  exhibits a hysteresis loop shown in Figure 8(a); the forest is aligned perpendicularly to the substrate, clean and free of amorphous carbon material on its surface. The nanoparticles of this sample have a conical morphology that is usually located at the tip of the N-MWCNTs. As an example, see the SEM image in the blue square for acetone, where you can see the top of the forest of N-MWCNTs. The contrast of the image allows appreciating the conical nanoparticles with maximum aspect ratio of 5. Their diameters and lengths are within the ranges 20–60 nm and 90–276 nm, respectively. The inset drawing represents the morphology which can take the nanoparticle when encapsulated by N-MWCNTs. The inserted HRTEM image shows the morphology with conical shape in N-MWCNTs [39]. Hysteresis loops of samples

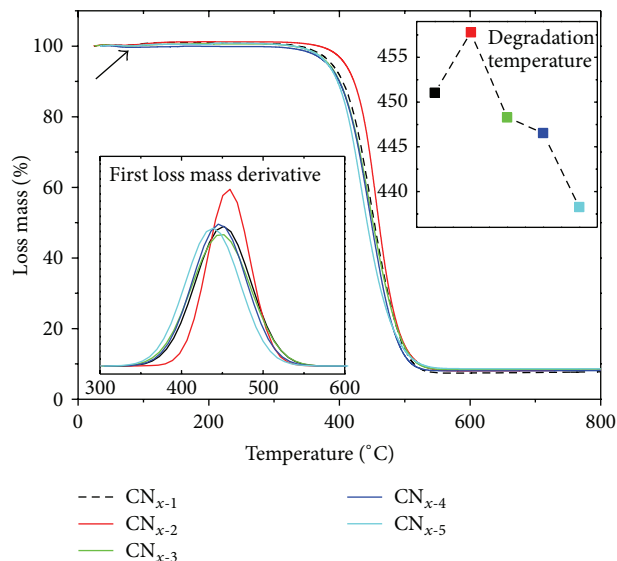


FIGURE 6: Thermogravimetric profile of N-MWCNTs synthesized using different substances in the trap (acetone, deionized water, and three concentrations by weight of NaCl). The insets correspond to the first derivative of thermogravimetric profile (left) and degradation temperature.

synthesized with the other substances are similar to acetone (see Figures 8(b)–8(e)), but properties are quite different. The respective forests show that CNTs are also aligned with some defects and amorphous material on the surface (Figures 8(g)–8(j)). The morphologies of the nanoparticles is totally different from each other (see drawings in each case); we can say that nanoparticles shape is dependent on the type of substance used in the trap. For the cases of  $CN_{x-2}$  ( $H_2O$ ) and  $CN_{x-3}$  (1 wt.% NaCl) nanoparticles have very similar morphologies, including nanowires with aspect ratios greater than 5. The diameters and lengths of the nanoparticles for  $CN_{x-2}$  are in the ranges 3–78 nm and 23–479 nm, respectively, while for  $CN_{x-3}$  the diameters and lengths are within the ranges of 8–60 nm and 11–348 nm, respectively. The aspect ratios are 16 and 25 for  $CN_{x-2}$  and  $CN_{x-3}$ , respectively, and the nanoparticles lengths in  $CN_{x-3}$  can be more than 1 micron. When increasing the NaCl weight concentration the dimensions of nanoparticles take smaller dimensions. This fact is confirmed by the data reported in each case.  $CN_{x-4}$  (half-saturation of NaCl) shows faceted nanoparticle morphologies, with diameter and length within the ranges of 8–60 nm and 11–348 nm, respectively, and aspect ratio of 10.  $CN_{x-5}$  (saturated aqueous solution of NaCl) has nanoparticles with diameters within the range of 5–22 nm and length of 7–118 nm, with lower aspect ratio of 10.

The analysis of hysteresis curves (saturation, coercive field, and remanence versus temperature) is presented in Figure 9. The saturation as a function of temperature is exhibited in Figure 9(a) where we can see that it is easier to saturate the ferromagnetic material contained in  $CN_{x-2}$  (water) and  $CN_{x-3}$ ,  $CN_{x-4}$ , and  $CN_{x-5}$  (with aqueous solutions of NaCl) than  $CN_{x-1}$  (acetone). Figure 9(b) presents the plot of coercive field as a function of temperature for the five samples.

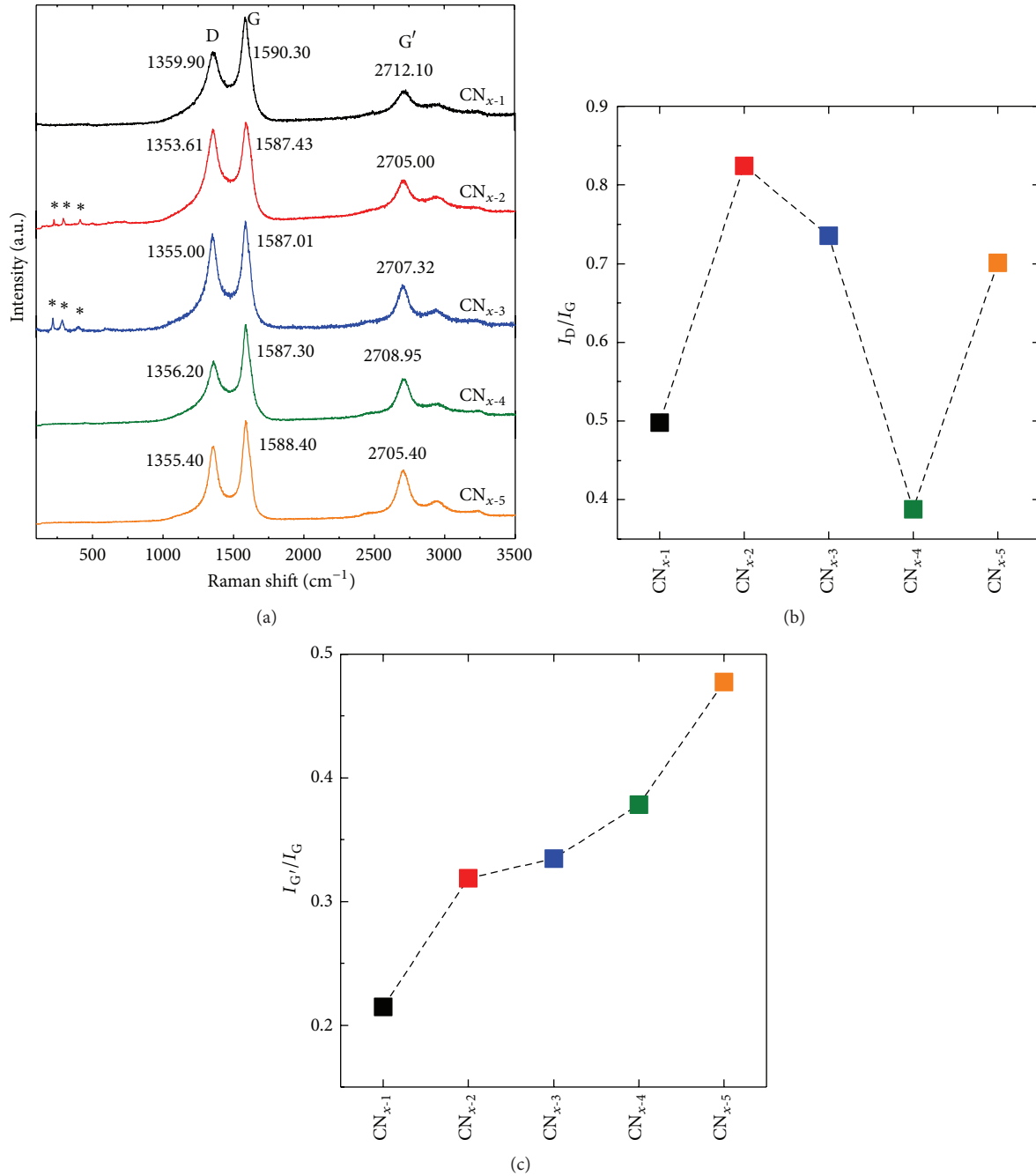


FIGURE 7: (a) Raman spectra of N-MWCNTs synthesized using different substances in the residual bubbler: acetone (C<sub>3</sub>H<sub>6</sub>O), water (H<sub>2</sub>O), and aqueous solution of NaCl at three weight concentrations (1%, 15.48%, and 26.92%). The RBM: D, G, and G' modes are listed in each spectrum. The asterisks indicate that some peaks related to the signals come from Si/SiO<sub>2</sub> substrates. Rates (b)  $I_D/I_G$  and (c)  $I_{G'}/I_G$  plotted as a function of the sample.

The coercive field decreases when increasing temperature in all samples, but the values decrease for CN<sub>x-2</sub>, CN<sub>x-4</sub>, and CN<sub>x-5</sub>. The sample CN<sub>x-3</sub> is very similar to CN<sub>x-1</sub>. The remanence, shown in Figure 9(c), has a decreasing trend as a function of temperature for each sample. However, the remanence decreases for the cases of nanoparticles synthesized N-MWCNTs contained in different substances into the trap, with lower values for CN<sub>x-5</sub>.

According to Figure 9 the most notable changes observed in the magnetic properties are related to the magnetization saturation. Since the iron carbide and  $\alpha$ -Fe phases are present in all cases, these changes could be associated with the presence of iron oxides phases (see X-ray diffractograms of Figure 5) or due to the morphological changes of magnetic nanoparticles inside or attached to CNT [40, 41]. For example, CN<sub>x-1</sub>, which is the control sample, presents

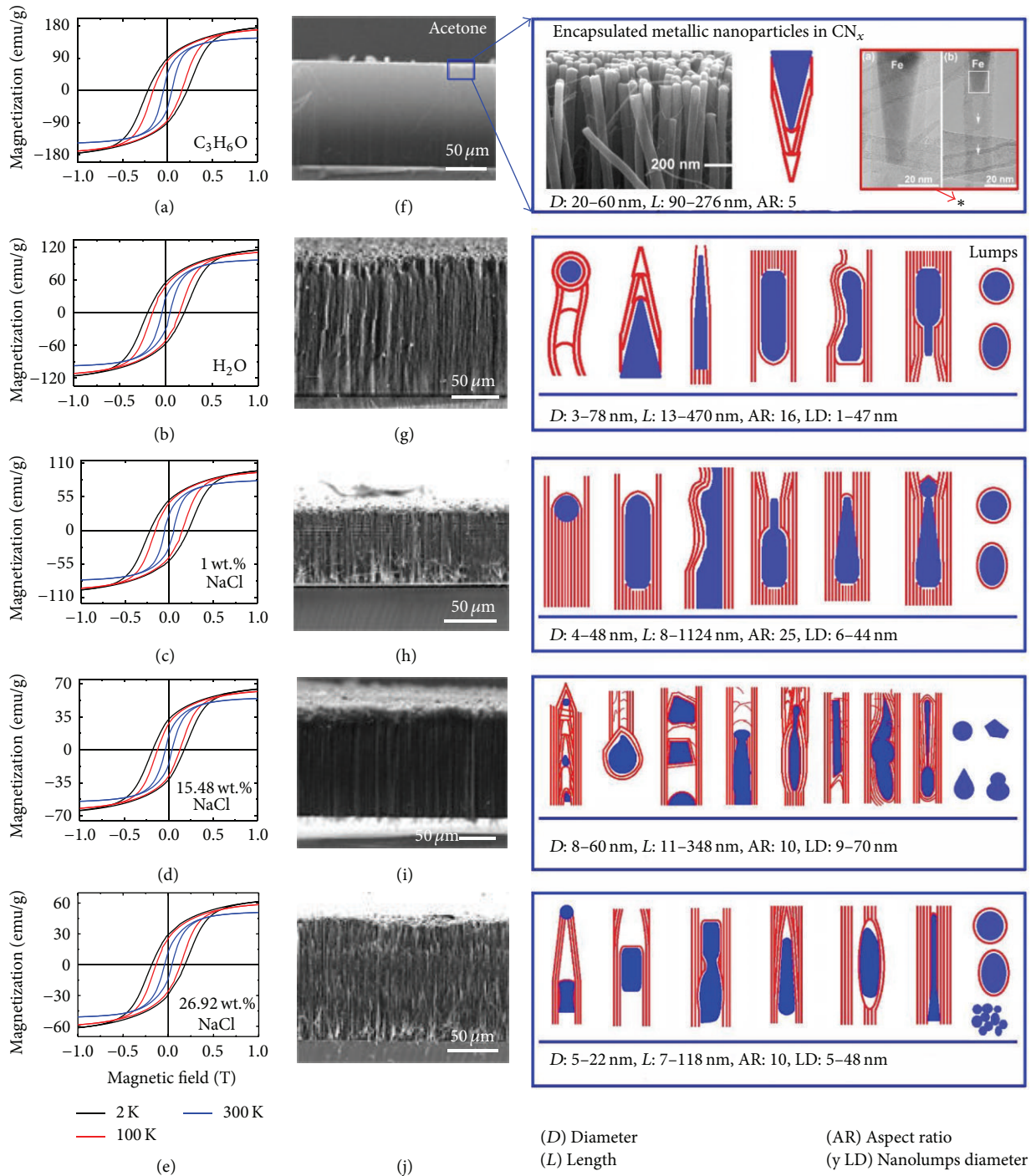


FIGURE 8: (a–e) Hysteresis loops measured at 2, 200, and 300 K for encapsulated metallic nanoparticles in CN<sub>x</sub> synthesized using different substances inside the trap. (f–j) SEM images of CN<sub>x</sub> forests grown over silicon substrates and drawings of the encapsulated nanoparticles in CN<sub>x</sub>. \* Courtesy and permission from [39].

mostly the typical Fe<sub>3</sub>C with a high saturation magnetization. Although some other important peaks were not observed, it is very probable that α-Fe phase is also present (the peak with the maximum intensity is located around 45 degrees). The shape of magnetic nanoparticles in this case is conical with an aspect ratio around 3. Even though the majority

of the magnetic phase is also Fe<sub>3</sub>C in CN<sub>x-2</sub> samples, the saturation magnetization is reduced when water is used in the trap (see Figure 8(b)). One of the probable explanations to this behavior is the morphology changes in the nanoparticles. A statistical analysis was performed to 60 TEM images of CN<sub>x-2</sub> case, which showed that 34% of the nanoparticles

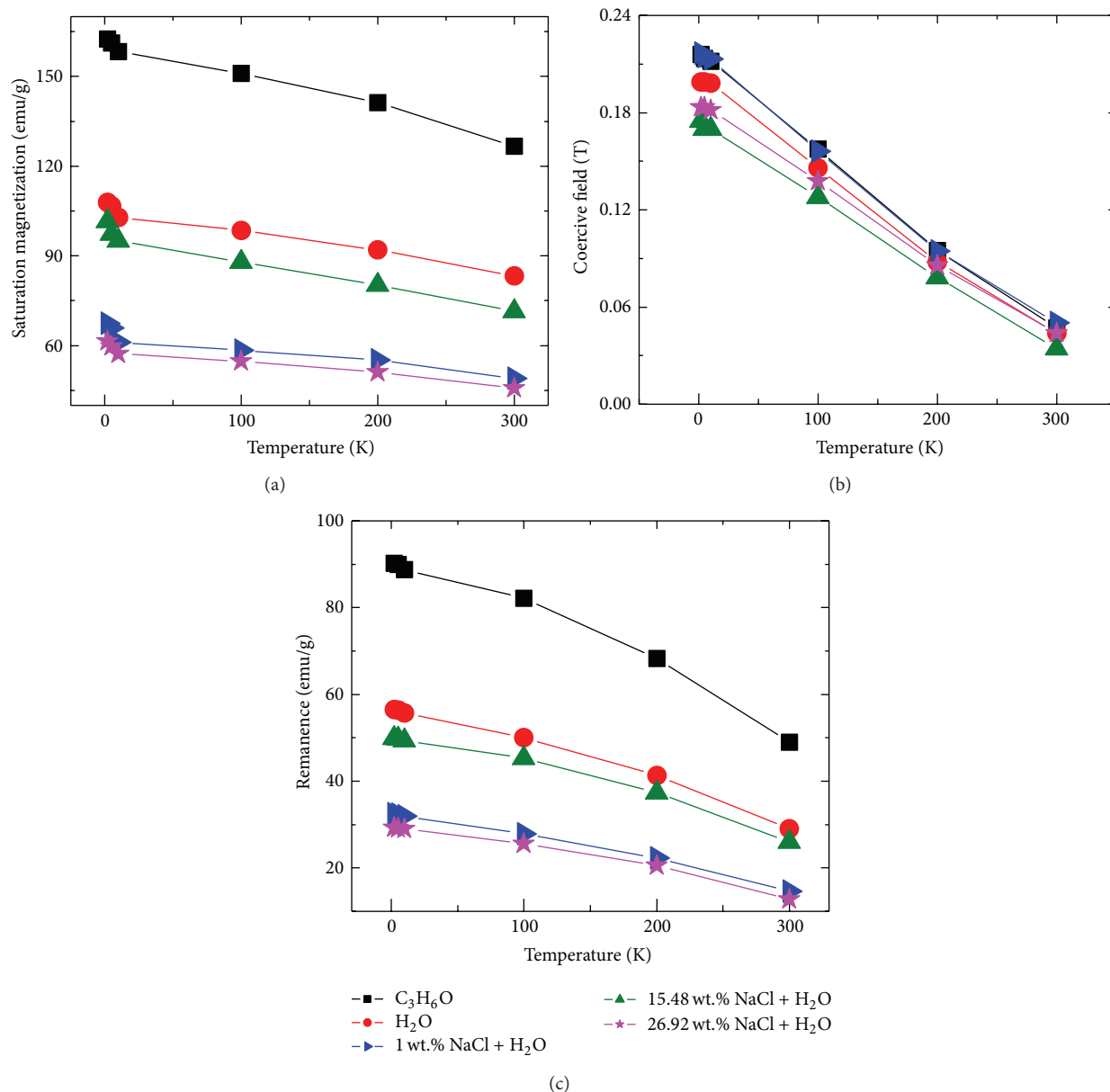


FIGURE 9: (a) Saturation, (b) coercivity, and (c) remanence values as a function of temperature for encapsulated metallic nanoparticles in  $CN_x$  synthesized in acetone ( $CN_{x-1}$ ), water ( $CN_{x-2}$ ), and various concentrations by weight NaCl in water ( $CN_{x-3}$ ,  $CN_{x-4}$ , and  $CN_{x-5}$ ).

have a spherical shape (first drawing) and the other 66% presented other kinds of morphologies (see right drawings of Figure 8(g)). The reduction of the saturation magnetization in this case is around 33.3%, which is approximately the percentage of nanoparticles which are spherical in type. However, there is another source that could contribute to the reduction of saturation magnetization, namely, the magnetite phase present in this sample. The peak at around 35 degrees shows the existence of that phase in sample  $CN_{x-2}$  (see  $CN_{x-2}$  diffractogram in Figure 5). Note that it was not possible to observe the peak having the second strongest value, which is around 62 degrees. Magnetite in bulk phase has a saturation magnetization of around 85–100 emu/g, which is around 50% lower than the respective saturation magnetizations

of  $Fe_3C$  (169 emu/g for bulk) phase [42–45]. Therefore, a combination of such effects could be the cause of the observed changes. In the case of  $CN_{x-3}$  the statistical analysis yielded the fact that only 6.8% of the magnetic nanoparticles have a spherical shape. Therefore, the effect of morphology changes of magnetic nanoparticles may not be important. However, now the  $\gamma-Fe_2O_3$  phase is present in this sample and could be one of the cause of the reduction of saturation magnetization. If the  $CN_{x-2}$  and  $CN_{x-3}$  X-ray diffractograms of Figure 5 are compared, it is possible to observe that in the  $CN_{x-3}$  case two additional diffraction peaks are present. These peaks are around 34 and 54 degrees and might be associated with (311) and (422) planes of the maghemite ( $\gamma-Fe_2O_3$ ) phase, which has around 90 emu/g of saturation magnetization in the case

of bulk phase. The presence of  $\gamma$ -Fe<sub>2</sub>O<sub>3</sub> and Fe<sub>3</sub>O<sub>4</sub> phases could be causing the saturation magnetization to reduce by more than 50% (see Figure 9(a)). An interesting situation is observed in the X-ray diffractogram of case CN<sub>x-4</sub>. The diffraction peaks corresponding to (311) and (422) planes of the maghemite phase are not present anymore and the structure corresponding to the Fe<sub>3</sub>C phase is drastically modified (see Figure 5 CN<sub>x-4</sub> case). Also, the diffraction peak at 35 degrees related to the Fe<sub>3</sub>O<sub>4</sub> magnetite phase is notably reduced. In addition, three new diffraction peaks are present, namely, at around 29, 56, and 77 degrees. The first two peaks correspond to (220) and (551) planes of magnetite and the last peak corresponds to (140) plane of cementite. Note how the intensity of the peak at around 43 degrees is greatly increased in comparison with the other Fe<sub>3</sub>C diffraction peaks. This peak can also be associated with the (400) plane of magnetite. Apparently, the magnetic behavior in this case is due to different causes than the previous situations. It is probable that the magnetic magnetite, cementite, and  $\alpha$ -Fe phases are those that determine the behavior of the saturation magnetization. Note also that the phase of maghemite was not well observed. Figure S8 (Supplementary Information) shows that, in elongated nanoparticles, mostly  $\alpha$ -Fe and cementite phases are contained. In this case, in order to explain the increase of saturation of magnetization, additional information that we need to consider is the morphological changes experienced by magnetic nanoparticles. The drawings on the left side of Figure 8(i) show complex structures of the encapsulated nanoparticles in CN<sub>x-4</sub>. According to a statistical analysis, it was found that only 8.6% of them have spherical shape and the rest present an elongated structure. It is noteworthy that some nanoparticles have square-type morphology (see Figure S7 in Supplementary Information). Finally, the X-ray diffractogram of CN<sub>x-5</sub> does not show any Fe-oxides phases. Only defined diffraction peaks of Fe<sub>3</sub>C and  $\alpha$ -Fe planes were observed. It seems that, in this case, the morphology changes are the only ones responsible for the observed decrease of saturation magnetization (more than 50%). Figure S9 shows several HRTEM images of such nanoparticles. These particles take different shapes such as spherical (13%), cylindrical (28%), deformed (23%), seed (28%), oval (5%), and arrow (3%) [27]. It is well known that if the morphologies of the ferromagnetic nanoparticles are different, it is very probable that the process of magnetization will be strongly dependent upon their shape and size and also on the applied magnetic field direction [39, 41]. The irregular shapes of ferromagnetic nanoparticles in this CN<sub>x-5</sub> case could have reduced the saturation magnetization due to surface or finite size effects [46, 47]. Note that the coercivity values follow the trend in aspect ratio where CN<sub>x-3</sub> with an aspect ratio of 25 had the highest values and the samples with the lowest aspect ratio of 10 (CN<sub>x-4</sub> and CN<sub>x-5</sub>) exhibited the lowest coercivity (see drawings of Figure 8).

The resistance of the N-MWCNTs was measured by the four-probe method as a function of the temperature in the range 2–395 K (Figure 10). The resistance of CN<sub>x-2</sub> is an order of magnitude higher than CN<sub>x-1</sub> and CN<sub>x-3</sub> (Figure 10(a)), but the three resistance curves have similar behavior. However the resistance of CN<sub>x-4</sub> and CN<sub>x-5</sub> (Figure 10(b)) is two orders

of magnitude lower than CN<sub>x-1</sub> with a different curve behavior. All samples showed two kinds of behaviors of electronic transport. The samples CN<sub>x-1</sub>, CN<sub>x-2</sub>, and CN<sub>x-3</sub> showed semiconducting electronic transport with very large values of resistivity at low temperatures (2 K). The samples CN<sub>x-4</sub> and CN<sub>x-5</sub>: (i) at very low temperatures (below 20 K) the slope of the resistance increases when temperature decreases; (ii) between 20 K and 300 K, the resistance increases with the increment of temperature showing metallic behavior. It is not possible to associate these two last behaviors with the N-MWCNTs themselves. However, it is very probable that some Na contamination of the substrates during the synthesis occurred. Results from OES characterization of samples (substrates and N-MWCNTs) obtained by the additional experiments, which were performed to verify the effect of trap substance over morphology and physical properties, showed that when the trap is filled with aqueous solution of NaCl (15.84 wt.% case) a gram of N-MWCNTs contains 0.204 mg of Na and in each gram of Si substrate there is 0.00835 mg of Na. This could explain the metallic transport at temperatures above 20 K. Similar kind of effect has been observed by p-doping with the intercalation of I, K, and Br within SWNT bundles, with a metallic-like behavior at high temperatures (>50 K) and semiconducting behavior at lower temperatures (<50 K) [48, 49]. However the mechanism is not yet well understood and we encourage more research regarding this effect.

In the CVD experiment we are proposing the use of different liquids other than acetone. We have used water and aqueous solutions of NaCl at three weight concentrations (1%; 15.48%, half-saturation; and 26.92%, saturation). In all cases we consider that a reflux evaporation of water molecules and some atoms of Na or Cl are entering to the hot zone of the furnace and participating in the catalysis of N-MWCNTs. The feedstock that contains the C, Fe, and N is carried by the argon gas. However, it seems that the reflux evaporation is also present in the process of synthesis. For example, in the case of water the oxygen directly affects the catalytic particles, keeping the catalyst alive [13, 14]. This effect could be responsible for the different nanoparticle shapes that catalyze N-MWCNTs in different morphologies, sizes, and diameters. In the case of H, this can be associated with C forming hydrocarbons which probably could be cleaned by the gas. In the case of the presence of NaCl the steps are similar, but the water evaporation is different because NaCl was solubilized in water, where the water molecules are attracted by the Na<sup>+</sup> and Cl<sup>-</sup> ions. The water is attracted by the crystal structure in the individual ions encircling and dissolving slowly the NaCl. The water molecules alignment depends on the ion kind (Na<sup>+</sup> or Cl<sup>-</sup>). The negative part of water molecule (O) surrounds the Na<sup>+</sup> ion, while the positive side (H) surrounds the Cl<sup>-</sup> ion. Taking into account this limitation to water, we may consider the fact that less water vapor is refluxing to the hot zone as well as some Na<sup>+</sup> or Cl<sup>-</sup> are entering by the water evaporation. In the case of saturated NaCl there are not available water molecules due to the fact all of them are associated with ions. First, water molecules and ions surrounded by water molecules are contaminating the feedstock deposited in the substrate. CNT

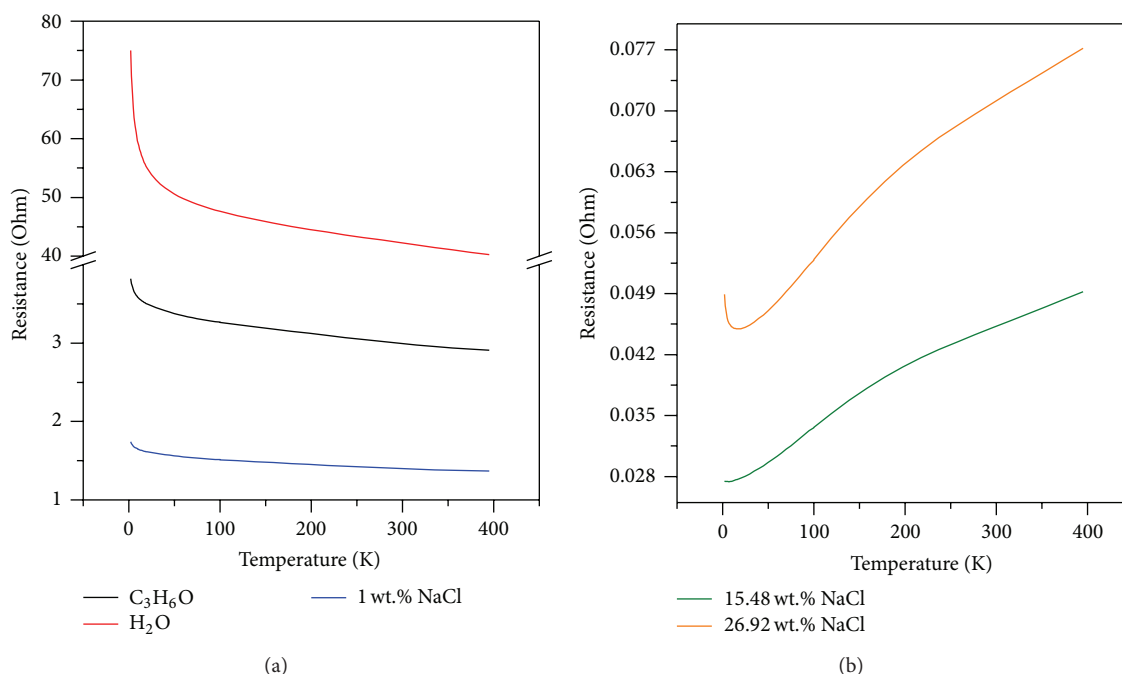


FIGURE 10: Resistance behavior of  $CN_x$  synthesized with different substances in the residual bubbler of CVD setup. (a) Black line corresponds to  $CN_{x-1}$  (acetone), red line to  $CN_{x-2}$  (water), and blue line to  $CN_{x-3}$  (aqueous solution of 1 wt.% of NaCl) and (b) red line corresponds to  $CN_{x-4}$  (aqueous solution of 15.48 wt.% of NaCl) and orange line to  $CN_{x-5}$  (aqueous solution of 26.92 wt.% of NaCl). Resistances of  $CN_{x-1}$ ,  $CN_{x-2}$ , and  $CN_{x-3}$  have typical semiconducting behavior. At the same time, the samples prepared with aqueous solution NaCl in the residual bubbler show metallic response above 20 K and semiconducting behavior at very low temperature.

has started growing but encapsulating small nanoparticles, at different sites in the hollow structure. The effects of the water molecules have an effect similar to the previous case, but in this case the Na or Cl ions are also participating in the catalysis, probably reducing the sizes of nanoparticles. In order to alternatively test how the Na or Cl could be affecting the growing of carbon nanotubes a specific experiment was performed. Instead of introducing aqueous solution of NaCl (case 15.84 wt.%) inside the trap, a more complicated CVD setup was used to fabricate the carbon nanotubes (see Figure S5 in Supplementary Information). In this case two sprayers were used, one with the typical solution containing benzylamine and ferrocene and the other with an aqueous solution of NaCl. Both systems were switched on at same time with different sprayer conditions of frequency and power to tray to obtain similar results to the original experiment with the trap. A total of 335 mg of powder was obtained from the quartz tube. Figure S6 (Supplementary Information) shows the fabricated N-MWCNTs selected from different part of the sample, which show different lengths but similar aspect at the magnification showed (see Supplementary Information) [50]. From these images it was possible to observe the dramatic damages due to the NaCl vapor introduced in the synthesis. More research using this bi-sprayer system is in progress.

#### 4. Summary

The CVD configuration was modified to synthesize controlled morphologies in nitrogen-doped carbon nanotubes

by increasing the density of the liquid trap used in the bubbler. The SEM and HRTEM images revealed the fact that the morphology of N-MWCNTs was modified substantially exploding the versatility of CVD. We studied the present morphologies in the sample by observing the hollow core morphology, which resulted in the fact that the bamboo structure not only was observed, but also collapsed, MWCNT, and different junctions. When increasing the density of the liquid in the residual bubbler it affected not only the tube morphology, but also the metallic nanoparticles morphology. X-Ray diffraction showed the presence of different phases of iron such as oxides (magnetite and maghemite) and most of the planes were observed in N-MWCNTs synthesized with water ( $CN_{x-2}$ ) and low concentration of NaCl + H<sub>2</sub>O ( $CN_{x-3}$ ) in the bubbler. The peaks of planes of iron oxides are not usually observed in samples of N-MWCNTs synthesized with acetone in the bubbler. Raman and thermogravimetric analysis exhibited the fact that water produces a noncrystalline sample that could be attributed to the high degree of disorder in the sample or high level of amorphous carbon. Yet, the presence of NaCl in water showed samples with higher crystalline structure and more reactivity. Magnetic measurements lower coercive fields, remanence, and saturation for the increment of NaCl. Resistivity plots revealed the semiconducting nature of the N-MWCNTs synthesized with water and low NaCl, similar to acetone, but with different orders of magnitude. The samples synthesized with aqueous solution of NaCl showed metallic behavior due to the fact that the resistances were increased with the increment of temperature.

More sophisticated experiments can be designed to tune the morphological and chemical and physical properties of N-MWCNTs.

### Conflict of Interests

The authors declare that there is no conflict of interests regarding the publication of this paper.

### Acknowledgments

Authors thank the support by CONACYT-Mexico grants: Fondo Mixto de San Luis Potosí 63001 S-3908 and 63072 S-3909 (Emilio Muñoz-Sandoval), 48300 (Emilio Muñoz-Sandoval), and CONACYT Scholarship of María Luisa García-Betancourt no. 223824. María Luisa García-Betancourt also thanks access to LINAN-IPICyT and Physics Department, Penn State, for experimentation and characterization in development of PhD thesis project. They thank B. Rivera-Escoto, G. Labrada, F. Tristan, H. Martínez, and D. Ramírez for technical support.

### References

- [1] A. Oberlin, M. Endo, and T. Koyama, "Filamentous growth of carbon through benzene decomposition," *Journal of Crystal Growth*, vol. 32, no. 3, pp. 335–349, 1976.
- [2] S. Iijima, "Helical microtubules of graphitic carbon," *Nature*, vol. 354, no. 6348, pp. 56–58, 1991.
- [3] L. Ding, A. Tselev, J. Wang et al., "Selective growth of well-aligned semiconducting single-walled carbon nanotubes," *Nano Letters*, vol. 9, no. 2, pp. 800–805, 2009.
- [4] N. Yamamoto, A. J. Hart, E. J. Garcia et al., "High-yield growth and morphology control of aligned carbon nanotubes on ceramic fibers for multifunctional enhancement of structural composites," *Carbon*, vol. 47, no. 3, pp. 551–560, 2009.
- [5] B. H. Hong, J. P. Small, M. S. Purewal et al., "Extracting subnanometer single shells from ultralong multiwalled carbon nanotubes," *Proceedings of the National Academy of Sciences of the United States of America*, vol. 102, no. 40, pp. 14155–14158, 2005.
- [6] K. T. Constantopoulos, C. J. Shearer, A. V. Ellis, N. H. Voelcker, and J. G. Shapter, "Carbon nanotubes anchored to silicon for device fabrication," *Advanced Materials*, vol. 22, no. 5, pp. 557–571, 2010.
- [7] M. A. Mohamed, N. Inami, E. Shikoh, Y. Yamamoto, H. Hori, and A. Fujiwara, "Fabrication of spintronics device by direct synthesis of single-walled carbon nanotubes from ferromagnetic electrodes," *Science and Technology of Advanced Materials*, vol. 9, no. 2, Article ID 025019, 2008.
- [8] P. M. Ajayan and O. Z. Zhou, "Applications of carbon nanotubes," in *Carbon Nanotubes*, pp. 391–425, Springer, Berlin, Germany, 2001.
- [9] S.-H. Jeong, O.-J. Lee, K.-H. Lee, S.-H. Oh, and C.-G. Park, "Packing density control of aligned carbon nanotubes," *Chemistry of Materials*, vol. 14, no. 10, pp. 4003–4005, 2002.
- [10] J. Zhao, H. Park, J. Han, and J. P. Lu, "Electronic properties of carbon nanotubes with covalent sidewall functionalization," *The Journal of Physical Chemistry B*, vol. 108, no. 14, pp. 4227–4230, 2004.
- [11] S. Bellucci, "Carbon nanotubes: physics and applications," *physica status solidi C*, vol. 2, no. 1, pp. 34–47, 2005.
- [12] J.-C. Charlier, "Defects in carbon nanotubes," *Accounts of Chemical Research*, vol. 35, no. 12, pp. 1063–1069, 2002.
- [13] K. Hata, D. N. Futaba, K. Mizuno, T. Namai, M. Yumura, and S. Iijima, "Water-assisted highly efficient synthesis of impurity-free single-walled carbon nanotubes," *Science*, vol. 306, no. 5700, pp. 1362–1364, 2004.
- [14] T. Yamada, A. Maigne, M. Yudasaka et al., "Revealing the secret of water-assisted carbon nanotube synthesis by microscopic observation of the interaction of water on the catalysts," *Nano Letters*, vol. 8, no. 12, pp. 4288–4292, 2008.
- [15] L. Ding, A. Tselev, J. Wang et al., "Selective growth of well-aligned semiconducting single-walled carbon nanotubes," *Nano Letters*, vol. 9, no. 2, pp. 800–805, 2009.
- [16] Y. Zhang and X. Sun, "Synthesis of carbon nanofibers and foam by catalytic chemical vapor deposition using a water-soluble alkali salt catalyst," *Advanced Materials*, vol. 19, no. 7, pp. 961–964, 2007.
- [17] Y. Qin, Y. Zhang, and X. Sun, "Synthesis of helical and straight carbon nanofibers by chemical vapor deposition using alkali chloride catalysts," *Microchimica Acta*, vol. 164, no. 3-4, pp. 425–430, 2009.
- [18] R. Lv, F. Kang, W. Wang et al., "Effect of using chlorine-containing precursors in the synthesis of FeNi-filled carbon nanotubes," *Carbon*, vol. 45, no. 7, pp. 1433–1438, 2007.
- [19] X. Gui, K. Wang, W. Wang et al., "The decisive roles of chlorine-contained precursor and hydrogen for the filling Fe nanowires into carbon nanotubes," *Materials Chemistry and Physics*, vol. 113, no. 2-3, pp. 634–637, 2009.
- [20] D. Wei and Y. Liu, "The intramolecular junctions of carbon nanotubes," *Advanced Materials*, vol. 20, no. 15, pp. 2815–2841, 2008.
- [21] C. Zhou, J. Kong, E. Yenilmez, and H. Dai, "Modulated chemical doping of individual carbon nanotubes," *Science*, vol. 290, no. 5496, pp. 1552–1555, 2000.
- [22] J. M. Romo-Herrera, D. A. Cullen, E. Cruz-Silva et al., "The role of sulfur in the synthesis of novel carbon morphologies: From covalent Y-junctions to sea-urchin-like structures," *Advanced Functional Materials*, vol. 19, no. 8, pp. 1193–1199, 2009.
- [23] X. Lepró, Y. Vega-Canú, F. J. Rodríguez-Macías, Y. Bando, D. Golberg, and M. Terrones, "Production and characterization of coaxial nanotube junctions and networks of CN<sub>x</sub>/CNT," *Nano Letters*, vol. 7, no. 8, pp. 2220–2226, 2007.
- [24] Z. Jin, X. Li, W. Zhou, Z. Han, Y. Zhang, and Y. Li, "Direct growth of carbon nanotube junctions by a two-step chemical vapor deposition," *Chemical Physics Letters*, vol. 432, no. 1-3, pp. 177–183, 2006.
- [25] Q. Liu, W. Liu, Z.-M. Cui, W.-G. Song, and L.-J. Wan, "Synthesis and characterization of 3D double branched K junction carbon nanotubes and nanorods," *Carbon*, vol. 45, no. 2, pp. 268–273, 2007.
- [26] D. Wei, Y. Liu, L. Cao et al., "A new method to synthesize complicated multibranch carbon nanotubes with controlled architecture and composition," *Nano Letters*, vol. 6, no. 2, pp. 186–192, 2006.
- [27] M. L. García-Betancourt, Y. Vega-Cantu, S. M. Vega-Díaz et al., "Synthesis, characterization and magnetic properties of defective nitrogen-doped multiwall carbon nanotubes encapsulating ferromagnetic nanoparticles," *Journal of Nano Research*, vol. 28, pp. 39–49, 2014.

- [28] M. L. García-Betancourt, N. Perea Lopez, S. M. Vega-Díaz et al., "Pinetree-like morphologies of nitrogen-doped carbon nanotubes: electron field emission enhancement," *Journal of Materials Research*, vol. 29, pp. 2441–2450, 2014.
- [29] J. W. Jang, C. E. Lee, S. C. Lyu, T. J. Lee, and C. J. Lee, "Structural study of nitrogen-doping effects in bamboo-shaped multiwalled carbon nanotubes," *Applied Physics Letters*, vol. 84, no. 15, pp. 2877–2879, 2004.
- [30] E. N. Nxumalo and N. J. Coville, "Nitrogen doped carbon nanotubes from organometallic compounds: a review," *Materials*, vol. 3, no. 3, pp. 2141–2171, 2010.
- [31] J. Y. Lao, W. Z. Li, J. G. Wen, and Z. F. Ren, "Boron carbide nanolumps on carbon nanotubes," *Applied Physics Letters*, vol. 80, no. 3, pp. 500–502, 2002.
- [32] C.-M. Seah, S.-P. Chai, and A. R. Mohamed, "Synthesis of aligned carbon nanotubes," *Carbon*, vol. 49, no. 14, pp. 4613–4635, 2011.
- [33] X. Li, X. Zhang, L. Ci et al., "Air-assisted growth of ultralong carbon nanotube bundles," *Nanotechnology*, vol. 19, no. 45, Article ID 455609, 2008.
- [34] V. O. Khavrus, E. M. M. Ibrahim, A. Leonhardt et al., "Conditions of simultaneous growth and separation of single- and multiwalled carbon nanotubes," *Journal of Physical Chemistry C*, vol. 114, no. 2, pp. 843–848, 2010.
- [35] T. Sharifi, F. Nitze, H. R. Barzegar et al., "Nitrogen doped multiwalled carbon nanotubes produced by CVD-correlating XPS and Raman spectroscopy for the study of nitrogen inclusion," *Carbon*, vol. 50, no. 10, pp. 3535–3541, 2012.
- [36] D. Bersani, P. P. Lottici, and A. Montenero, "Micro-Raman investigation of iron oxide films and powders produced by sol-gel syntheses," *Journal of Raman Spectroscopy*, vol. 30, no. 5, pp. 355–360, 1999.
- [37] C. J. Sartoretti, B. D. Alexander, R. Solarska, I. A. Rutkowska, J. Augustynski, and R. Cerny, "Photoelectrochemical oxidation of water at transparent ferric oxide film electrodes," *Journal of Physical Chemistry B*, vol. 109, no. 28, pp. 13685–13692, 2005.
- [38] Y.-S. Li, J. S. Church, A. L. Woodhead, and F. Moussa, "Preparation and characterization of silica coated iron oxide magnetic nano-particles," *Spectrochimica Acta Part A: Molecular and Biomolecular Spectroscopy*, vol. 76, no. 5, pp. 484–489, 2010.
- [39] F. López-Urías, E. Muñoz-Sandoval, M. Reyes-Reyes, A. H. Romero, M. Terrones, and J. L. Morán-López, "Creation of helical vortices during magnetization of aligned carbon nanotubes filled with Fe: Theory and experiment," *Physical Review Letters*, vol. 94, no. 21, Article ID 216102, 2005.
- [40] C. Cannas, D. Gatteschi, A. Musinu, G. Piccaluga, and C. Sangregorio, "Structural and magnetic properties of Fe<sub>2</sub>O<sub>3</sub> nanoparticles dispersed over a silica matrix," *The Journal of Physical Chemistry B*, vol. 102, no. 40, pp. 7721–7726, 1998.
- [41] A. Morelos-Gómez, F. López-Urías, E. Muñoz-Sandoval et al., "Controlling high coercivities of ferromagnetic nanowires encapsulated in carbon nanotubes," *Journal of Materials Chemistry*, vol. 20, no. 28, pp. 5906–5914, 2010.
- [42] A. Demir, A. Baykal, H. Sözeri, and R. Topkaya, "Low temperature magnetic investigation of Fe<sub>3</sub>O<sub>4</sub> nanoparticles filled into multiwalled carbon nanotubes," *Synthetic Metals*, vol. 187, no. 1, pp. 75–80, 2014.
- [43] X. Wang, Z. Zhao, J. Qu, Z. Wang, and J. Qiu, "Fabrication and characterization of magnetic Fe<sub>3</sub>O<sub>4</sub>-CNT composites," *Journal of Physics and Chemistry of Solids*, vol. 71, no. 4, pp. 673–676, 2010.
- [44] F. S. Boi, G. Mountjoy, R. M. Wilson, Z. Luklinska, L. J. Sawiak, and M. Baxendale, "Multiwall carbon nanotubes continuously filled with micrometre-length ferromagnetic alpha-Fe nanowires," *Carbon*, vol. 64, pp. 351–358, 2013.
- [45] D. L. Peng, X. Zhao, S. Inoue, Y. Ando, and K. Sumiyama, "Magnetic properties of Fe clusters adhering to single-wall carbon nanotubes," *Journal of Magnetism and Magnetic Materials*, vol. 292, pp. 143–149, 2005.
- [46] H. M. Lu, W. T. Zheng, and Q. Jiang, "Saturation magnetization of ferromagnetic and ferrimagnetic nanocrystals at room temperature," *Journal of Physics D: Applied Physics*, vol. 40, no. 2, pp. 320–325, 2007.
- [47] N. Grobert, W. K. Hsu, Y. Q. Zhu et al., "Enhanced magnetic coercivities in Fe nanowires," *Applied Physics Letters*, vol. 75, no. 21, pp. 3363–3365, 1999.
- [48] R. S. Lee, H. J. Kim, J. E. Fischer, A. Thess, and R. E. Smalley, "Conductivity enhancement in single-walled carbon nanotube bundles doped with K and Br," *Nature*, vol. 388, no. 6639, pp. 255–257, 1997.
- [49] S. Ahn, Y. Kim, Y. Nam et al., "Magnetotransport in iodine-doped single-walled carbon nanotubes," *Physical Review B*, vol. 80, no. 16, Article ID 165426, 2009.
- [50] S. S. Meysami, F. Dillon, A. A. Koós, Z. Aslam, and N. Grobert, "Aerosol-assisted chemical vapour deposition synthesis of multi-wall carbon nanotubes: I. Mapping the reactor," *Carbon*, vol. 58, pp. 151–158, 2013.

## Review Article

# Applications of Nanostructured Carbon Materials in Constructions: The State of the Art

Shu-Nan Lu,<sup>1</sup> Ning Xie,<sup>2,3</sup> Li-Chao Feng,<sup>4</sup> and Jing Zhong<sup>3</sup>

<sup>1</sup>College of Civil Engineering and Architecture, Harbin University of Science and Technology, Harbin 150080, China

<sup>2</sup>School of Transportation Science and Engineering, Harbin Institute of Technology, Harbin 150001, China

<sup>3</sup>School of Civil Engineering, Harbin Institute of Technology, Harbin 150001, China

<sup>4</sup>School of Mechanical Engineering, Huaihai Institute of Technology and Jiangsu Marine Resources Development Research Institute, Lianyungang 222005, China

Correspondence should be addressed to Ning Xie; [xiening@hit.edu.cn](mailto:xiening@hit.edu.cn)

Received 30 September 2014; Accepted 20 April 2015

Academic Editor: Myoung-Woon Moon

Copyright © 2015 Shu-Nan Lu et al. This is an open access article distributed under the Creative Commons Attribution License, which permits unrestricted use, distribution, and reproduction in any medium, provided the original work is properly cited.

The most recent studies on the applications of nanostructured carbon materials, including carbon nanotubes, carbon nanofibers, and graphene oxides, in constructions are presented. First, the preparation of nanostructured carbon/infrastructure material composites is summarized. This part is mainly focused on how the nanostructured carbon materials were mixed with cementitious or asphalt matrix to realize a good dispersion condition. Several methods, including high speed melting mixing, surface treatment, and aqueous solution with surfactants and sonication, were introduced. Second, the applications of the carbon nanostructured materials in constructions such as mechanical reinforcement, self-sensing detectors, self-heating element for deicing, and electromagnetic shielding component were systematically reviewed. This paper not only helps the readers understand the preparation process of the carbon nanostructured materials/infrastructure material composites but also sheds some light on the state-of-the-art applications of carbon nanostructured materials in constructions.

## 1. Introduction

Nanostructured carbon materials, including carbon nanotubes (CNTs), carbon nanofibers (CNFs), graphene (GR), graphene oxide (GO), and fullerene, are promising elements that can be used in many practical areas [1–3]. One of the most important applications of the nanostructured carbon materials is using them to fabricate various composite materials including carbon/polymer [4], carbon/ceramic [5], carbon/cement [6], and carbon/metal [7] composites.

The infrastructure materials are the most commonly used materials in the modern civilization. Some studies demonstrated that, with the addition of nanostructured carbon materials, the overall performances of the infrastructure materials can be modified from various perspectives. It was believed that the nanostructured carbon materials will change the pore structures and hydration process of

the cementitious materials and thus change the mechanical properties or functionalize the infrastructure materials.

Currently, the research on nanostructured carbon in infrastructure materials is burgeoning. In the former studies, rapid progress and improvements of advanced nanocarbon materials have led to numerous studies for construction materials. Nanotechnology has demonstrated its promising merits in empowering the development of infrastructures with mechanical reinforcement and many other functionalities. In this paper, the most recent studies on the preparation and applications of nanostructured carbon materials, including carbon nanotubes, carbon nanofibers, and graphene oxides, in constructions are presented.

## 2. Preparation

The final properties of the nanostructured carbon composites are determined by their fabrication process. Several methods

were used to prepare the composites in the past decade. Thanks to its low cost, simplicity, and availability, high speed melt mixing process is the most widely used approach to prepare the composites. In this method, the nanostructured carbon material will be dispersed in a matrix material with a high shear mixing condition. The merit of the high speed melting mixing is that it can guarantee a good dispersion of the nanostructured carbon material in a matrix material; however, this process will damage the structure of the CNT, CNF, GR, or GO, which is another important factor governing the final properties of the composites. As a result, how to use low shear mixing speed to protect the structure of the carbon nanomaterials without sacrificing the dispersion condition is still a challenge to fabricate the composites.

Apart from the high speed melt mixing processing, the solution approach with help of sonication is another method to prepare the composites. In this process, the nanostructured carbon material will be dispersed in a liquid form solution by sonication before being mixed with the matrix. In addition, external cooling device has to be applied to avoid the temperature increase during the sonication process.

Unlike the applications in other areas, the applications of the nanostructured carbon materials in constructions have to satisfy some basic requirements before it can be widely accepted in the construction field. First, because the usage of the carbon nanomaterials will be extremely larger than other areas, the high speed melting mixing process in the field will not be realized as easy as in the lab. Second, for the construction applications, the cost of the composite fabrication has to be low before they can be widely applied. Accordingly, the quality and cost control are the top challenges for the applications of the nanostructured carbon materials in constructions.

Because the high speed melting mixing and solution methods are both not able to be easily realized in the construction fields, the surface treatment of the nanostructured carbon materials is becoming a promising approach to realize their good dispersion in a matrix material. In this process, various functional groups will be grafted on the surfaces of the carbon nanomaterials, and the compatibility between the matrix and the functional group will play a key role which decides the final properties of the composites. In some cases, the surface treatment was realized by oxidizing the surfaces of carbon nanomaterials by soaking them into acids at various temperatures followed by acylation. After that, the functional groups will be grafted on the surfaces of the carbon nanomaterials by the reaction between the carbon and the functional groups [14].

In the most recent years, the research of the carbon nanostructured composites in constructions has been focused on investigating effective dispersion methods of the carbon nanomaterials in the construction materials. Yu and Kwon [8] used two methods to realize the good dispersion of the CNT in cement matrix. The first one is called *acid surface treatment* method, which has been widely applied to disperse the CNTs in composites. In this process, the as-received CNTs were soaked in the sulfuric acid and nitric acid (with ratio of 3 : 1) for about 45 min at 110°C. The reactive parts of the CNTs, namely, the ends and the defects, will be easily oxidized

by the oxygen atoms in the acids. As a result, the surface of the CNTs will be grafted on negative charged groups and led to the good dispersion due to the electrostatic repulsions. The second method they used was the so-called *noncovalent surface treatment* of the CNTs. In this method, the CNTs were surface treated with polarized surfactant (sodium dodecyl sulfate) rather than acids. Unlike the acid treatment method, in which the CNT surfaces were grafted with functional groups, the surfactants were wrapped on the CNT surfaces and resulted in the dispersion of CNTs in solutions. After the dispersion treatment, the CNTs were mixed with cement (with 0.1 wt.% of cement) to prepare the composites. Figure 1 shows the SEM image of the CNT/cement composites.

Another acids surface treatment method was applied to prepare well dispersed CNT/cement and CNF/cement composites [15]. In this study, the CNTs and CNFs were surface treated by soaking them in sulfuric acids and nitric acids (with ratio of 2 : 1) at 85°C for an hour with continuous magnetic stirring. After being washed and dried, the surface treated CNTs and CNFs were mixed with water and superplasticizer and sonicated for 20 min and 10 min, respectively. After that, the CNT or CNF solutions were mixed with cement powder (with 0.1 wt.% and 0.2 wt.% of cement) to prepare the composites.

The preparation of well dispersed CNT/cement composites was also investigated by another study with surfactant surface treatment method [9]. In this study, various surfactants were used for the CNT dispersion. The CNTs were mixed with surfactants in aqueous solutions and sonicated at room temperature. Unlike the usual sonication tank with magnetic stirring, a sonicator with 500 W cup-horn high intensity cylindrical tip was used in this study. In addition to the types of surfactants, the concentration effect of the surfactants on the dispersion was investigated as well. It was found that the fracture strength of the composites was increasing followed by decreasing with increasing surfactant/CNT ratio. It was claimed that the optimum surfactant/CNT ratio is about 4.0. Figure 2 shows the effect of the surfactant concentration on the dispersion effect of the CNT in the cement matrix.

A few investigators have found the addition of the CNT/CNF in cement will largely affect the workability of the paste. As a result, how to maintain the workability of the CNT/cement composites became a top challenge. Collins et al. [16] reported the relationship between the dispersion, workability, and strength of CNT/cement composites, in which the CNTs were dispersed with concrete compatible surfactants, including air entraining agents, styrene butadiene rubber (SBS), polycarboxylates, calcium naphthalene sulfonate, and lignosulfonate formulations. It was found that the SBS and calcium naphthalene sulfonate admixtures lead to rapid agglomeration of CNTs; the air entraining agents dispersed CNTs in aqueous solutions very well but agglomeration occurred within days, while the polycarboxylate and lignosulfonate admixtures can provide good dispersion of CNTs in aqueous solutions as long as 9 days.

Meanwhile, Sobolkina divided the surfactant into anionic and nonionic types and investigated the dispersion effect

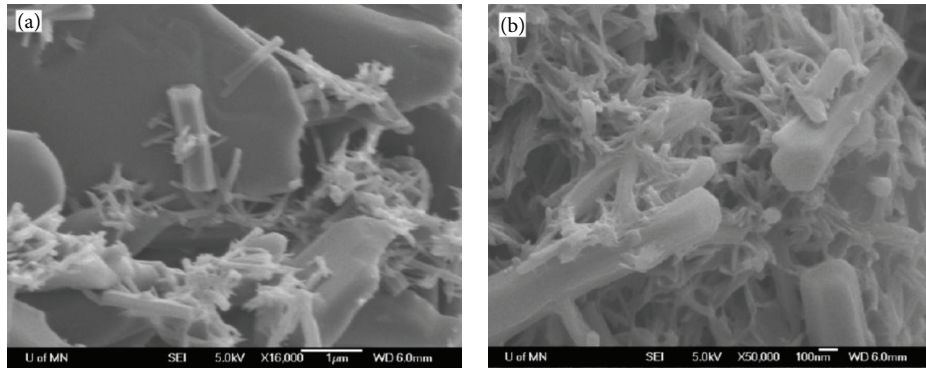


FIGURE 1: The SEM image of the CNT/cement composites [8].

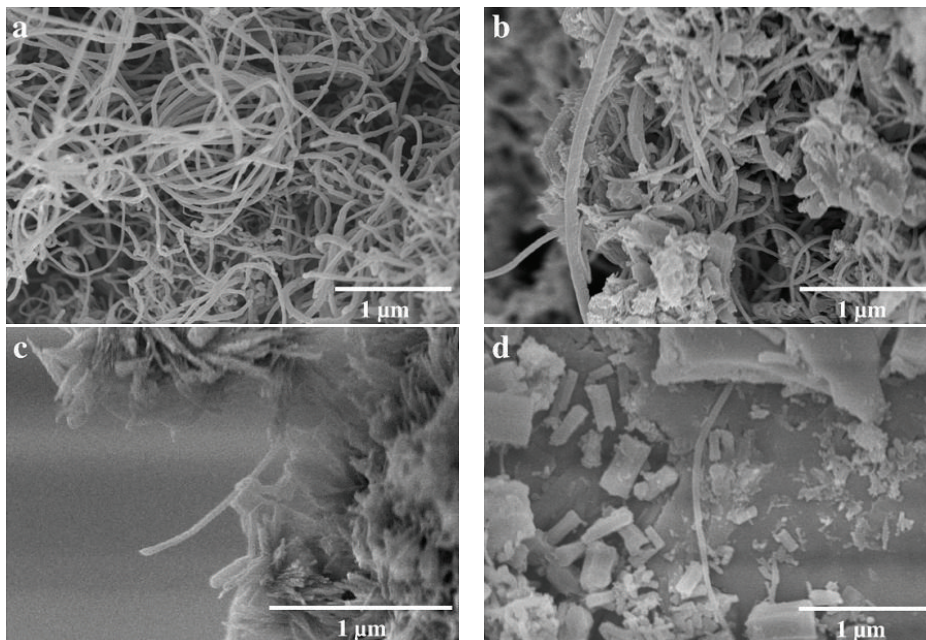


FIGURE 2: Effect of surfactant on the dispersion effect of the CNT in the cement matrix with CNT dosages of (a) 0%, (b) 1.5 wt.%, (c) 4.0 wt.%, and (d) 6.25 wt.% [9].

via UV-vis spectroscopy with sonication time and surfactant concentration as variables [17]. Different from Konsta-Gdoutos' study [9], it was found that the optimum surfactant/CNT ratio is 1:1–1:1.5, and the best sonication time is 120 min.

Other than the sonication time, the sonication energy was also used as parameter to evaluate the dispersion effect of CNF/cement composites [18]. The sonication energies of 2100, 2800, and 3500 kJ/l were applied to dispersion effect of the CNF in the cement matrix. It was found that the composites with sonication energy of 2800 kJ/l demonstrate the best performance.

Comparing with the dispersion process of CNT or CNF in water, the dispersion of GO in water is relatively easier and more stable. In general, the GO nanosheet will be prepared via modified Hummer's method [19]. In this method, the graphite powders were chemically oxidized and diluted in distilled water to prepare the well dispersed GO water

solution. In addition to modified Hummer's method, the stable GO colloid suspension can be obtained by exfoliating the graphite oxide. This GO water solution can be used to prepare the GO/cement composite directly. Gong prepared the GO water solution with modified Hummer's method and fabricated the GO/cement composite [20], and Babak et al. [10] prepared the GO water solution via exfoliation method and prepared the GO/cement composites (shown in Figure 3). Both of their works agreed that the small amount of well dispersed GO addition will evidently enhance the performance of the cement material. Although the GO water solution is more stable than CNT's or CNF's, the study of GO/cement composite is still in its infancy stage and needs to be further systematically investigated in the future studies.

As another important infrastructure material, asphalt has been widely used as binder material for pavement construction, water proof layer at the building roofs, or crack sealer for pavement rehabilitations. Unlike the carbon/cementitious



FIGURE 3: Cement matrix with addition of 1.5 wt.% GO [10].

composite, which has to be cured in a water environment, the carbon/asphalt composite, on the contrary, has to be prepared without water, because the water damage is one of the most important factors that reduce the durability of the asphalt material. Therefore, the dispersion of carbon nanostructured materials in asphalt is more difficult than in cementitious materials. To the best of our knowledge, a few effective ways have been developed to realize the good dispersion of carbon nanostructured materials in asphalt. Although the dispersion problem is still a bottle neck to prepare the nanocarbon/asphalt composite, the investigators are still working on this project with their full enthusiasm.

Because asphalt is a viscoelastic material, it is much easier to prepare the nanocarbon/asphalt composite via high speed melting mixing method. Recently, this method was used to prepare the CNT/bitumen composites [21–24]. Three types of mixers, namely, mechanical mixer, high shear mixer, and ultrasonic mixer, were used to evaluate the dispersion effect of the CNTs in the asphalt matrix. The mechanical mixer, whose motor rotation is a constant while the mixing time is a variable, and the high shear mixer, whose rotation rate is a variable, were used to prepare polymer modified asphalt. The specific designed mixer tip can guarantee a homogenous polymer distribution in asphalt matrix. Sonication mixer is another important mixer that can be used to prepare the nanocarbon/asphalt composite. One thing that has to be noted here is that this apparatus generates large amount of energy and increases the temperature of the composite; therefore, the cooling system might be needed during the mixing process [23, 25].

Combined with sonication and high shear mixing, Khat-tak developed a dispersion method and successfully prepared the well dispersed CNF/asphalt composite. In these studies, the CNFs were firstly thoroughly mixed with kerosene and followed by mixing with asphalt at 60°C. Slowly raise the oil bath temperature to 150°C and keep mixing for 175 min. During this process, the kerosene will be completely evaporated and the CNFs will be homogeneously left in the asphalt matrix [26, 27].

In addition to surfactants and sonication, a new study demonstrates that the addition of appropriate quantity of silica fume has positive effect on the CNF dispersion in cement paste [28]. With normal sonication and surfactants treatment, the CNF/cement composites were prepared

with/without addition of silica fume. It was found that the average dispersion value was 0.73 of the control specimen, while it increased to 0.83% with addition of silica fume (silica/cement = 0.2).

### 3. Applications

**3.1. Reinforcement.** Mechanical properties are always the first priority that needs to be considered before the construction materials can be used in the fields. The application of carbon nanostructured materials as reinforcement has been widely studied in the past decade and accepted as an effective way to enhance the mechanical properties of the infrastructure materials [29–33].

The compressive and splitting tensile strength of the CNT reinforced cement paste were studied by Kumar et al. [34]. In this study, the CNTs were not surface treated. Before mixing with cement, the CNTs were only sonicated for 30 min to 4 h in water. The dosages of the CNTs were 0.5 wt.%, 0.75 wt.%, and 1.0 wt.% of the cement, the water/cement ratio was 0.4, and the curing times were 7, 28, 60, 90, and 180 days. The testing results demonstrated that the samples cured for 28 days with 0.5 wt.% dosage of CNT have the best performance with compressive strength and splitting tensile strength enhancement of 15% and 36% comparing with the control samples.

By combining sonication and surfactants, Hu et al. considerably reduced the dosage of the CNT from 0.5 wt.% of cement to 0.1 wt.% [35]. It was found that, comparing with the control samples, the compressive strength of the CNT modified sample was not evidently enhanced while the fracture energy and fracture toughness were increased 26.2% and 11.4%, respectively.

The rheological performance of the CNT reinforced cement slurries was investigated recently [36]. In this study, the lignosulfonate (0.2%) was used as dispersant in the cement samples. It was found that the rheological performance and stability will not be changed with addition of CNT, while the flexural strength was increased about 15% with the dosage of 0.1% CNT.

Apart from the dosage, the effect of the aspect ratio of CNT on the mechanical properties was investigated as well [37]. Two types of CNTs with high aspect ratio (1250–3750) and low aspect ratio (157) were used to prepare the CNT/cement samples. The testing results showed that, with addition of 0.2 wt.% low aspect ratio CNT, the flexural strength of the 28 days samples increased about 269%, and, with 0.1 high aspect ratio CNT, the flexural strength increased 65%. Meanwhile, the optimized ductility enhancements of the 28 days samples were 86% and 81% with addition of 0.1 and 0.2 low aspect ratio CNTs, respectively.

The reinforcement on compressive and flexural strength of CNF/cement composites was investigated most recently [38, 39]. In this study, the CNFs were dispersed in an aqueous solution with a new surfactant called methylcellulose (MC) by combining with sonication before mixing with cement. It was found that the addition of the CNF to the cement paste has negative effect on the compressive strength of

the CNF/cement composite. However, the 28 days flexural strength was enhanced 21%, and the optimized dosage of the CNF was 0.1 wt.% of cement.

There are some different voices arguing that the addition of the CNT or CNF has negative effects on the mechanical properties of cement paste [15, 16]. It was claimed that extra ettringite will be formed on the acid treated CNT or CNF surfaces, which degraded the mechanical properties of the composites [15].

In addition to cementitious materials, the mechanical performances of the asphalt modified by CNT/CNF were also investigated during the past years [21, 26, 27, 39, 40]. With the addition of CNT from 0.3% to 1.2% weight percent of asphalt, the softening point, penetration depth, complex modulus, fatigue parameter, rutting parameter, and phase change angle of modified asphalt have all improved comparing with the control sample. However, continuously increasing the CNT content from 1.2% to 1.5% has little enhancement effect of the overall performances of the asphalt; therefore, it was claimed that the optimized dosage of the CNT in asphalt should be 1.2% weight of asphalt [39]. The rheological behavior of the CNT modified asphalt was reported recently [25, 40]. It was found that the rheological performance of the asphalt materials can be largely influenced by the addition of CNTs. The viscosity increased about 10% with CNT dosage of 0.1%, 25% with CNT dosage of 0.5%, and above 100% with 1.0% CNT addition [24]. The fatigue testing results also show that the addition of CNT can considerably enhance the fatigue resistance of the asphalt material [40].

Apart from CNT/CNF modified cement composites, the GO addition is also another effective way to enhance the mechanical properties of cementitious materials. Although the results of this area are not quite fruitful, there still are some studies that show their mechanical reinforcement of the composite. A recent study demonstrated that the tensile and flexural strength were both increased with the dosage of GO increased from 0.01 wt.% to 0.03 wt.% and then decreased with the GO content being increased to 0.05 wt.%. Comparing with the control samples, the tensile and flexural strengths of the samples with addition of 0.03 wt.% GO increased 78.6% and 60.7%, respectively. Meanwhile, the highest compressive strength was found in the samples with addition of 0.05 wt.% GO, which increased 47.0% by comparing with the samples without GO addition [41]. Similarly, Gong et al. [20] gives the results that with 0.03 wt.% of GO addition into the cement paste will increase the compressive and tensile strength over 40%. This phenomenon has been further proven by Babak et al. [10]. In that study, it was found that, with 1.5 wt.% of GO in cement, the tensile strength was increased about 50% comparing with the control samples.

Although some studies have demonstrated the overall performances of asphalt can be modified by adding CNT or CNF, the study of the asphalt material modified by GO is still very limited. In addition, there still are some bottle neck problems yet to be solved in the asphalt/nanostructured carbon material composites, such as how to effectively disperse the CNT or CNF in the asphalt, how to use GR or GO to modify the asphalt, and how the durability of the modified

asphalt is. These questions will be the future study trends for the asphalt/nanocarbon composites.

**3.2. Self-Sensing.** Currently, the requirements for self-sensing have become an important characteristic to realize the smart constructions. The nanostructured carbon/cement composites, as a promising self-sensing infrastructure material, have been widely investigated in the past years [2, 8, 12, 42–46].

Technically, the realization of the self-sensing nanostructured carbon/cement composites is originated from evaluating the bulk electrical conductivity/resistivity variation that resulted from the external condition changes, including stress/strain, humidity, temperature, or gas environment, because the electrical properties of the nanostructured carbon/cement composites can be evidently changed with the change of external conditions. It can accurately reflect not only the external conditions of the constructions but also the inside conditions of the composites.

Han et al.'s group did a great contribution in this area during the past decade. They systematically investigated the preparation, properties, and applications of the nanostructure carbon/cementitious composites and discussed their self-sensing performances from both academic and practical perspectives [11, 47–49].

Via testing the variation of its piezoresistive property, which can reflect the stresses status of the materials, the CNT/cement composite was prepared as self-sensing pavement to test the traffic flow [49]. The results showed that this composite has sensitive and stable response to the repeated compressive and impulsive loading, shown in Figure 4 [11]. One year later, they found that the piezoresistivity is largely governed by the water content of the composite [47]. The results indicated that the piezoresistivity values of MWNT/cement composites with water contents of 0.1, 1.3, 3.3, 5.7, 7.6, and 9.9% are 0.60, 0.61, 0.73, 0.68, 0.34, and 0.06 k $\Omega$ /MPa, respectively. Furthermore, they found that the piezoresistivity of the CNT/CNF cementitious composites is largely affected by the dispersant. Many surfactants, including sodium dodecyl sulfate (SDS), sodium dodecylbenzene sulfonate (NaDDBS), and methylcellulose, have been tested and proven to have negative effects on the piezoresistive property until a polycarboxylate superplasticizer was applied as the dispersant [50]. In light of the DC electrical resistivity measurement needing a prepower time to guarantee the resistance reaches its linear increasing stage, which is not convenient for testing, the AC electrical properties tests were developed to overcome the shortcomings of DC electrical resistivity measurements [43]. It was found that the capacitor charging and discharging effect on the pressure-sensitive responses of CNT/cement composites will be eliminated by AC electrical properties testing. In addition, it was claimed that a low-amplitude AC voltage is necessary to improve the pressure sensitivity of the CNT/cement composite.

Via piezoresistivity measurement, another study demonstrated the pressure sensitivity was different with different direction of loadings, namely, compressive and tensile forces [44]. In this study, it was confirmed that the electrical resistance increased with tensile loading, while it decreased

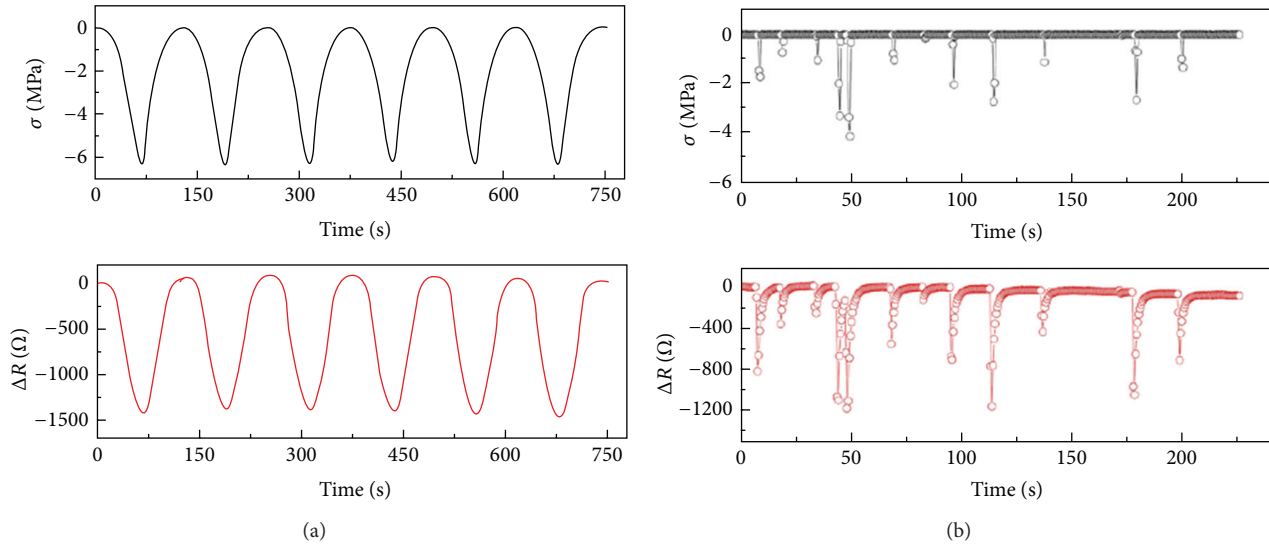


FIGURE 4: The electrical resistance as a function of the external loading of a self-sensing CNT/cement composite. (a) Corresponding to compressive loading of 6 MPa. (b) Corresponding to impulsive loading [11].

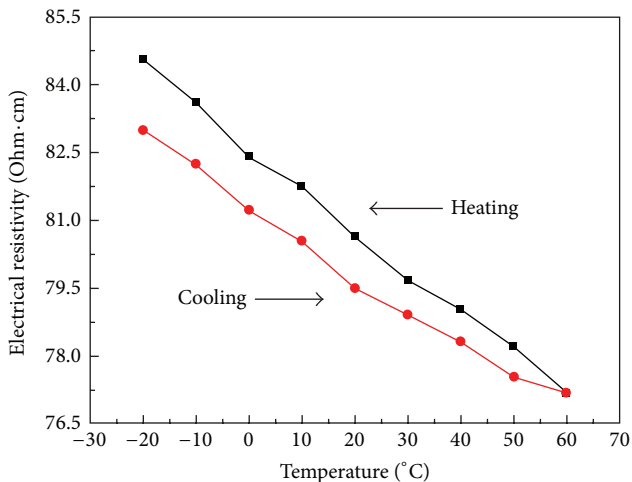


FIGURE 5: Heating and cooling plot of the electrical resistivity as a function of temperature with 0.4 wt.% CF and 2.0 wt.% CNT in a cement matrix [12].

with compression loading. In addition, the sensitivity was determined by the concentration of the CNT. Other than the loading directions, the effect of the water/binder ratio on the piezoresistivity of the CNT/cement composites was investigated as well. It was claimed that the low water/binder ratio has a positive effect on the piezoresistive sensitivity [46].

Other than the stress sensing, the temperature sensing property of the CNT modified cement composites was briefly investigated as well [12]. In that study, it was claimed that the addition of the CNT will clearly result in a temperature sensitivity. Figure 5 shows the heating and cooling relationship between the electrical resistivity and the temperature of the samples with 0.4 wt.% carbon fibers (CF) and 2.0 wt.% CNT in the cement matrix. The temperature sensitivity coefficient

enhanced with the CNT addition increased from 0.2 wt.% to 2.0 wt.%, suggesting that the CNT/CF-cement composites could be applied as the thermistors to reflect the temperatures in concrete structures.

Most recently, the GO/cementitious composites were prepared and used as the self-sensing elements to monitor the infrastructures [51]. The compressive and tensile loading were able to be reflected by the piezoresistivity change of the GO/fly ash geopolymeric composites. In these composites, the GO was easily reduced due to the strong alkaline environment of the fly ash geopolymer. With GO content increased from 0 to 0.35 wt.%, the electrical conductivity of the GO/fly ash geopolymer composite increased from 0.77 S/m to 2.38 S/m. The gauge factors, which are defined as  $k = \Delta R/R_0 \varepsilon$ , were increased about 112% and 103%, corresponding to tension and compression, respectively.

**3.3. Self-Heating Deicing Pavement.** Due to the huge negative impact of the deicing chemicals on the environment and the infrastructure materials [52], the self-heating deicing pavement has been investigated as a replacement of the deicing chemicals to control the ice and snow of the pavement surfaces in cold regions [53, 54]. Using normal commercial carbon fibers as the heating elements to prepare the self-heating deicing concrete, including asphalt and cement, has been widely investigated in the past decade [55, 56]. However, the cost for the electricity consumption of normal CF self-heating pavement is really high; the practical application of this technology has been largely limited.

Thanks to the decreasing fabrication cost of the nanostructured carbon materials, especially carbon nanofibers, they have been investigated as the heating elements to fabricate the self-heating deicing pavement. Due to its high chemical stability, magnificent electrical performances, and outstanding heating efficiency, it has been considered as an

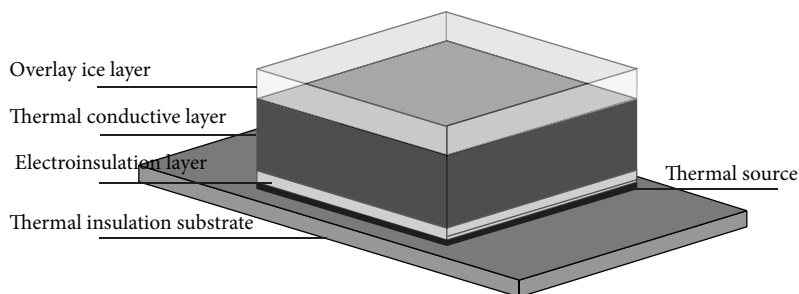


FIGURE 6: Schematic demonstration of a self-heating deicing pavement [13].

effective heating element to prepare the self-heating deicing pavement.

The deicing effects of the carbon nanofibers paper (CNFP) have been studied from numerical and experimental perspectives in recent years and demonstrated its high deicing efficiency. By using air temperature, wind speed, and thickness of the pavement or insulating layer as parameters, a finite element model was developed to evaluate the deicing effect of the CNFP [57] pavement. It was found that the temperature of the pavement equipped with CNFP can be raised up to  $0^{\circ}\text{C}$  with only 20-VAC electrical charge in a relatively short time. In addition, the heating element embedment depth, surface convection conditions, and heating rate are the important factors affecting the heating responding time.

In addition to numerical studies, the experimental research was also carried out to investigate the heating efficiency of the self-deicing pavement [13, 58]. As demonstrated in Figure 6, a multiple layer system was designed to realize the high efficiency self-heating deicing pavement. In this system, the thermal source layer was prepared with CNF/polymer composite, the thermal insulation substrate was made of epoxy polymer, the electroinsulation layer was the AlN ceramics, and the thermal conductive layer was prepared by CNT/cement composite. The results show that the CNT/cement composite has a higher thermal conductivity ( $2.83\text{ W/m}\cdot\text{K}$ ) than normal CF/cement composite ( $1.3\text{--}2.0\text{ W/m}\cdot\text{K}$ ) and plain cement concrete ( $1.58\text{ W/m}\cdot\text{K}$ ). In addition, with a heat flux density of  $600\text{ W/m}^2$ , the covered snow with depth of 20, 30, 40, and 50 mm can be melted in 6000, 6500, 7500, and 6800 seconds with surrounded temperatures of  $-9.1$ ,  $-9.2$ ,  $-9.7$ , and  $-10^{\circ}\text{C}$ , respectively. The corresponding energy consumptions are 1.0, 1.12, 1.28, and  $1.10\text{ kWh/m}^2$ , respectively. By comparing the cost with the former studies, this multiple layer self-heating deicing pavement has a much lower cost ( $0.05\text{--}0.11\text{ \$/m}^2$ ) than CF or steel filled concrete. This experimental study has been compared with numerical study and the results show that the heat flux, air temperature, ice thickness, and wind speed have clear effects on the deicing time, which increases linearly with increasing ice thickness and decreases as a hyperbolic function of the heat-flux density and linearly with air temperature [58].

**3.4. Electromagnetic Shielding.** It has been widely accepted that the conductive concrete has the capability of electromagnetic (EM) wave absorption and can be used to build electromagnetic shielding infrastructures. Comparing with normal CF/cement composites, the CNT (CNF)/cement composites were considered with a higher EM absorption efficiency. Singh et al. [59] investigated the EM interference shielding performance of the CNT/cement composites. It was found that the shielding effectiveness (SE) was dominated by absorption rather than reflection and was higher than 28 dB in X-band ( $8.2\text{--}12.4\text{ GHz}$ ) with 15 wt.% CNT in cement concrete matrix. Due to the effective anisotropy energy and the interfacial polarization of the CNT/cement composite, the high efficient SE can be obtained by the EM wave scattering compared to other carbon/cement composites. Moreover, the dosage of the CNT in the cement matrix has a clear effect on the microwave absorption properties.

Another study demonstrated the EM absorption efficiency of the CNT/cement composite in a relatively low frequency with low CNT dosages. In addition, the effect of the thickness on the EM efficiency of the CNT/cement composite was studied as well [60]. In this study, it was found that the EM wave can be considerably absorbed in a frequency range of  $2\text{--}8\text{ GHz}$  with 0.6 wt.% CNT and a 25 mm thickness of CNT/cement mortar samples. The highest peak of the reflection with value of 28 dB was observed at 2.9 GHz. Similar to other studies, it was found that the EM absorption capability increases with increasing CNT content. The reflection below 10 dB reached 7.1 GHz with addition of 0.9 wt.% CNT.

The EM wave absorption capability in a wider frequency range was evaluated [61]. In this study, the dispersion of the CNT in cement matrix was improved with addition of the silica fume (SF). Unlike the above mentioned studies, this study claimed that the increase of the CNT dosage from 0.3 wt.% to 1.0 wt.% has little effect on the EM SE performance. However, with the synergistic addition of SF (20 wt.%) and CNT (0.6 wt.%), the CNT-SF/cement composites exhibited a good EM wave absorption performance in a wide range of frequency from 45 MHz to 18 GHz. The best EM SE was observed at 0.94 GHz, 1.56 GHz, and 2.46 GHz. In addition, comparing with the samples without addition of SF, the samples with 30 wt.% SF and 1.0 wt.% CNT show the highest enhancement of EM SE with values of 111%, 70%, and

40% corresponding to 0.94 GHz, 1.56 GHz, and 2.46 GHz, respectively.

**3.5. Energy Harvesting.** Although the investigations of the nanostructured carbon/cement as energy harvesting materials are very limited, a few studies were still carried out to test the piezoelectric and thermoelectric performances of the CNT/cement composites. Unlike the piezoresistivity, which is used to evaluate the sensing capability, the piezoelectric performance is used for the energy harvesting from converting the mechanical energy to the electrical energy of the CNT/cement composites. The piezoresistivity of the CNT/cement composites was realized by the backbones or tunneling channels changes of the CNT networks corresponding to external force field change which can result in an electrical conductivity change and reflect the external or internal conditions of the concrete infrastructures; however, the piezoelectricity was realized by changing the polarization status of the CNT/cement composites under external force field and generating an induced electrical field to realize the energy harvesting. Gong et al. [62] studied the piezoelectric performance of CNT/cement concrete mixed with lead zirconate titanate (PZT) powders. It was found that the piezoelectric realization temperature can be decreased from 120°C to room temperature with small amount of CNT addition (0.3 wt.%). The highest piezoelectric strain factors ( $d_{33}$ ) with value of 62 pC/N and the highest piezoelectric voltage factors ( $g_{33}$ ) with value of  $60 \times 10^{-3}$  Vm/N can be obtained with 0.3 wt.% CNT and 70 wt.% PZT.

Other than piezoelectric performances, the thermoelectric performances of CNT/cement composites were also investigated recently. The Seebeck coefficient of the CNT/cement composites with 0.5 wt.% CNT addition reached the highest thermoelectric power of 23.5  $\mu$ V/K [63]. However, the temperature gradient between the two ends of the samples and the  $Z_t$  value of the samples were not presented, which means the applications and the efficiency of transferring are still very limited. Although a few studies have demonstrated the thermoelectric performance of the carbon fiber/cement composites [64, 65], the thermoelectric performance of the nanostructured carbon/cement composites is still in its infancy stage. The CNT/cement, CNF/cement, or GR/cement composites can be used as potential thermoelectric devices in the future applications.

#### 4. Summary and Future Trends

In this paper, the preparation methods of the nanostructured carbon/infrastructure materials composites, especially the dispersion methods of nanostructured carbon materials in the infrastructure materials matrix, were systematically reviewed. The high speed melt mixing, surface treatment, aqueous solution with surfactants, and sonication methods were presented to introduce the current preparation approaches. The surface treatment, aqueous solution with surfactants, and sonication methods were applied on the nanostructured carbon/cementitious materials composites,

while the high speed melt mixing method was widely used in nanostructured carbon/asphalt composites. It was found that using surfactants or acid surface treatment to the nanostructured carbon materials is positive for their dispersion in cementitious materials, but different surfactants have different dispersion efficiency. Unfortunately, it is too early to draw conclusions of which surfactant is better than others because there are many influence factors determining various requirements of the composites. Another important factor that governs the dispersion of the carbon nanostructured materials in cementitious materials is the sonication energy. However, the investigation on this part is still very limited and should be further studied in the future studies. In addition to CNT and CNF, the investigation of the GO dispersion in a cementitious material matrix is still in an infancy stage. Many problems have not been solved so far to demonstrate an effective way of GO or GR dispersion in a cementitious material matrix.

The nanostructured carbon/cementitious composites can be used as self-sensing composites due to their capability to reflect external force field change via their specific piezoresistivity performance. As a self-sensing composite, the sensitivity and stability of the composites are a top challenge in the future studies. How to obtain a composite which has high piezoelectric sensitivity and stable performances in repeated loading cycles still needs to be systematically investigated.

For the thermoelectric converting investigation, the temperature gradient between the two ends and the  $Z_t$  value of the composites were not systematically investigated. In addition, the investigations of the CNF/cement or GR/cement composites used as potential thermoelectric devices should be explored in the future investigations. For the piezoelectric constructions, the converting efficiency is the most important bottle neck problem that has to be solved before it can be widely applied in the fields.

#### Conflict of Interests

The authors declare that there is no conflict of interests regarding the publication of this paper.

#### Acknowledgments

This work was financially supported by the National Natural Science Foundation of China (51402074), the Lianyungang Scientific Plan-Industrial Program (CG1204), and the Six Talent Peaks Program of Jiangsu Province (ZBZZ-032).

#### References

- [1] M. J. Hanus and A. T. Harris, "Nanotechnology innovations for the construction industry," *Progress in Materials Science*, vol. 58, no. 7, pp. 1056–1102, 2013.
- [2] D. D. L. Chung, "Carbon materials for structural self-sensing, electromagnetic shielding and thermal interfacing," *Carbon*, vol. 50, no. 9, pp. 3342–3353, 2012.

- [3] S. J. Chen, F. G. Collins, A. J. N. Macleod, Z. Pan, W. H. Duan, and C. M. Wang, "Carbon nanotube-cement composites: a retrospect," *The IES Journal Part A: Civil & Structural Engineering*, vol. 4, no. 4, pp. 254–265, 2011.
- [4] Y. Liu and S. Kumar, "Polymer/carbon nanotube nano composite fibers-A review," *ACS Applied Materials & Interfaces*, vol. 6, no. 9, pp. 6069–6087, 2014.
- [5] L. S. Walker, V. R. Marotto, M. A. Rafiee, N. Koratkar, and E. L. Corral, "Toughening in graphene ceramic composites," *ACS Nano*, vol. 5, no. 4, pp. 3182–3190, 2011.
- [6] S. Parveen, S. Rana, and R. Fangueiro, "A review on nanomaterial dispersion, microstructure, and mechanical properties of carbon nanotube and nanofiber reinforced cementitious composites," *Journal of Nanomaterials*, vol. 2013, Article ID 710175, 19 pages, 2013.
- [7] S. J. Yan, S. L. Dai, X. Y. Zhang et al., "Investigating aluminum alloy reinforced by graphene nanoflakes," *Materials Science and Engineering: A*, vol. 612, pp. 440–444, 2014.
- [8] X. Yu and E. Kwon, "A carbon nanotube/cement composite with piezoresistive properties," *Smart Materials and Structures*, vol. 18, no. 5, Article ID 055010, 2009.
- [9] M. S. Konsta-Gdoutos, Z. S. Metaxa, and S. P. Shah, "Highly dispersed carbon nanotube reinforced cement based materials," *Cement and Concrete Research*, vol. 40, no. 7, pp. 1052–1059, 2010.
- [10] F. Babak, H. Abolfazl, R. Alimorad, and G. Parviz, "Preparation and mechanical properties of graphene oxide: cement nanocomposites," *The Scientific World Journal*, vol. 2014, Article ID 276323, 10 pages, 2014.
- [11] B. Han, X. Yu, and E. Kwon, "A self-sensing carbon nanotube/cement composite for traffic monitoring," *Nanotechnology*, vol. 20, no. 44, Article ID 445501, 2009.
- [12] J. Zuo, W. Yao, X. Liu, and J. Qin, "Sensing properties of carbon nanotube-carbon fiber/cement nanocomposites," *Journal of Testing and Evaluation*, vol. 40, no. 5, pp. 838–843, 2012.
- [13] H. Li, Q. Zhang, and H. Xiao, "Self-deicing road system with a CNFP high-efficiency thermal source and MWCNT/cement-based high-thermal conductive composites," *Cold Regions Science and Technology*, vol. 86, pp. 22–35, 2013.
- [14] L. I. Nasibulina, I. V. Anoshkin, A. G. Nasibulin, A. Cwirzen, V. Penttala, and E. I. Kauppinen, "Effect of carbon nanotube aqueous dispersion quality on mechanical properties of cement composite," *Journal of Nanomaterials*, vol. 2012, Article ID 169262, 6 pages, 2012.
- [15] R. K. Abu Al-Rub, B. M. Tyson, A. Yazdanbakhsh, and Z. Grasley, "Mechanical properties of nanocomposite cement incorporating surface-treated and untreated carbon nanotubes and carbon nanofibers," *Journal of Nanomechanics and Micromechanics*, vol. 2, no. 1, pp. 1–6, 2012.
- [16] F. Collins, J. Lambert, and W. H. Duan, "The influences of admixtures on the dispersion, workability, and strength of carbon nanotube-OPC paste mixtures," *Cement and Concrete Composites*, vol. 34, no. 2, pp. 201–207, 2012.
- [17] A. Sobolkina, V. Mechtcherine, V. Khavrus et al., "Dispersion of carbon nanotubes and its influence on the mechanical properties of the cement matrix," *Cement and Concrete Composites*, vol. 34, no. 10, pp. 1104–1113, 2012.
- [18] Z. S. Metaxa, M. S. Konsta-Gdoutos, and S. P. Shah, "Carbon nanofiber cementitious composites: effect of debulking procedure on dispersion and reinforcing efficiency," *Cement and Concrete Composites*, vol. 36, no. 1, pp. 25–32, 2013.
- [19] D. C. Marcano, D. V. Kosynkin, J. M. Berlin et al., "Improved synthesis of graphene oxide," *ACS Nano*, vol. 4, no. 8, pp. 4806–4814, 2010.
- [20] K. Gong, Z. Pan, A. H. Korayem et al., "Reinforcing effects of graphene oxide on portland cement paste," *Journal of Materials in Civil Engineering*, vol. 27, A4014010, no. 2, pp. 1–6, 2014.
- [21] A. A. Motlagh, A. Kiasat, E. Mirzaei, and F. O. Birgani, "Bitumen modification using carbon nanotubes," *World Applied Sciences Journal*, vol. 18, no. 4, pp. 594–599, 2012.
- [22] M. J. Khattak, A. Khattab, H. R. Rizvi, and P. Zhang, "The impact of carbon nano-fiber modification on asphalt binder rheology," *Construction and Building Materials*, vol. 30, pp. 257–264, 2012.
- [23] Z. Hasan, R. O. Kamran, F. Mohammad, G. Ahmad, and F. Hosein, "Evaluation of different conditions on the mixing bitumen and carbon nano-tubes," *International Journal of Civil & Environmental Engineering*, vol. 12, pp. 53–59, 2012.
- [24] E. Santagata, O. Baglieri, L. Tsantilis, and D. Dalmazzo, "Evaluation of self healing properties of bituminous binders taking into account steric hardening effects," *Construction and Building Materials*, vol. 41, pp. 60–67, 2013.
- [25] H. Yao, Z. You, L. Li et al., "Rheological properties and chemical analysis of nanoclay and carbon microfiber modified asphalt with Fourier transform infrared spectroscopy," *Construction and Building Materials*, vol. 38, pp. 327–337, 2013.
- [26] M. J. Khattak, A. Khattab, and H. R. Rizvi, "Characterization of carbon nano-fiber modified hot mix asphalt mixtures," *Construction and Building Materials*, vol. 40, pp. 738–745, 2013.
- [27] M. J. Khattak, A. Khattab, P. Zhang, H. R. Rizvi, and T. Pesacreta, "Microstructure and fracture morphology of carbon nano-fiber modified asphalt and hot mix asphalt mixtures," *Materials and Structures*, vol. 46, no. 12, pp. 2045–2057, 2013.
- [28] A. Yazdanbakhsh and Z. Grasley, "Utilization of silica fume to stabilize the dispersion of carbon nanofilaments in cement paste," *Journal of Materials in Civil Engineering*, vol. 26, no. 7, Article ID 06014010, 2014.
- [29] A. Chaipanich, T. Nochaiya, W. Wongkeo, and P. Torkitkul, "Compressive strength and microstructure of carbon nanotubes-fly ash cement composites," *Materials Science and Engineering A*, vol. 527, no. 4–5, pp. 1063–1067, 2010.
- [30] B. M. Tyson, R. K. Abu Al-Rub, A. Yazdanbakhsh, and Z. Grasley, "Carbon nanotubes and carbon nanofibers for enhancing the mechanical properties of nanocomposite cementitious materials," *Journal of Materials in Civil Engineering*, vol. 23, no. 7, pp. 1028–1035, 2011.
- [31] A. Yazdanbakhsh, Z. Grasley, B. Tyson, and R. Abu Al-Rub, "Challenges and benefits of utilizing carbon nanofilaments in cementitious materials," *Journal of Nanomaterials*, vol. 2012, Article ID 371927, 8 pages, 2012.
- [32] Z. S. Metaxa, J.-W. T. Seo, M. S. Konsta-Gdoutos, M. C. Hersam, and S. P. Shah, "Highly concentrated carbon nanotube admixture for nano-fiber reinforced cementitious materials," *Cement and Concrete Composites*, vol. 34, no. 5, pp. 612–617, 2012.
- [33] R. Siddique and A. Mehta, "Effect of carbon nanotubes on properties of cement mortars," *Construction and Building Materials*, vol. 50, pp. 116–129, 2014.
- [34] S. Kumar, P. Kolay, S. Malla, and S. Mishra, "Effect of multiwalled carbon nanotubes on mechanical strength of cement paste," *Journal of Materials in Civil Engineering*, vol. 24, no. 1, pp. 84–91, 2012.

- [35] Y. Hu, D. Luo, P. Li, Q. Li, and G. Sun, "Fracture toughness enhancement of cement paste with multi-walled carbon nanotubes," *Construction and Building Materials*, vol. 70, pp. 332–338, 2014.
- [36] J. N. Paula, J. M. Calixto, L. O. Ladeira et al., "Mechanical and rheological behavior of oil-well cement slurries produced with clinker containing carbon nanotubes," *Journal of Petroleum Science and Engineering*, vol. 122, pp. 274–279, 2014.
- [37] R. K. Abu Al-Rub, A. I. Ashour, and B. M. Tyson, "On the aspect ratio effect of multi-walled carbon nanotube reinforcements on the mechanical properties of cementitious nanocomposites," *Construction and Building Materials*, vol. 35, pp. 647–655, 2012.
- [38] B. Wang, T. Zhang, and Y. Han, "Reinforcement of surface-modified multi-walled carbon nanotubes on cement-based composites," *Advances in Cement Research*, vol. 26, no. 2, pp. 77–84, 2014.
- [39] H. Ziari, H. Farahani, A. Goli, and S. S. Galooyak, "The investigation of the impact of carbon nano tube on bitumen and HMA performance," *Petroleum Science and Technology*, vol. 32, no. 17, pp. 2102–2108, 2014.
- [40] E. Santagata, O. Baglieri, L. Tsantilis, and G. Chiappinelli, "Fatigue properties of bituminous binders reinforced with carbon nanotubes," *International Journal of Pavement Engineering*, vol. 16, no. 1, pp. 80–90, 2015.
- [41] S. Lv, Y. Ma, C. Qiu, T. Sun, J. Liu, and Q. Zhou, "Effect of graphene oxide nanosheets of microstructure and mechanical properties of cement composites," *Construction and Building Materials*, vol. 49, pp. 121–127, 2013.
- [42] F. Azhari and N. Banthia, "Cement-based sensors with carbon fibers and carbon nanotubes for piezoresistive sensing," *Cement and Concrete Composites*, vol. 34, no. 7, pp. 866–873, 2012.
- [43] B. Han, K. Zhang, X. Yu, E. Kwon, and J. Ou, "Electrical characteristics and pressure-sensitive response measurements of carboxyl MWNT/cement composites," *Cement and Concrete Composites*, vol. 34, no. 6, pp. 794–800, 2012.
- [44] B. Andrawes and L. Y. Chan, "Compression and tension stress-sensing of carbon nanotube-reinforced cement," *Magazine of Concrete Research*, vol. 64, no. 3, pp. 253–258, 2012.
- [45] A. L. Materazzi, F. Ubertini, and A. D'Alessandro, "Carbon nanotube cement-based transducers for dynamic sensing of strain," *Cement and Concrete Composites*, vol. 37, no. 1, pp. 2–11, 2013.
- [46] H. K. Kim, I. S. Park, and H. K. Lee, "Improved piezoresistive sensitivity and stability of CNT/cement mortar composites with low water-binder ratio," *Composite Structures*, vol. 116, pp. 713–719, 2014.
- [47] B. Han, X. Yu, and J. Ou, "Effect of water content on the piezoresistivity of MWNT/cement composites," *Journal of Materials Science*, vol. 45, no. 14, pp. 3714–3719, 2010.
- [48] B. Han, X. Yu, and J. Ou, "Multifunctional and smart carbon nanotube reinforced cement-based materials," in *Nanotechnology in Civil Infrastructure*, pp. 1–47, Springer, Berlin, Germany, 2011.
- [49] B. Han, K. Zhang, T. Burnham, E. Kwon, and X. Yu, "Integration and road tests of a self-sensing CNT concrete pavement system for traffic detection," *Smart Materials and Structures*, vol. 22, no. 1, Article ID 015020, 2013.
- [50] B. Han, K. Zhang, X. Yu, E. Kwon, and J. Ou, "Fabrication of Piezoresistive CNT/CNF Cementitious Composites with Superplasticizer as Dispersant," *Journal of Materials in Civil Engineering*, vol. 24, no. 6, pp. 658–665, 2012.
- [51] M. Saafi, K. Andrew, P. L. Tang et al., "Multifunctional properties of carbon nanotube/fly ash geopolymeric nanocomposites," *Construction and Building Materials*, vol. 49, pp. 46–55, 2013.
- [52] X. Shi, N. Xie, K. Fortune, and J. Gong, "Durability of steel reinforced concrete in chloride environments: an overview," *Construction and Building Materials*, vol. 30, pp. 125–138, 2012.
- [53] S. Yehia, C. Y. Tuan, D. Ferdon, and B. Chen, "Conductive concrete overlay for bridge deck deicing: mixture proportioning, optimization, and properties," *ACI Materials Journal*, vol. 97, no. 2, pp. 172–181, 2000.
- [54] T. Yang, Z. J. Yang, M. Singla, G. Song, and Q. Li, "Experimental study on carbon fiber tape-based deicing technology," *Journal of Cold Regions Engineering*, vol. 26, no. 2, pp. 55–70, 2012.
- [55] S. Wu, L. Mo, Z. Shui, and Z. Chen, "Investigation of the conductivity of asphalt concrete containing conductive fillers," *Carbon*, vol. 43, no. 7, pp. 1358–1363, 2005.
- [56] H. Zhao, Z. Wu, S. Wang, J. Zheng, and G. Che, "Concrete pavement deicing with carbon fiber heating wires," *Cold Regions Science and Technology*, vol. 65, no. 3, pp. 413–420, 2011.
- [57] X.-M. Zhou, Z. J. Yang, C. Chang, and G. Song, "Numerical assessment of electric roadway deicing system utilizing emerging carbon nanofiber paper," *Journal of Cold Regions Engineering*, vol. 26, no. 1, pp. 1–15, 2012.
- [58] H. Li, Q. Zhang, and H. Xiao, "Analytic investigations of CNFP-based self-deicing road system on the deicing performance," *Cold Regions Science and Technology*, vol. 103, pp. 123–132, 2014.
- [59] A. P. Singh, B. K. Gupta, M. Mishra, A. Chandra, R. B. Mathur, and S. K. Dhawan, "Multiwalled carbon nanotube/cement composites with exceptional electromagnetic interference shielding properties," *Carbon*, vol. 56, pp. 86–96, 2013.
- [60] B. Wang, Z. Guo, Y. Han, and T. Zhang, "Electromagnetic wave absorbing properties of multi-walled carbon nanotube/cement composites," *Construction and Building Materials*, vol. 46, pp. 98–103, 2013.
- [61] I. W. Nam, H. K. Kim, and H. K. Lee, "Influence of silica fume additions on electromagnetic interference shielding effectiveness of multi-walled carbon nanotube/cement composites," *Construction and Building Materials*, vol. 30, pp. 480–487, 2012.
- [62] H. Gong, Y. Zhang, J. Quan, and S. Che, "Preparation and properties of cement based piezoelectric composites modified by CNTs," *Current Applied Physics*, vol. 11, no. 3, pp. 653–656, 2011.
- [63] J. Zuo, W. Yao, and K. Wu, "Seebeck effect and mechanical properties of carbon nanotube-carbon fiber/cement nanocomposites," *Fullerenes, Nanotubes and Carbon Nanostructures*, vol. 23, no. 5, pp. 383–391, 2015.
- [64] J. Wei, L. Hao, G. He, and C. Yang, "Enhanced thermoelectric effect of carbon fiber reinforced cement composites by metallic oxide/cement interface," *Ceramics International*, vol. 40, no. 6, pp. 8261–8263, 2014.
- [65] J. Wei, Z. Nie, G. He, L. Hao, L. Zhao, and Q. Zhang, "Energy harvesting from solar irradiation in cities using the thermoelectric behavior of carbon fiber reinforced cement composites," *RSC Advances*, vol. 4, no. 89, pp. 48128–48134, 2014.

## Review Article

# A Review of the Application and Performance of Carbon Nanotubes in Fuel Cells

**Chong Luo, Hui Xie, Qin Wang, Geng Luo, and Chao Liu**

*Key Laboratory of Low-Grade Energy Utilization Technologies and Systems of Ministry of Education,  
College of Power Engineering, Chongqing University, Chongqing 400030, China*

Correspondence should be addressed to Hui Xie; [xiehui@cqu.edu.cn](mailto:xiehui@cqu.edu.cn)

Received 25 September 2014; Revised 17 April 2015; Accepted 20 April 2015

Academic Editor: Myoung-Woon Moon

Copyright © 2015 Chong Luo et al. This is an open access article distributed under the Creative Commons Attribution License, which permits unrestricted use, distribution, and reproduction in any medium, provided the original work is properly cited.

The fuel cell has the nature of high energy conversion efficiency and low pollutant emission. Carbon nanotubes used for fuel cells can decrease the needs of noble metals which are used for catalyst and improve the performance of fuel cells. The application of carbon nanotubes in fuel cells is summarized and discussed. The following aspects are described in this paper: the method used to reduce the platinum, the effect of carbon nanotubes on the fuel cell, improving the performance of fuel cell catalysts, the interaction between catalyst and carbon nanotube support, and the synthetic conditions of carbon nanotube supported catalyst. We summarize some of the results of previous studies and raise expectations for the microscopic state study of carbon nanotubes in the future.

## 1. Introduction

The fuel cell is a device which directly converts chemical energy into electrical energy. It has high energy conversion efficiency and low emissions [1–3]. Fuel cells are considered to be one of the promising methods to solve future energy crisis and environmental issues.

In recent years, in order to improve the efficiency of the fuel cell, a lot of studies are carried out from different ways.

In order to improve the efficiency of the fuel cell, the catalyst is needed. The noble metal Pt has the good catalytic efficiency. However, Pt is expensive, which is a huge obstacle for fuel cell to be commercialized [2, 3]. So we need to reduce the use of Pt and develop new catalysts improving the oxidation-reduction reaction (ORR) of the electrode [4].

The support of catalyst can help improve the capability of catalyst [5, 6]. Common catalyst support includes carbon, graphene, carbon nanotube (CNT), and other forms of carbon. Low content of platinum catalyst being thin film layer has been reported to be effective and provides a higher quality of Pt utilization and activity [7, 8]. Graphene nanosheet as an ideal alternative compared with the traditional carbon support materials has a high electrical activity of the catalyst and superior durability than the commercial Pt/C catalyst [9]. Furthermore, the support of iron-based catalyst is porous

carbon used in polymer electrolyte fuel cell, which can improve the fuel cell oxygen reducing ability. So the supports are really important for fuel cells. CNT as a support can effectively improve the catalyst performance and utilization [10]. Nowadays, the CNTs adopted in fuel cells are receiving wide attention.

This paper focuses on describing the study about the performance of CNTs and the latest advances in fuel cell applications.

## 2. CNT Used to Reduce the Using of Platinum

In order to reduce the amount of platinum and make sure the activity and stability of the catalyst at a high level, the following methods are mainly used. There is an example of proton exchange membrane fuel cell in Figure 1 [3], so that we can have a better understanding of fuel cell.

*2.1. Using the Support to Reduce the Use of Pt.* Jha et al. used proton exchange membrane fuel cell (PEMFC) structure to base on functionalized single-walled CNTs (SWCNT), making the Pt loading to reach  $0.06 \text{ mg Pt/m}^2$ , far below the  $0.125 \text{ mg Pt/m}^2$ —the United States Department of Energy 2017 loading of technical indicators about platinum group

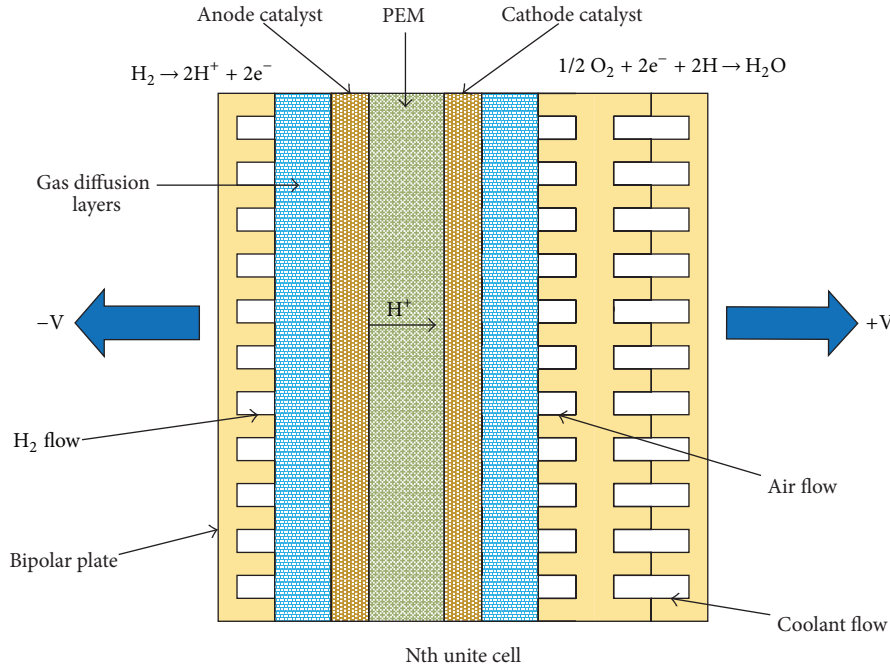


FIGURE 1: Fuel-cell components [3].

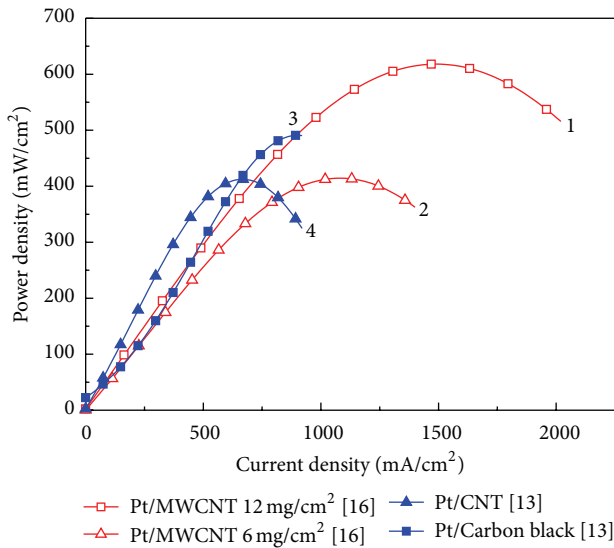


FIGURE 2: Current density based fuel cell performance curves.

metals (PGM) [11]. Girishkumar et al. found that the CNT as support for fuel cells rather than the support of carbon black for the Pt catalyst has a better catalyst activity and a higher current density [12]. Therefore, CNT can effectively reduce the use of Pt [13, 14]. So CNTs that are used as support can effectively improve the performance of the catalysts [15, 16].

In Figure 2, curves 1 and 2 are two catalysts in Hydrogen Fuel Cells. Pt/multiwalled CNTs (MWCNT) ( $12 \mu\text{g}/\text{cm}^2$ ) have a better power density [16]. As a result, in the same condition, having a higher Pt loading will get a better power density. Curves 3 and 4 are the performance of the Pt/Carbon Black

and Pt/CNT [13]. When the current is not too high, the power density of Pt/CNT electrode is much higher. In a word, we can get the different current density when we use different fuel cell, as their conversion efficiency is different. Therefore, the use of catalyst support has an important significance in the fuel cell applications.

**2.2. Exploring Pt-Containing Alloys as a Catalyst.** Catalysts composed by CNT as the support of Pt-Ru alloy have good dispersion and catalytic [17–19]. By comparing the Pt/MWCNTs, PtNi/MWCNTs, and PtRu/MWCNTs electrodes, the studies found PtRuNi/MWCNTs have better electrocatalytic activity [20]. When Au-CNT is used, phosphate buffer solution, isopropanol, and Nafion membrane can be mixed separately getting PdPtPt/Au-CNT, PtPdPd/Au-CNT, and PtPdPt/Au-CNT catalysts by the way of continuous precipitation. These catalysts are suitable for different environments and have good catalytic effect [21].

Just as the research of Wu et al., Pt-containing alloy as catalyst has a better performance than the commercial Pt/C catalyst in Figure 3 [22]. Besides, three Pt<sub>3</sub>Ni catalysts were more active than Pt. In this case, the alloy using as catalysts can be a good substitute for fuel cells.

In a word, it can be concluded that it is effective to improve catalysis performance by using Pt alloy or other metal alloys with CNT support [22–30]. In addition, it should be noted that the compound temperature of the alloy will effect the catalytic activity with the heat treatment [31].

**2.3. No Pt-Containing Catalysts.** In order to reduce the use of Pt, researchers attempt to use cheaper alternatives to achieve the same effect. Sheng et al. found that multiwalled CNTs as the support of Cu/Cu<sub>x</sub>O rather than Pt nanoparticles

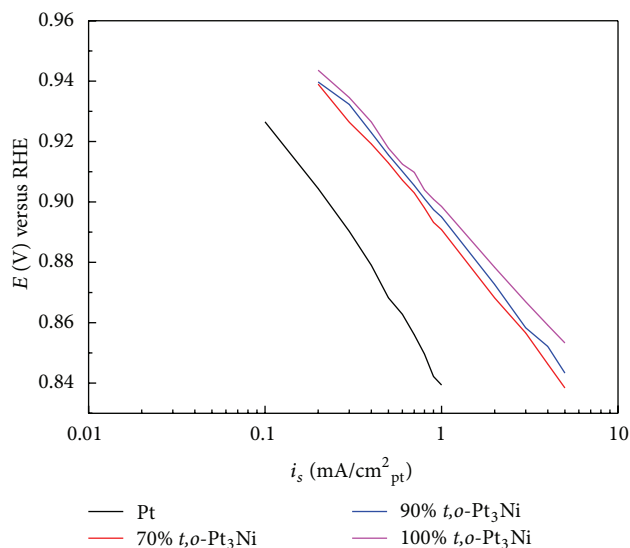


FIGURE 3: The performance of catalysts [22].

have higher catalytic activity [32]. Wang et al. found when polyelectrolyte functionalized carbon nanotubes can comprise the metal-free catalyst and are used to the oxidation-reduction reaction, it has a similar property to Pt catalyst in a fuel cell [33]. When PtRu/MWCNT and PtSn/MWCNT as anode catalyst, respectively, nonprecious cobalt-polypyrrole MWCNTs have the improved power density than no Pt based electrocatalysts as the cathode [34]. The electrode with Mo<sub>2</sub>C catalyst using the support of CNTs has a higher overvoltage than Pt-based electrode, and its activity may be further improved [35]. The nanocomposite of multiwalled CNTs and SnO<sub>2</sub>, constituting the anodes of microbial fuel cells in the electrode, has a larger maximum power density; therefore the nanocomposite of multiwalled CNTs and SnO<sub>2</sub> is a very desirable anode material [36]. The electrocatalytic activity of CNTs as the support of Mo<sub>2</sub>C (16.7 wt.% Mo) catalyst is equivalent to the Pt catalyst (20 wt.%) [37]. What is more, the catalyst is formed with Pd<sub>x</sub>Co-two metal alloy and multiwalled CNTs, which has the better activity. Moreover, Pd<sub>3</sub>Co/MWCNT (2.53 mW/cm<sup>2</sup>) has a better catalytic performance than Pd/MWCNT (1.64 mW/cm<sup>2</sup>) and Pt/C (1.20 mW/cm<sup>2</sup>) as the cathode applied in the fuel cell [38]. As is reported in the thesis of Lefèvre et al. [39], the current density of a cathode made with the best iron-based electrocatalyst can equal that of platinum-based cathode.

Therefore, compared to the platinum-containing catalyst, nonnoble metal catalysts with the CNT support for the electrode also have good catalytic effectivity [40, 41] and stability [42].

**2.4. Using of Pt Nanoparticles.** Ru-decorated Pt nanoparticles on Nitrogen-doped multiwalled CNTs used for directly methanol fuel cells have high performance and high dispersion [43]. On the one hand, the polymer composition of Pt nanoparticles loaded into the MWCNT shows higher electrocatalytic activity and better tolerance as the anode

of direct methanol fuel cell [44]. On the other hand, the shape and surface's morphology of CNTs has a profound impact on its electrocatalytic activity. When attached to the Pt nanoparticles, the electrical properties of flower-shaped nanostructure are significantly higher than conventional electro-catalytic properties of spherical nanoparticles [45].

So the use of Pt nanoparticles can well reflect the performance of the catalyst [46, 47], and Pt nanoparticles can be more dispersed on the surface of the support, thereby improving the utilization rate of platinum.

### 3. Effect of CNTs on Fuel Cell

Among the supports, CNT has a high surface area and high electrical conductivity, light weight, perfect hexagonal structure and many unusual mechanical, and electrical and chemical properties. In a silicon microfuel cell test, the PtRu graphitic carbon nanofibers, PtRu CNTs, and PtRu-Vulcan catalysts were used. The results obtained have shown that PtRu nanotubes have a maximum power density; PtRu-Vulcan has maximum durability [48]. Therefore CNTs are better able to improve the activity and get widespread attention. CNTs can improve the fuel cell performance, mainly in the following areas.

**3.1. Improving the Performance of the Catalyst.** The use of CNTs improves the performance of catalyst [49, 50]. Platinum can be fixed in the inner wall and the outer wall of CNTs and may constitute platinum-CNTs having good electrocatalytic properties [51]. The fuel cell using CNTs as a catalyst support has a larger current density [52]. And the fuel cell has a high performance, catalytic activity and the quality of transmission [53, 54]. In proton exchange membrane fuel cell, the surface of the bipolar plate is covered by conductive polymer coating (aluminum-coated). Adding the CNTs to polyaniline coating can enhance the conductive properties of the polyaniline polymer [55].

Therefore, while CNTs are of the catalyst support, the electrocatalytic properties of catalyst can be improved [52, 56, 57].

**3.2. Improving the Stability and Corrosion Resistance of the Catalyst.** CNTs can make the fuel cell more stable [58] and have higher corrosion resistance performance in work. CNT as catalyst support for fuel cells can reduce the formation of surface oxides and corrosion current as is shown in Figure 4 [59].

From Figure 4, Pt supported on MWCNT and Vulcan XC-72 has similar initial half wave potential. With time going on, MWCNT exhibits a much slower decrease rate than Vulcan XC-72 of the half wave potential [59].

Studies have shown that, in the fuel cell, the CNT as catalyst support is more stable than the carbon black XC-72, is more resistant to corrosion, and has a higher peak power density [50, 60]. The oxidized graphene catalyst supported on CNTs is coated on the melamine sponges as electrode prepared by the special method. And it can prove a large

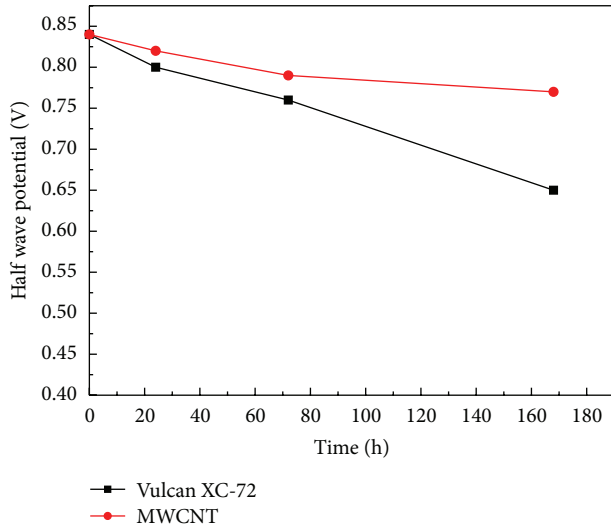


FIGURE 4: Comparison of half potential for ORR between Pt supported on Vulcan XC-72 and MWCNT as a function of oxidation treatment time.

conductive surface of microbial fuel cell for transferring electrons; compared to the conventional carbon-based anode and the metal group, it can have better durability and catalytic activity [61].

**3.3. Reducing the Cost of the Fuel Cell.** The CNT has a high surface area, good support for Pt, and high dispersion of the platinum, getting a smaller particle size [62]. So it can reduce the cost of production by reducing the use of platinum [63, 64].

### 3.4. Increasing Transmission Capacity

- (1) Electron transport capabilities: CNTs as electrode in solid acid fuel cell can improve the connection between platinum catalyst nanoparticles and current collector [65]. And multiwalled CNTs increase the anode surface area and the volume ratio, enhancing the ability of the anode electron transmission in microbial fuel cells [66].
- (2) Quality of transmission capacity: The mixture of multiwalled CNTs and single-walled CNTs used as Pt support can enhance the cathode quality activities and the mass transport in the catalyst layer, which can be a good method to ameliorate the mass transfer, when SWNT is used as catalyst support [67].

## 4. Improving the Performance of Catalysts by Using CNT

### 4.1. Optimization of Support

**4.1.1. Nitrogen-Containing Catalyst Support.** It can effectively improve the catalytic activity and stability, introducing the nitrogen functional group on the carbon support for

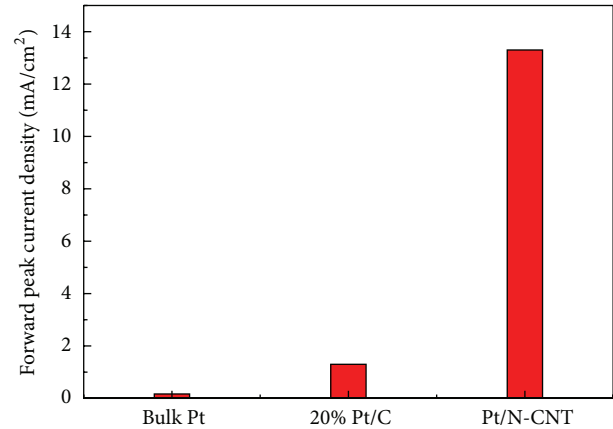


FIGURE 5: Peak current density for methanol oxidation on the various electrodes.

the catalyst [68–70]. Cheng et al. found PtRu nanoparticles are supported onto poly(diallyldimethylammonium chloride) (PDDA), polyethylenimine (PEI), 1-aminopyrene (AP), and tetrahydrofuran (THF) functionalized multiwalled CNTs. Pt-Ru nanoparticles supported on PEI, AP, and PDDA functionalized CNTs exhibited significantly much higher electrocatalytic activity and stability for the electro-oxidation of methanol as compared with PtRu supported on THF-CNTs [71]. Platinum supported on multiwalled CNTs doped with nitrogen, as the cathode catalyst, has a higher maximum power density ( $0.78 \text{ mW/cm}^2$ ) than commercial carbon supported Pt catalyst ( $0.72 \text{ mW/cm}^2$ ). When the oxidant is the actual gas, the use of the former has a significantly higher performance in direct methanol fuel cell [72]. Maiyalagan et al. [69] have done the experiment for nitrogen-containing catalyst support in Figure 5, which could testify the advantage of nitrogen-containing CNT.

### 4.1.2. Other Forms of Carbon Added

- (1) The fuel cell supported by the mixed electrode material of Graphene and multiwalled CNTs has a good catalytic effect [73]. Pham et al. got the unique layered graphene-CNT hybrid structures by a chemical vapor deposition method. Then they used the structures to support the Pt catalyst and found the catalyst for a fuel cell had superior polarization performance [74]. Therefore, adding graphene into the support can effectively improve the catalytic performance.
- (2) Carbon shells embedded carbon nanotubes can facilitate Pt nanoparticles dispersing on the core-shell nanostructural support and the carbon shell embedded carbon nanotube supported Pt catalyst will form a new catalyst, and this catalyst has a higher electrochemical activity surface area and mass activity than the Pt catalyst loading on the original CNTs [75].
- (3) CNTs and oxidized graphite form a three-dimensional carbon fiber composited material, just as

a sandwich, which gives a maximum PEMFC performance of 495 mW/cm<sup>2</sup> at 60°C temperature [76].

**4.1.3. Adding Substances to CNT to Synthesize the Support.** Adding new substances on the CNTs synthesizes new support to improve its performance; the researchers made a lot of attempts and exploration. Examples are listed below:

- (1) Sulfonated polyamide (PA-S) and sulfonation of polystyrene (PS-S) are two categories of mechanically robust and thermally stable nanocomposites, respectively, based on multiwalled CNT and silica nanotube (SiNT). Through solution blending, they were well dispersed and adhered on the nanostructures, forming a porous membrane structure for a fuel cell, which has high proton conductivity of 1.28–2.23 S/cm at 80°C and higher water retention capacity [77].
- (2) CNT is doped with heteroatoms forming a core-sheath nanostructure, which is attached to the CNTs forming the catalyst. Compared to Pt/C catalyst, it has higher durability. When used as the cathode catalyst, it exhibits very high current and power density [78].
- (3) The composed film using CNTs and polytetrafluoroethylene is located between the bipolar plate and the electrode. The contact resistance is reduced. Therefore, the proton-exchange membrane fuel cell output power is increased by about 1.6 times [79].

**4.1.4. Surface Treatment of CNTs.** Some substances were coated on the surface of CNTs to improve performance. The following examples show part of the studies:

- (1) By coating mesoporous polysulfone substrate on SWNTs forming a three-dimensional porous polysulfone-SWCNT, which is used as an anode in a microbial fuel cell, it has a high activity of surface region and the effective electron transfer in outer cells [80].
- (2) The surfactant was adsorbed on the surface of functionalized MWCNTs, where they prevented reaggregation of MWCNTs on the nanocomposite. Thereby enhancing the dispersion of nanocomposite materials, the prepared CNTs used in proton exchange membrane can enhance the thermal performance [81].

**4.2. Multimetal Addition of the Catalyst.** Studies have shown that the multiwalled CNTs are used as the support with Pd catalyst in anode, respectively, and Rh, Ru, Pt, Au, Ag, Pd, Ni, and Cu as the cathode catalyst for direct reduction of H<sub>2</sub>O<sub>2</sub>. The fuel cell maximum power density in descending order is Au > Ru > Pt > Ag > Rh > Pd > Ni > Cu [82]. Therefore, the use of various metals may have an impact on the catalytic activity [83]; we have a need to study the impact of the performance of various metals adding to the catalyst.

For example, Ni added to PtRu catalyst with the support of multiwalled CNTs can improve the electrochemical surface of the catalyst; meanwhile, comparing with the commercial

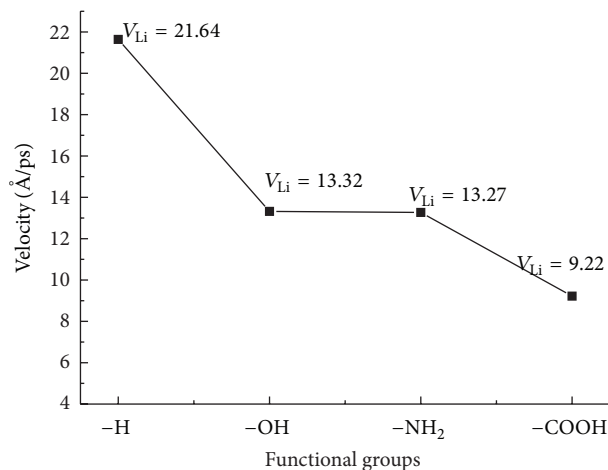


FIGURE 6: Effects of functional groups.

catalyst (20 wt.% PtRu/C), it has an effect in which the PtRu loading is reduced (10 wt.% PtRu) and a similar catalytic effect can be achieved [84]. Using CMK-3, ferrocene nickel as nickel source will be allowed to grow on CNTs, by chemical vapor deposition method. Through traditional wet impregnation method, we can get Pt catalyst. As a result, Pt particles get smaller, and they have a better performance under the conditions of a smaller Pt loading [85].

**4.3. Using Oriented CNTs.** Pt is supported on the oriented CNTs. In this way they form the catalyst, which has a good durability and reduces the loading amount of Pt; thereby we reduced the manufacturing costs. Using it in proton exchange membrane, fuel cell can have a higher energy density and current density [86]. Studies have shown that the oriented CNT film as cathode of the proton exchange membrane fuel cell can achieve a higher performance and a higher electrocatalytic activity than the disorder CNT membrane system of Pt/CNT [53]. Vertically aligned CNTs together with Pt forming the electrodes can be a good transfer of protons, electrons, and water. Catalyst layer and microporous layer have a good conduction for proton exchange membrane fuel cell, resulting in very good current density and reducing the use of Pt [87].

**4.4. Functionalization of CNTs.** While the port of CNT is functionalized, MWCNT-OH has a better power density than MWCNT-COOH [88]. The molecular dynamics simulation results also show that the functional groups on the port of the CNTs have a significant influence on the mass transporting through the port. As shown in Figure 6 [89], the speed of lithium-ion getting into the functionalized CNTs' port with hydroxy(-OH) is faster than with carboxyl(-COOH).

**4.5. The Use of Polymers.** Filling polyethylene terephthalate (PET) and polyvinylidene fluoride (PVDF) into CNTs, we can form a triple continuous structure. It can be applied to a proton exchange membrane fuel cell's bipolar plate, with excellent conductivity and strength [90]. Film, based

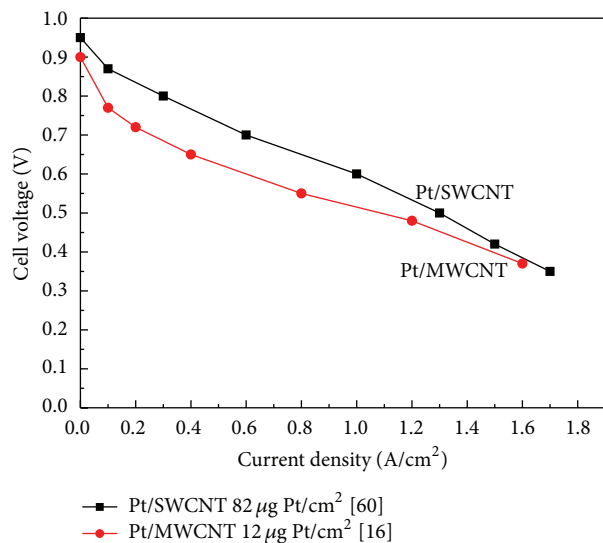


FIGURE 7: *I-V* characteristics of fuel cell with cathode.

on the polymer Nafion membrane adding some surfactant and working with functional multiwalled CNTs, makes CNTs have good dispersion. This nanocomposite is measured through thermogravimetric analysis (TGA), and results show that it lowers absorption of methanol and improves thermal stability [91].

## 5. Interaction between Catalyst and CNT Support

**5.1. The Catalyst Particles Are More Dispersed with CNT Support.** For example, CNT, used as a catalyst to support PtPd, can make PtPd nanoparticles distribute uniformly. CNT directly used in methanol fuel cell increases the activity of the electrochemical surface area and mass activity [92]. Therefore, it is important for carbon nanostructure as the support material and it can effectively disperse catalyst particles [93].

**5.2. CNT Diameter and Number of Layers.** When CNT-supported Pt nanoparticles are used for ORR, the specific surface area decreases with the diameter of the CNT increasing. When the diameter of CNT increases, the performance of Pt catalyst becomes more stable and the amount of Pt loading reduces [94]. Besides, multiwalled CNTs have better performance than single-walled CNTs [95]. As shown in Figure 7, the curves are the comparing cathode catalyst made of  $82 \mu\text{g Pt/cm}^2$  Pt/SWCNT and  $12 \mu\text{g Pt/cm}^2$  Pt/MWCNT, while other conditions do not have too much discrepancy. Even through Pt/SWCNT has a higher Pt loading, their cell voltages do not generate the great difference.

**5.3. Adhesion between the Pt Nanoparticles and Support.** He et al. studied how the size and the shape of Pt nanoparticles affect the catalytic performance. The results show that as the size of the Pt nanoparticles is larger, adhesive force becomes bigger regardless of the humidity. When the nanoparticles

are tetrahedral, it has good adhesion. But other shapes did not significantly impact the adhesion. When the humidity of Nafion membrane is increased, enhanced hydration leads to weakened adhesion. At the same time, controlling the content of the Nafion membrane can also improve the absorption [96].

## 6. The Synthetic Conditions of CNTs Catalyst

**6.1. In Supercritical Fluid.** If platinum CNTs are synthesized in supercritical fluids, they can be electrocatalyst for the low temperature fuel cells [97] or for the direct methanol fuel cell [98].

**6.2. The Application of Microwave Technology.** The CNTs can be manufactured through microwave-assisted reduction polyol method, and then platinum deposits on the CNTs to form the catalyst. The catalyst can be used in direct methanol fuel cells [99]. Chloroplatinic acid is used in providing Pt to synthesize platinum catalyst by the intermittent microwave radiation technology. This platinum catalyst has better performance than commercial platinum carbon black catalyst [100]. The vertically oriented CNT is synthesized using a microwave plasma enhanced chemical vapor deposition method. Then platinum nanoparticles are deposited on the CNT by DC sputtering system to form the catalyst. Increasing surface nitrogen content of this catalyst is expected to become the future fuel cell electrodes [101].

**6.3. Processing in Acid.** After CNTs are processed in acid, they can be used to manufacture the catalyst with platinum nanoparticles by chemical deposition method [102].

**6.4. Low-Temperature Plasma Method.** This method is widely used in the synthesis of CNTs and graphene material applied to the fuel cell, because it is possible to obtain many advantages like highly dispersed active substances, reducing energy requirements, enhancing the activation of the catalyst, shortening the synthetic time, reducing environmental pollution, and so on [103].

## 7. Summary and Outlook

Fuel cells have the nature of high energy conversion efficiency and low pollutant emission and are considered to be one of the promising methods to solve future energy crisis and environmental issues. Carbon nanotube used as the support of catalysis has an important significance in the fuel cell applications. We summarize and discuss the application of carbon nanotubes in fuel cells. We focus on the effect of carbon nanotubes on the fuel cell in which the ways are used to reduce the need of noble metal and to improve the performance of fuel cell catalysts, as well as the interaction with catalyst and carbon nanotube support and the synthesis conditions of carbon nanotube supported catalyst.

Researches about the support of CNTs and catalyst's performance have made a lot of achievements and make us much more clearly to understand the effects of the CNT

on fuel cell. However, the microscopic transport mechanism in CNTs remains to be further studied. The molecular dynamics simulation should be a powerful method to study the microscopic transmission in CNTs.

## Conflict of Interests

The authors declare that there is no conflict of interests regarding the publication of this paper.

## Acknowledgments

This work is supported by the Natural Science Foundation of Chongqing (Grant no. cstc2013cyjA90009), the National Natural Science Foundation of China (Grant no. 51206195), and the Fundamental Research Funds for the Central Universities of Ministry of Education of China (Grant no. CDJZR12110033).

## References

- [1] A. S. Aricò, S. Srinivasan, and V. Antonucci, "DMFCs: from fundamental aspects to technology development," *Fuel Cells*, vol. 1, no. 2, pp. 133–161, 2001.
- [2] F. T. Wagner, B. Lakshmanan, and M. F. Mathias, "Electrochemistry and the future of the automobile," *Journal of Physical Chemistry Letters*, vol. 1, no. 14, pp. 2204–2219, 2010.
- [3] M. K. Debe, "Electrocatalyst approaches and challenges for automotive fuel cells," *Nature*, vol. 486, no. 7401, pp. 43–51, 2012.
- [4] M. K. Debe, A. K. Schmoedel, G. D. Vernstrom, and R. Atanasoski, "High voltage stability of nanostructured thin film catalysts for PEM fuel cells," *Journal of Power Sources*, vol. 161, no. 2, pp. 1002–1011, 2006.
- [5] K. Wan, G. Long, M. Liu, L. Du, Z. Liang, and P. Tsiakaras, "Nitrogen-doped ordered mesoporous carbon: synthesis and active sites for electrocatalysis of oxygen reduction reaction," *Applied Catalysis B: Environmental*, vol. 165, pp. 566–571, 2015.
- [6] L. Zhao, Z. Wang, J. Li, J. Zhang, X. Sui, and L. Zhang, "A newly-designed sandwich-structured graphene-Pt-graphene catalyst with improved electrocatalytic performance for fuel cells," *Journal of Materials Chemistry A*, vol. 3, no. 10, pp. 5313–5320, 2015.
- [7] J.-H. Wee, K.-Y. Lee, and S. H. Kim, "Fabrication methods for low-Pt-loading electrocatalysts in proton exchange membrane fuel cell systems," *Journal of Power Sources*, vol. 165, no. 2, pp. 667–677, 2007.
- [8] E. Negro, R. Latsuzbaia, M. Dieci, I. Boshuizen, and G. J. Koper, "Pt electrodeposited over carbon nano-networks grown on carbon paper as durable catalyst for PEM fuel cells," *Applied Catalysis B: Environmental*, vol. 166–167, pp. 155–165, 2015.
- [9] J.-Y. Choi, D. Higgins, and Z. Chen, "Highly durable graphene nanosheet supported iron catalyst for oxygen reduction reaction in PEM fuel cells," *Journal of the Electrochemical Society*, vol. 159, no. 1, pp. B86–B89, 2012.
- [10] N. Rajalakshmi, H. Ryu, M. M. Shaijumon, and S. Ramaprabhu, "Performance of polymer electrolyte membrane fuel cells with carbon nanotubes as oxygen reduction catalyst support material," *Journal of Power Sources*, vol. 140, no. 2, pp. 250–257, 2005.
- [11] N. Jha, P. Ramesh, E. Bekyarova et al., "Functionalized single-walled carbon nanotube-based fuel cell benchmarked against US DOE 2017 technical targets," *Scientific Reports*, vol. 3, article 2257, 2013.
- [12] G. Girishkumar, M. Rettker, R. Underhile et al., "Single-wall carbon nanotube-based proton exchange membrane assembly for hydrogen fuel cells," *Langmuir*, vol. 21, no. 18, pp. 8487–8494, 2005.
- [13] T. Matsumoto, T. Komatsu, K. Arai et al., "Reduction of Pt usage in fuel cell electrocatalysts with carbon nanotube electrodes," *Chemical Communications*, vol. 10, no. 7, pp. 840–841, 2004.
- [14] X. Sun, R. Li, D. Villers, J. P. Dodelet, and S. Désilets, "Composite electrodes made of Pt nanoparticles deposited on carbon nanotubes grown on fuel cell backings," *Chemical Physics Letters*, vol. 379, no. 1–2, pp. 99–104, 2003.
- [15] H. Liu, C. Song, L. Zhang, J. Zhang, H. Wang, and D. P. Wilkinson, "A review of anode catalysis in the direct methanol fuel cell," *Journal of Power Sources*, vol. 155, no. 2, pp. 95–110, 2006.
- [16] J. M. Tang, K. Jensen, M. Waje et al., "High performance hydrogen fuel cells with ultralow Pt loading carbon nanotube thin film catalysts," *The Journal of Physical Chemistry C*, vol. 111, no. 48, pp. 17901–17904, 2007.
- [17] N. Jha, A. Leela Mohana Reddy, M. M. Shaijumon, N. Rajalakshmi, and S. Ramaprabhu, "Pt-Ru/multi-walled carbon nanotubes as electrocatalysts for direct methanol fuel cell," *International Journal of Hydrogen Energy*, vol. 33, no. 1, pp. 427–433, 2008.
- [18] L. Li and Y. C. Xing, "Pt-Ru nanoparticles supported on carbon nanotubes as methanol fuel cell catalysts," *Journal of Physical Chemistry C*, vol. 111, no. 6, pp. 2803–2808, 2007.
- [19] H. Wang, X. Wang, J. Zheng, F. Peng, and H. Yu, "Enhanced activity and durability of nanosized Pt-SnO<sub>2</sub>/IrO<sub>2</sub>/CNTs catalyst for methanol electrooxidation," *Journal of Nanoscience and Nanotechnology*, vol. 15, no. 5, pp. 3662–3669, 2015.
- [20] Y. Zhao, L. Fan, J. Ren, and B. Hong, "Electrodeposition of Pt-Ru and Pt-Ru-Ni nanoclusters on multi-walled carbon nanotubes for direct methanol fuel cell," *International Journal of Hydrogen Energy*, vol. 39, no. 9, pp. 4544–4557, 2014.
- [21] S. Saipanya, S. Lapanantnoppakhun, and T. Sarakonsri, "Electrochemical deposition of platinum and palladium on gold nanoparticles loaded carbon nanotube support for oxidation reactions in fuel cell," *Journal of Chemistry*, vol. 2014, Article ID 104514, 6 pages, 2014.
- [22] J. Wu, J. Zhang, Z. Peng, S. Yang, F. T. Wagner, and H. Yang, "Truncated octahedral Pt<sub>3</sub>Ni oxygen reduction reaction electrocatalysts," *Journal of the American Chemical Society*, vol. 132, no. 14, pp. 4984–4985, 2010.
- [23] V. R. Stamenkovic, B. Fowler, B. S. Mun et al., "Improved oxygen reduction activity on Pt<sub>3</sub>Ni(111) via increased surface site availability," *Science*, vol. 315, no. 5811, pp. 493–497, 2007.
- [24] V. R. Stamenkovic, B. S. Mun, M. Arenz et al., "Trends in electrocatalysis on extended and nanoscale Pt-bimetallic alloy surfaces," *Nature Materials*, vol. 6, no. 3, pp. 241–247, 2007.
- [25] B. Lim, M. Jiang, P. H. C. Camargo et al., "Pd-Pt bimetallic nanodendrites with high activity for oxygen reduction," *Science*, vol. 324, no. 5932, pp. 1302–1305, 2009.
- [26] K. D. Beard, D. Borrelli, A. M. Cramer, D. Blom, J. W. Van Zee, and J. R. Monnier, "Preparation and structural analysis of carbon-supported co core/pt shell electrocatalysts using electroless deposition methods," *ACS Nano*, vol. 3, no. 9, pp. 2841–2853, 2009.

- [27] C. Wang, H. Daimon, and S. Sun, "Dumbbell-like Pt-Fe<sub>3</sub>O<sub>4</sub> nanoparticles and their enhanced catalysis for oxygen reduction reaction," *Nano Letters*, vol. 9, no. 4, pp. 1493–1496, 2009.
- [28] K.-T. Jeng, C.-C. Chien, N.-Y. Hsu et al., "Performance of direct methanol fuel cell using carbon nanotube-supported Pt-Ru anode catalyst with controlled composition," *Journal of Power Sources*, vol. 160, no. 1, pp. 97–104, 2006.
- [29] N.-Y. Hsu, C.-C. Chien, and K.-T. Jeng, "Characterization and enhancement of carbon nanotube-supported PtRu electrocatalyst for direct methanol fuel cell applications," *Applied Catalysis B: Environmental*, vol. 84, no. 1-2, pp. 196–203, 2008.
- [30] J. Prabhuram, T. S. Zhao, Z. K. Tang, R. Chen, and Z. X. Liang, "Multiwalled carbon nanotube supported PtRu for the anode of direct methanol fuel cells," *The Journal of Physical Chemistry B*, vol. 110, no. 11, pp. 5245–5252, 2006.
- [31] B. N. Wanjala, R. Loukrakpam, J. Luo et al., "Thermal treatment of PtNiCo electrocatalysts: effects of nanoscale strain and structure on the activity and stability for the oxygen reduction reaction," *The Journal of Physical Chemistry C*, vol. 114, no. 41, pp. 17580–17590, 2010.
- [32] X. Sheng, B. Wouters, T. Breugelmans, A. Hubin, I. F. J. Vankelcom, and P. P. Pescarmona, "Cu/Cu<sub>2</sub>O and Pt nanoparticles supported on multi-walled carbon nanotubes as electrocatalysts for the reduction of nitrobenzene," *Applied Catalysis B: Environmental*, vol. 147, pp. 330–339, 2014.
- [33] S. Wang, D. Yu, and L. Dai, "Polyelectrolyte functionalized carbon nanotubes as efficient metal-free electrocatalysts for oxygen reduction," *Journal of the American Chemical Society*, vol. 133, no. 14, pp. 5182–5185, 2011.
- [34] A. L. Mohana Reddy, N. Rajalakshmi, and S. Ramaprabhu, "Cobalt-polypyrrole-multiwalled carbon nanotube catalysts for hydrogen and alcohol fuel cells," *Carbon*, vol. 46, no. 1, pp. 2–11, 2008.
- [35] T. Matsumoto, Y. Nagashima, T. Yamazaki, and J. Nakamura, "Fuel cell anode composed of Mo<sub>2</sub>C catalyst and carbon nanotube electrodes," *Electrochemical and Solid-State Letters*, vol. 9, no. 3, pp. A160–A162, 2006.
- [36] A. Mehdinia, E. Ziaei, and A. Jabbari, "Multi-walled carbon nanotube/SnO<sub>2</sub> nanocomposite: a novel anode material for microbial fuel cells," *Electrochimica Acta*, vol. 130, pp. 512–518, 2014.
- [37] Y. Wang, B. Li, D. Cui, X. Xiang, and W. Li, "Nano-molybdenum carbide/carbon nanotubes composite as bifunctional anode catalyst for high-performance Escherichia coli-based microbial fuel cell," *Biosensors & Bioelectronics*, vol. 51, pp. 349–355, 2014.
- [38] H. Gharibi, F. Golmohammadi, and M. Kheirmand, "Palladium/cobalt coated on multi-walled carbon nanotubes as an electro-catalyst for oxygen reduction reaction in passive direct methanol fuel cells," *Fuel Cells*, vol. 13, no. 6, pp. 987–1004, 2013.
- [39] M. Lefèvre, E. Proietti, F. Jaouen, and J. P. Dodelet, "Iron-Based catalysts with improved oxygen reduction activity in polymer electrolyte fuel cells," *Science*, vol. 324, no. 5923, pp. 71–74, 2009.
- [40] K. Gong, F. Du, Z. Xia, M. Durstock, and L. Dai, "Nitrogen-doped carbon nanotube arrays with high electrocatalytic activity for oxygen reduction," *Science*, vol. 323, no. 5915, pp. 760–764, 2009.
- [41] J. Zhao, Z. Liu, H. Li et al., "Development of a highly active electrocatalyst via ultrafine Pd nanoparticles dispersed on pristine graphene," *Langmuir*, vol. 31, no. 8, pp. 2576–2583, 2015.
- [42] C. Venkateswara Rao and Y. Ishikawa, "Activity, selectivity, and anion-exchange membrane fuel cell performance of virtually metal-free nitrogen-doped carbon nanotube electrodes for oxygen reduction reaction," *The Journal of Physical Chemistry C*, vol. 116, no. 6, pp. 4340–4346, 2012.
- [43] A.-C. Johansson, R. B. Yang, K. B. Haugshøj, J. V. Larsen, L. H. Christensen, and E. V. Thomsen, "Ru-decorated Pt nanoparticles on N-doped multi-walled carbon nanotubes by atomic layer deposition for direct methanol fuel cells," *International Journal of Hydrogen Energy*, vol. 38, no. 26, pp. 11406–11414, 2013.
- [44] Y. Mu, H. Liang, J. Hu, L. Jiang, and L. Wan, "Controllable Pt nanoparticle deposition on carbon nanotubes as an anode catalyst for direct methanol fuel cells," *The Journal of Physical Chemistry B*, vol. 109, no. 47, pp. 22212–22216, 2005.
- [45] S. Ghosh and C. R. Raj, "Facile in situ synthesis of multiwall carbon nanotube supported flowerlike Pt nanostructures: an efficient electrocatalyst for fuel cell application," *The Journal of Physical Chemistry C*, vol. 114, no. 24, pp. 10843–10849, 2010.
- [46] S. Y. Wang, S. P. Jiang, T. J. White, J. Guo, and X. Wang, "Electrocatalytic activity and interconnectivity of Pt nanoparticles on multiwalled carbon nanotubes for fuel cells," *Journal of Physical Chemistry C*, vol. 113, no. 43, pp. 18935–18945, 2009.
- [47] T. S. Miller, S. Sansuk, S. Pei E, S. C. Lai, J. V. Macpherson, and P. R. Unwin, "Pt nanoparticle modified single walled carbon nanotube network electrodes for electrocatalysis: control of the specific surface area over three orders of magnitude," *Catalysis Today*, vol. 244, pp. 136–145, 2015.
- [48] M. Borghei, G. Scotti, P. Kanninen et al., "Enhanced performance of a silicon microfabricated direct methanol fuel cell with PtRu catalysts supported on few-walled carbon nanotubes," *Energy*, vol. 65, pp. 612–620, 2014.
- [49] K. Lee, J. Zhang, H. Wang, and D. P. Wilkinson, "Progress in the synthesis of carbon nanotube- and nanofiber-supported Pt electrocatalysts for PEM fuel cell catalysis," *Journal of Applied Electrochemistry*, vol. 36, no. 5, pp. 507–522, 2006.
- [50] F. Hasché, M. Oezaslan, and P. Strasser, "Activity, stability and degradation of multi walled carbon nanotube (MWCNT) supported Pt fuel cell electrocatalysts," *Physical Chemistry Chemical Physics*, vol. 12, no. 46, pp. 15251–15258, 2010.
- [51] Z. Wen, Q. Wang, and J. Li, "Template synthesis of aligned carbon nanotube arrays using glucose as a carbon source: Pt decoration of inner and outer nanotube surfaces for fuel-cell catalysts," *Advanced Functional Materials*, vol. 18, no. 6, pp. 959–964, 2008.
- [52] T. Yoshitake, Y. Shimakawa, S. Kuroshima et al., "Preparation of fine platinum catalyst supported on single-wall carbon nanohorns for fuel cell application," *Physica B: Condensed Matter*, vol. 323, no. 1–4, pp. 124–126, 2002.
- [53] W. Li, X. Wang, Z. Chen, M. Waje, and Y. Yan, "Carbon nanotube film by filtration as cathode catalyst support for proton-exchange membrane fuel cell," *Langmuir*, vol. 21, no. 21, pp. 9386–9389, 2005.
- [54] J. E. Mink and M. M. Hussain, "Sustainable design of high-performance micro-sized microbial fuel cell with carbon nanotube anode and air cathode," *ACS Nano*, vol. 7, no. 8, pp. 6921–6927, 2013.
- [55] M. A. Deyab, "Corrosion protection of aluminum bipolar plates with polyaniline coating containing carbon nanotubes in acidic medium inside the polymer electrolyte membrane fuel cell," *Journal of Power Sources*, vol. 268, pp. 50–55, 2014.
- [56] W. Li, C. Liang, W. Zhou et al., "Preparation and characterization of multiwalled carbon nanotube-supported platinum for cathode catalysts of direct methanol fuel cells," *The Journal of Physical Chemistry B*, vol. 107, no. 26, pp. 6292–6299, 2003.

- [57] H. Tang, J. H. Chen, Z. P. Huang et al., "High dispersion and electrocatalytic properties of platinum on well-aligned carbon nanotube arrays," *Carbon*, vol. 42, no. 1, pp. 191–197, 2004.
- [58] W. Zhang, P. Sherrell, A. I. Minett, J. M. Razal, and J. Chen, "Carbon nanotube architectures as catalyst supports for proton exchange membrane fuel cells," *Energy & Environmental Science*, vol. 3, no. 9, pp. 1286–1293, 2010.
- [59] X. Wang, W. Li, Z. Chen, M. Waje, and Y. Yan, "Durability investigation of carbon nanotube as catalyst support for proton exchange membrane fuel cell," *Journal of Power Sources*, vol. 158, no. 1, pp. 154–159, 2006.
- [60] J. M. Tang, K. Jensen, W. Li et al., "Carbon nanotube free-standing membrane of Pt/SWNTs as catalyst layer in hydrogen fuel cells," *Australian Journal of Chemistry*, vol. 60, no. 7, pp. 528–532, 2007.
- [61] H.-T. Chou, H. Lee, C. Lee, N. Tai, and H. Chang, "Highly durable anodes of microbial fuel cells using a reduced graphene oxide/carbon nanotube-coated scaffold," *Bioresource Technology*, vol. 169, pp. 532–536, 2014.
- [62] T. Matsumoto, T. Komatsu, H. Nakano et al., "Efficient usage of highly dispersed Pt on carbon nanotubes for electrode catalysts of polymer electrolyte fuel cells," *Catalysis Today*, vol. 90, no. 3–4, pp. 277–281, 2004.
- [63] C. Wang, M. Waje, X. Wang, J. M. Tang, R. C. Haddon, and Y. Yan, "Proton exchange membrane fuel cells with carbon nanotube based electrodes," *Nano Letters*, vol. 4, no. 2, pp. 345–348, 2004.
- [64] G. Girishkumar, K. Vinodgopal, and P. V. Kamat, "Carbon nanostructures in portable fuel cells: single-walled carbon nanotube electrodes for methanol oxidation and oxygen reduction," *The Journal of Physical Chemistry B*, vol. 108, no. 52, pp. 19960–19966, 2004.
- [65] Á. Varga, M. Pfohl, N. A. Brunelli, M. Schreier, K. P. Giapis, and S. M. Haile, "Carbon nanotubes as electronic interconnects in solid acid fuel cell electrodes," *Physical Chemistry Chemical Physics*, vol. 15, no. 37, pp. 15470–15476, 2013.
- [66] J. E. Mink, J. P. Rojas, B. E. Logan, and M. M. Hussain, "Vertically grown multiwalled carbon nanotube anode and nickel silicide integrated high performance micro-sized (1.25  $\mu\text{m}$ ) microbial fuel cell," *Nano Letters*, vol. 12, no. 2, pp. 791–795, 2012.
- [67] P. Ramesh, M. E. Itkis, J. M. Tang, and R. C. Haddon, "SWNT-MWNT hybrid architecture for proton exchange membrane fuel cell cathodes," *The Journal of Physical Chemistry C*, vol. 112, no. 24, pp. 9089–9094, 2008.
- [68] Y. Zhou, K. Neyerlin, T. S. Olson et al., "Enhancement of Pt and Pt-alloy fuel cell catalyst activity and durability via nitrogen-modified carbon supports," *Energy & Environmental Science*, vol. 3, no. 10, pp. 1437–1446, 2010.
- [69] T. Maiyalagan, B. Viswanathan, and U. V. Varadaraju, "Nitrogen containing carbon nanotubes as supports for Pt—alternate anodes for fuel cell applications," *Electrochemistry Communications*, vol. 7, no. 9, pp. 905–912, 2005.
- [70] Z. Chen, D. Higgins, H. Tao, and R. S. Hsu, "Highly active nitrogen-doped carbon nanotubes for oxygen reduction reaction in fuel cell applications," *The Journal of Physical Chemistry C*, vol. 113, no. 49, pp. 21008–21013, 2009.
- [71] Y. Cheng, C. Xu, P. K. Shen, and S. P. Jiang, "Effect of nitrogen-containing functionalization on the electrocatalytic activity of PtRu nanoparticles supported on carbon nanotubes for direct methanol fuel cells," *Applied Catalysis B: Environmental*, vol. 158–159, pp. 140–149, 2014.
- [72] P. Kanninen, M. Borghei, O. Sorsa et al., "Highly efficient cathode catalyst layer based on nitrogen-doped carbon nanotubes for the alkaline direct methanol fuel cell," *Applied Catalysis B: Environmental*, vol. 156–157, pp. 341–349, 2014.
- [73] N. Jha, R. I. Jafri, N. Rajalakshmi, and S. Ramaprabhu, "Graphene-multi walled carbon nanotube hybrid electrocatalyst support material for direct methanol fuel cell," *International Journal of Hydrogen Energy*, vol. 36, no. 12, pp. 7284–7290, 2011.
- [74] K. Pham, D. H. Chua, D. S. McPhail, and A. T. Wee, "The direct growth of graphene-carbon nanotube hybrids as catalyst support for high-performance PEM fuel cells," *ECS Electrochemistry Letters*, vol. 3, no. 6, pp. F37–F40, 2014.
- [75] H. G. Li, X. Zhang, D. He, T. Peng, and S. Mu, "Carbon-embedded carbon nanotubes as supports of polymer electrolyte membrane fuel cell catalysts," *Journal of Nanoscience and Nanotechnology*, vol. 14, no. 9, pp. 6929–6933, 2014.
- [76] M. Sahoo, B. P. Vinayan, and S. Ramaprabhu, "Platinum-decorated chemically modified reduced graphene oxide—multi-walled carbon nanotube sandwich composite as cathode catalyst for a proton exchange membrane fuel cell," *RSC Advances*, vol. 4, no. 50, pp. 26140–26148, 2014.
- [77] A. Kausar, A. Hussain, M. Y. Khan, and M. Siddiq, "Fuel cell membranes prepared from multi-walled carbon nanotubes and silica nanotubes-filled sulfonated polyamide/sulfonated polystyrene porous blend films," *Journal of Plastic Film & Sheeting*, vol. 30, no. 3, pp. 314–336, 2014.
- [78] Y. J. Sa, C. Park, H. Y. Jeong et al., "Carbon nanotubes/heteroatom-doped carbon core-sheath nanostructures as highly active, metal-free oxygen reduction electrocatalysts for alkaline fuel cells," *Angewandte Chemie International Edition*, vol. 53, no. 16, pp. 4102–4106, 2014.
- [79] Y. Show and K. Takahashi, "Stainless steel bipolar plate coated with carbon nanotube (CNT)/polytetrafluoroethylene (PTFE) composite film for proton exchange membrane fuel cell (PEMFC)," *Journal of Power Sources*, vol. 190, no. 2, pp. 322–325, 2009.
- [80] T.-H. Nguyen, Y.-Y. Yu, X. Wang, J.-Y. Wang, and H. Song, "A 3D mesoporous polysulfone-carbon nanotube anode for enhanced bioelectricity output in microbial fuel cells," *Chemical Communications*, vol. 49, no. 91, pp. 10754–10756, 2013.
- [81] A. Sayeed, Y. H. Kim, Y. Park, A. I. Gopalan, K.-P. Lee, and S.-J. Choi, "Non-covalent bonding interaction of surfactants with functionalized carbon nanotubes in proton exchange membranes for fuel cell applications," *Journal of Nanoscience and Nanotechnology*, vol. 13, no. 11, pp. 7424–7429, 2013.
- [82] T. H. Oh, B. Jang, and S. Kwon, "Electrocatalysts supported on multiwalled carbon nanotubes for direct borohydride-hydrogen peroxide fuel cell," *International Journal of Hydrogen Energy*, vol. 39, no. 13, pp. 6977–6986, 2014.
- [83] W. M. Daoush and T. Imae, "Fabrication of PtNi bimetallic nanoparticles supported on multi-walled carbon nanotubes," *Journal of Experimental Nanoscience*, vol. 10, no. 5, pp. 392–406, 2015.
- [84] A. M. Valenzuela-Muñiz, G. Alonso-Nuñez, G. G. Botte, M. Miki-Yoshida, and Y. Verde-Gómez, "Influence of nickel on the electrochemical activity of PtRu/multiwalled carbon nanotubes electrocatalysts for direct methanol fuel cells," *Journal of Applied Electrochemistry*, vol. 44, no. 6, pp. 695–700, 2014.
- [85] L. Samiee, F. Shoghi, and A. Maghsodi, "In situ functionalisation of mesoporous carbon electrodes with carbon nanotubes for proton exchange membrane fuel-cell application," *Materials Chemistry and Physics*, vol. 143, no. 3, pp. 1228–1235, 2014.

- [86] J. B. Liu, Y. Yuan, and S. Bashir, "Functionalization of aligned carbon nanotubes to enhance the performance of fuel cell," *Energies*, vol. 6, no. 12, pp. 6476–6486, 2013.
- [87] S. Murata, M. Imanishi, S. Hasegawa, and R. Namba, "Vertically aligned carbon nanotube electrodes for high current density operating proton exchange membrane fuel cells," *Journal of Power Sources*, vol. 253, pp. 104–113, 2014.
- [88] N. Thepsuparungsikul, T. C. Ng, O. Lefebvre, and H. Y. Ng, "Different types of carbon nanotube-based anodes to improve microbial fuel cell performance," *Water Science and Technology*, vol. 69, no. 9, pp. 1900–1910, 2014.
- [89] Y. Cheng-Bing, X. Hui, and L. Chao, "Molecular dynamics simulation of average velocity of lithium ion across the end of carbon nanotube," *Acta Physica Sinica*, vol. 63, no. 20, Article ID 200508, 2014.
- [90] M. Wu and L. L. Shaw, "A novel concept of carbon-filled polymer blends for applications in PEM fuel cell bipolar plates," *International Journal of Hydrogen Energy*, vol. 30, no. 4, pp. 373–380, 2005.
- [91] Y. H. Kim, A. Sayeed, Y. Park, A. I. Gopalan, K.-P. Lee, and S.-J. Choi, "Functionalized carbon nanotubes reinforced polymer electrolyte membranes prepared by surfactant-assisted casting for fuel cell applications," *Journal of Nanoelectronics and Optoelectronics*, vol. 8, no. 6, pp. 551–556, 2013.
- [92] H. L. Wang, B. A. Kakade, T. Tamaki, and T. Yamaguchi, "Synthesis of 3D graphite oxide-exfoliated carbon nanotube carbon composite and its application as catalyst support for fuel cells," *Journal of Power Sources*, vol. 260, pp. 338–348, 2014.
- [93] G. Girishkumar, T. D. Hall, K. Vinodgopal, and P. V. Kamat, "Single wall carbon nanotube supports for portable direct methanol fuel cells," *Journal of Physical Chemistry B*, vol. 110, no. 1, pp. 107–114, 2006.
- [94] A. O. Al-Youbi, J. L. Gómez de la Fuente, F. J. Pérez-Alonso et al., "Effects of multiwalled carbon nanotube morphology on the synthesis and electrocatalytic performance of Pt supported by multiwalled carbon nanotubes," *Applied Catalysis B: Environmental*, vol. 150–151, pp. 21–29, 2014.
- [95] M. Carmo, V. A. Paganin, J. M. Rosolen, and E. R. Gonzalez, "Alternative supports for the preparation of catalysts for low-temperature fuel cells: the use of carbon nanotubes," *Journal of Power Sources*, vol. 142, no. 1–2, pp. 169–176, 2005.
- [96] Q. He, D. C. Joy, and D. J. Keffer, "Nanoparticle adhesion in proton exchange membrane fuel cell electrodes," *Journal of Power Sources*, vol. 241, pp. 634–646, 2013.
- [97] Y. Lin, X. Cui, C. Yen, and C. M. Wai, "Platinum/carbon nanotube nanocomposite synthesized in supercritical fluid as electrocatalysts for low-temperature fuel cells," *The Journal of Physical Chemistry B*, vol. 109, no. 30, pp. 14410–14415, 2005.
- [98] Y. Lin, X. Cui, C. H. Yen, and C. M. Wai, "PtRu/carbon nanotube nanocomposite synthesized in supercritical fluid: a novel electrocatalyst for direct methanol fuel cells," *Langmuir*, vol. 21, no. 24, pp. 11474–11479, 2005.
- [99] M. Sakthivel, A. Schlange, U. Kunz, and T. Turek, "Microwave assisted synthesis of surfactant stabilized platinum/carbon nanotube electrocatalysts for direct methanol fuel cell applications," *Journal of Power Sources*, vol. 195, no. 20, pp. 7083–7089, 2010.
- [100] Z. Q. Tian, S. P. Jiang, Y. M. Liang, and P. K. Shen, "Synthesis and characterization of platinum catalysts on multiwalled carbon nanotubes by intermittent microwave irradiation for fuel cell applications," *Journal of Physical Chemistry B*, vol. 110, no. 11, pp. 5343–5350, 2006.
- [101] N. Soin, S. S. Roy, L. Karlsson, and J. A. McLaughlin, "Sputter deposition of highly dispersed platinum nanoparticles on carbon nanotube arrays for fuel cell electrode material," *Diamond and Related Materials*, vol. 19, no. 5–6, pp. 595–598, 2010.
- [102] Z. Liu, X. Lin, J. Y. Lee, W. Zhang, M. Han, and L. M. Gan, "Preparation and characterization of platinum-based electrocatalysts on multiwalled carbon nanotubes for proton exchange membrane fuel cells," *Langmuir*, vol. 18, no. 10, pp. 4054–4060, 2002.
- [103] Q. Wang, X. Wang, Z. Chai, and W. Hu, "Low-temperature plasma synthesis of carbon nanotubes and graphene based materials and their fuel cell applications," *Chemical Society Reviews*, vol. 42, no. 23, pp. 8821–8834, 2013.

## Research Article

# N-Type Conductive Ultrananocrystalline Diamond Films Grown by Hot Filament CVD

Michael Mertens, Markus Mohr, Neda Wiora, Kai Brühne, and Hans-Jörg Fecht

*Institute of Micro and Nanomaterials, Ulm University, 89081 Ulm, Germany*

Correspondence should be addressed to Michael Mertens; michael.mertens@uni-ulm.de and Markus Mohr; markus.mohr@uni-ulm.de

Received 24 September 2014; Revised 20 January 2015; Accepted 12 February 2015

Academic Editor: Aiyang Wang

Copyright © 2015 Michael Mertens et al. This is an open access article distributed under the Creative Commons Attribution License, which permits unrestricted use, distribution, and reproduction in any medium, provided the original work is properly cited.

We present the synthesis of ultrananocrystalline diamond (UNCD) films by application of hot filament chemical vapor deposition (HFCVD). We furthermore studied the different morphological, structural, and electrical properties. The grown films are fine grained with grain sizes between 4 and 7 nm. The UNCD films exhibit different electrical conductivities, dependent on grain boundary structure. We present different contact metallizations exhibiting ohmic contact behavior and good adhesion to the UNCD surface. The temperature dependence of the electrical conductivity is presented between  $-200$  and  $900^{\circ}\text{C}$ . We furthermore present spectroscopic investigations of the films, supporting that the origin of the conductivity is the structure and volume of the grain boundary.

## 1. Introduction

Electronic and microelectromechanic sensor devices built from diamond have already been demonstrated [1–4]. However, one of the main obstacles to make use of diamond as a material for electronic applications is the difficulty of doping diamond [5]. Diamond can be p-doped by boron, even though the acceptor level of boron is 0.37 eV over the valence band [6] and is therefore not activated at room temperature. By increasing the doping level, the activation energy decreases, so that p-doped diamond can be thermally activated at room temperature [7]. In contrast to that, no shallow donors were found for diamond [5].

An interesting, novel kind of n-type conductivity, present at room temperature, which could fill this gap, was found in ultrananocrystalline diamond films [8–10]. The addition of nitrogen (which has activation energy of 1.7 eV, if incorporated substitutionally [5]) can lead in ultrananocrystalline diamond films to a high electrical conductivity at room temperature [8–10]. In [11] it was shown that the incorporation of nitrogen in grain boundaries leads to additional localized states within the band gap. Birrell et al. [12] have produced similar films by plasma CVD and conclude that the addition of nitrogen does lead to an increased width of a  $sp^2$ -carbon

grain boundary phase. In contrast to our findings [10], they reach an increasing conductivity for an increased addition of nitrogen [12].

Investigations of Ikeda et al. [13], who also used plasma CVD for deposition of UNCD films with nitrogen addition, show that the increase of ordering and amount of a  $sp^2$ -carbon grain boundary phase is more responsible for an increasing conduction than the concentration of incorporated nitrogen.

In contrast to most of the published work on conductive UNCD films, where the films are mostly grown by plasma CVD, we present the growth of UNCD films by hot filament chemical vapor deposition (HFCVD).

We show that, by increase of substrate temperature, a strong change in morphology and an increase of electrical conductivity of the films take place.

## 2. Experiments

The UNCD films were grown by using the hot filament chemical vapor deposition (HFCVD) technique.

This highly flexible and scalable technique allows growing diamond films on different substrates like silicon, quartz, and

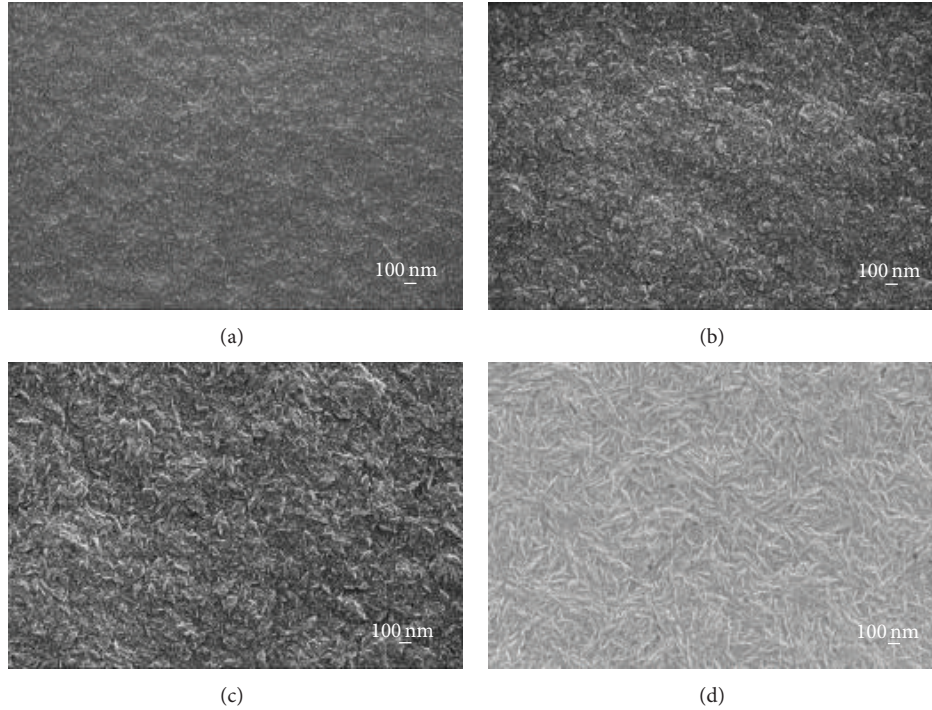


FIGURE 1: Influence of the substrate temperature on the morphology of the UNCD films is shown in the SEM pictures (a) ca. 570°C, (b) and (c) 580°C–630°C, and (d) ca. 750°C.

carbide forming metals. Also coating of structured and three dimensional substrates is possible [1].

Before growth, the substrates were pretreated by ultrasonication in a nanodiamond solution. By this treatment, small seed crystals are deposited on the substrate with a density in the order of  $10^{11} \text{ cm}^{-2}$  [2]. This procedure, in contrast to bias enhanced nucleation, opens the possibility to grow diamond on some nonconductive substrates [2].

We used tungsten filaments that were electrically heated up to about 2000°C. The used gas, maintained during growth, was a methane/hydrogen mixture (5%  $\text{CH}_4/\text{H}_2$ ). Additionally we introduced different amounts of ammonia (between 0.35% and 3.5%  $\text{NH}_3/\text{H}_2$ ). We investigate the influence of extra gas addition (ammonia) on the electrical conductivity of the grown films. The influence of ammonia addition on the morphology was already shown in [10].

Conductive UNCD films were grown on 3 inches,  $\langle 100 \rangle$  silicon wafer with a 300 nm silicon oxide layer deposited by PECVD for an electrical insulation between the substrate and the conductive film. Due to the high seeding density, a closed film is achieved after a few minutes and the silicon oxide is exposed to atomic hydrogen for only short time.

Figure 1 shows microstructures of different UNCD films grown with different substrate temperatures. The substrate temperature can be influenced indirectly by different filament currents and by the distance of substrate to filament or directly by using a sample holder at a cooling and heating system.

Different substrate temperatures are leading to completely different microstructures. Figure 1(a) presents a very

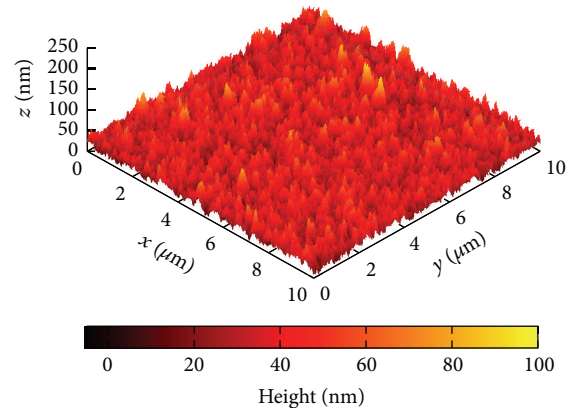


FIGURE 2: AFM measurement of 1  $\mu\text{m}$  thick UNCD film on silicon substrate (compare SEM in Figure 1(a)).

homogeneous microstructure, grown at a substrate temperature of about 570°C. With increasing substrate temperature, from 580°C to 630°C, like exemplarily shown in Figures 1(b) and 1(c), more and more cluster-like structures are visible in the microstructure. Above about 700°C substrate temperature the diamond microstructure changes completely to another structure, which is shown in Figure 1(d).

The surface roughness measured by atomic force microscopy (AFM) for all grown films is about 10 nm (RMS). A representative measurement is shown in Figure 2.

X-ray diffraction (XRD) measurements were performed, proving that the film consists of crystalline diamond grains.

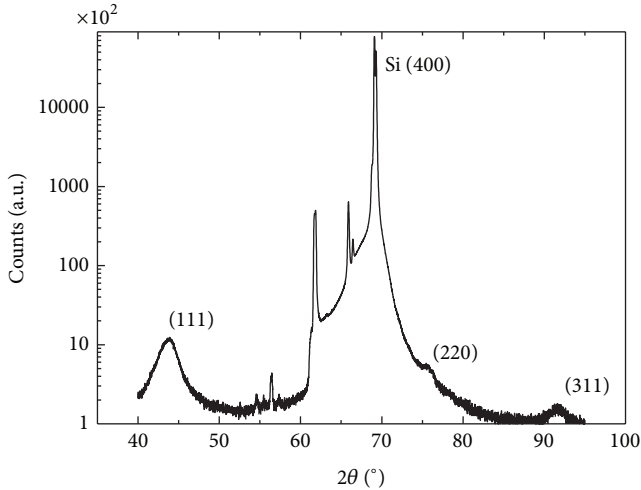


FIGURE 3: XRD measurement with copper anode (1.5444 Å) on a 1 μm thick UNCD film, with average grain size of 5 nm.

In Figure 3, a typical measurement for an UNCD film is presented.

The measurement was done using a standard Bragg-Brentano geometry and a Cu Kα X-ray source. The three diamond peaks at  $2\theta = 43.9^\circ$  (111),  $75.2^\circ$  (220), and  $91.4^\circ$  (311) are clearly detectable. The (100) orientated silicon substrate leads to a peak at  $69^\circ$  and additionally some small peaks on the left side of the silicon (400) peak are detected, caused by the not perfectly monochromatic X-ray source.

The average grain size is in the range of 4 to 6 nm, as measured by XRD. The full width at half maximum of the (111) peak was fitted and the grain size was determined by applying Scherrer's equation.

To further analyze the grown films, texture measurements were done. In order to obtain pole figures for the (111) peak, the  $\theta$  and  $2\theta$  angles were kept constant at  $\theta = 21.95^\circ$  and  $2\theta = 43.9^\circ$ . Then the sample was rotated around its surface normal and, for each rotation angle  $\phi$ , the intensities were measured. Furthermore, the sample was tilted against the beam and detector plane and for each tilt angle  $\psi$  the diffraction intensities are recorded. The measured pole figure of the (111) peak is presented in Figure 4. Peaks at a tilt angle of  $\psi = 35^\circ$  would indicate a (110) fiber texture; a sharp peak at tilt angle  $\psi = 0^\circ$  would indicate a (111) texture.

This measurement shows that the grains in our UNCD films (which were grown thinner than 2 μm only) have no significant preferred orientations.

**2.1. Electrical Characterization.** The specific resistivity of different UNCD microstructures was measured by using the Van-der-Pauw method. Therefore, clearly defined rectangular geometries were etched out of the diamond film. Furthermore, ohmic metal contacts (Ti adhesion layer and Au) were deposited by using sputtering. The specific resistivity reaches values from  $1 \times 10^3 \Omega\text{cm}$  up to  $5 \times 10^{-3} \Omega\text{cm}$  on highly conductive samples.

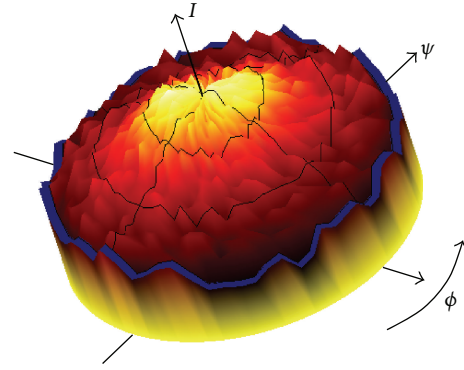


FIGURE 4: Pole figure of the (111) peak.

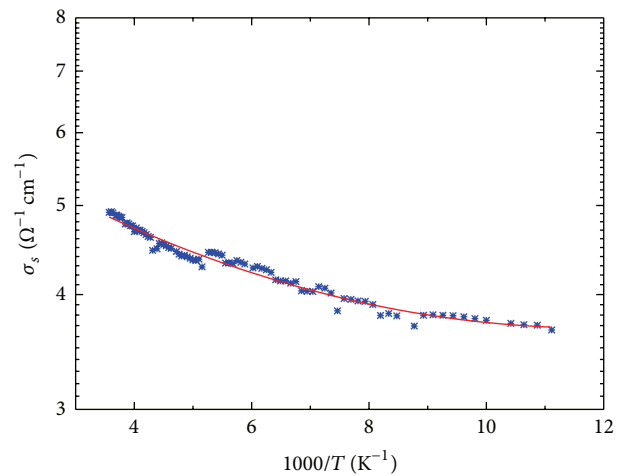


FIGURE 5: Specific conductivity depending on the temperature between  $-200^\circ\text{C}$  and RT.

To verify activation energies, temperature dependent measurements were done. In the first experiment, the specific conductivity was measured at low temperatures, as demonstrated in Figure 5. The sample with a conductivity of about 5 S/cm at room temperature was cooled down to  $-200^\circ\text{C}$  under vacuum conditions, while the conductivity was measured.

In the second experiment, which is shown in the Arrhenius plot in Figure 6, a sample was heated up to  $900^\circ\text{C}$ . This is also done under high vacuum conditions, to avoid oxidation of the diamond at temperature above  $500^\circ\text{C}$ , while again the conductivity was measured.

Over the whole temperature range, from  $-200^\circ\text{C}$  to  $900^\circ\text{C}$ , the specific conductivity increases, like in negative temperature coefficient thermistors. At low temperatures no freeze-out can be detected. In [8] similar measurements show even at 4.2 K no freeze-out, which is in contrast to conventional semiconductor definition. The slopes in the Arrhenius plot in Figure 5 indicate very low activation energies in the range of single meV, assuming constant mobility. The nonlinearity in comparison with a non-freeze-out process indicates electronic states caused by the  $\pi$  bonds of carbon in the grain boundary, which lead to the conductivity in

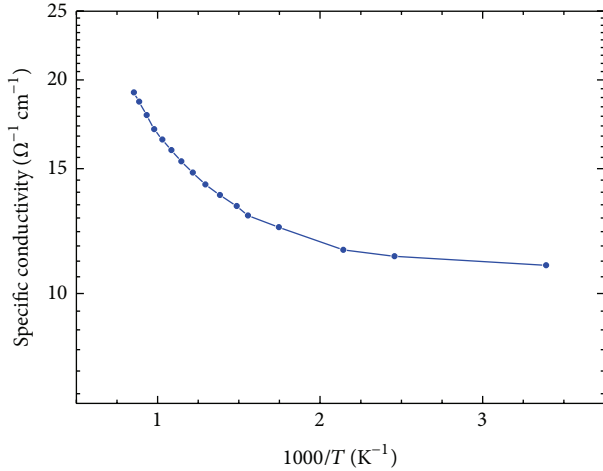


FIGURE 6: Conductivity depending on temperature between RT and 900°C.

the diamond films. That is also assumed in several other publications [8, 11, 14].

The high temperature measurement, shown in Figure 6, demonstrates an amazing potential over conventional semi-conductors. In the temperature range from RT up to about 400°C the change in conductivity is lower and follows the trend of the first measurement. Above 400°C the conductivity increases faster. Under the same assumption, of constant mobility, the corresponding activation energies are about 50 meV–150 meV. It indicates electronic states which are activated with increasing temperature but cannot be directly associated with an activation of further donors.

**2.2. Metallization.** To investigate electrical contacts on the UNCD surface, transmission-line-method (TLM) measurements were used. This commonly used technique [15] allows a quantitative characterization of different contact materials by the contact resistance  $R_C$ . Another good measure for the quality of the metal contact is the transfer length  $L_T$  (which is the length under the metal contact, where the current in the film is reduced by  $1/e$ , due to the currents into the metal contact). Since the contact resistance is not independent of the sheet resistance  $R_{SC}$ , we present also the ratio of contact resistance and sheet resistance.

For its noble character and low specific resistivity, gold is often the choice for metallization of electronic elements. On the other hand, in order to achieve good adhesion and ohmic contact behavior, it is beneficial to have a carbide forming adhesion promoter between the diamond surface and gold.

Different contact metals were tested: molybdenum, titanium, tantalum, and a titanium tungsten alloy ( $Ti_{0.8}W_{0.2}$ ). A summary of TLM measurement results is shown in Table 1. All carbide forming metals showed ohmic behavior in the voltage range of  $\pm 40$  V. Titanium and tantalum have shown significantly better electrical properties than molybdenum and the  $Ti_{0.8}W_{0.2}$  alloy. In [16] different types of carbides are mentioned, with their different electronegativity and atom radius. The interstitial carbide, one special type of carbide

TABLE 1: Results from TLM various measurements on CNCD samples of different conductivity.

Material	$R_C$ [ $\Omega$ ]	$R_{SC}$ [ $\Omega$ ]	$L_T$ [ $\mu\text{m}$ ]	$R_C/R_{SC} \cdot 100$
Mo	402	$18 \cdot 10^3$	4.38	2.21
Ti	6	1305	0.86	0.43
Ta	3	2488	0.28	0.15
TiW	1000	$575 \cdot 10^3$	3.48	1.74

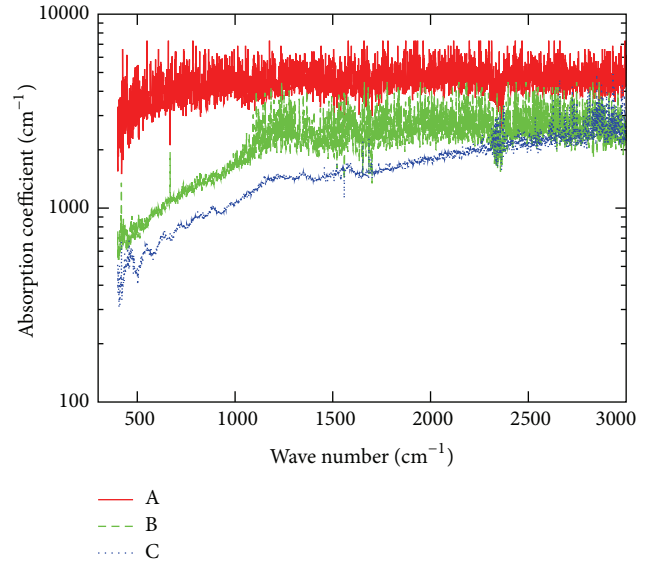


FIGURE 7: Transmission spectra.

with particularly good electrical properties, can only be found for titanium and tantalum.

Resulting from this, titanium and tantalum are suitable materials as ohmic contact material on UNCD, which was also shown for other kinds of conductive diamonds, as shown, for example, in [17, 18]. To improve the temperature stability of the metal contact it is necessary to reduce diffusion of the titanium in gold. That can be done by a diffusion barrier between gold and titanium. Platinum is an appropriate candidate, which was also generally shown in [19]. This also leads to ohmic behavior and to a temperature stability of up to the melting point of gold.

### 3. Spectroscopic Investigations

**3.1. Optical Properties.** Three thick UNCD films (20  $\mu\text{m}$  thick) were grown with different  $NH_3$  concentration in the feed gas, to achieve three different conductivities.

By etching the Si substrate in KOH, free standing UNCD films were obtained. They were measured by Fourier transformation infrared spectroscopy (FTIR). Assuming that Lambert-Beer's law can be applied, the absorption coefficient was calculated. The spectra are shown in Figure 7.

Sample A has a conductivity of 3.7 S/cm at room temperature, sample B has a conductivity of 1.1 S/cm, and sample C has a conductivity of 0.16 mS/cm, as measured by simple four-point measurements [20].

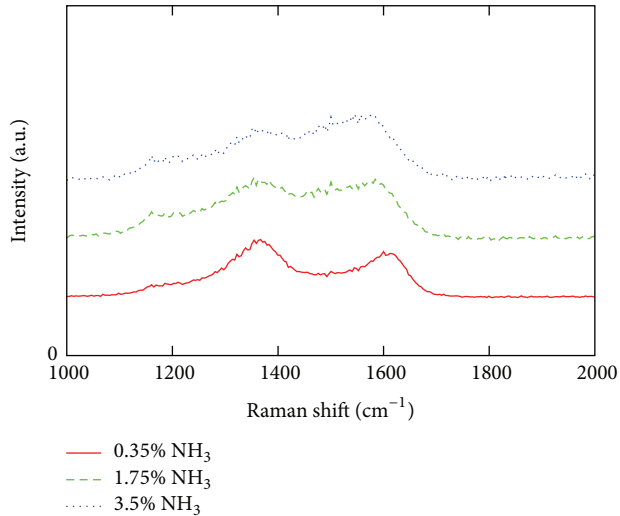


FIGURE 8: Spectra for different  $\text{NH}_3$  concentrations in the feed gas.

It can clearly be seen that, for the sample A, with the highest conductivity, nearly no transmission is found in the measured range.

The coordination of carbon atoms in grain boundaries is generally reduced [21]. Therefore  $sp^2$  and  $sp^3$  bonds coexist in the grain boundaries of diamond, together with impurity atoms (e.g., nitrogen). This distorted  $sp^3$  bonds and the coexisting  $sp^2$  bonds in the grain boundaries lead to band tailing and the appearance of  $\sigma^*$  states (origin from distorted  $sp^3$  bonds and dangling bonds) [14] as well as  $\pi$  and  $\pi^*$  bands (origin from  $sp^2$  bonded carbons) [11, 14], which are responsible for the absorption at these low energies [14, 22, 23].

We see that the absorption edge shifts to lower wave numbers (higher wave lengths) for a higher conductivity of the film. It can be concluded that the  $\pi$  and  $\pi^*$  bands are broader for samples with higher conductivity [14].

**3.2. Raman Spectroscopy.** Raman spectra were measured for three films that were grown with different ammonia addition. The excitation wavelength was 543 nm. The spectra can be seen in Figure 8. A linear background was subtracted from all spectra. We can see the D-band at  $1360\text{ cm}^{-1}$  and the G-band at  $1560\text{ cm}^{-1}$ . The diamond peak at  $1333\text{ cm}^{-1}$  cannot be seen due to its smaller Raman cross section [24, 25]. Therefore only the chemical constitution and structure of the grain boundaries are reflected by measurements.

The D- and G-band peaks were fitted using Lorentzian functions, revealing the intensities and full width at half maximum (FWHM) of each.

The electrical conductivities of these films were also determined by four-point measurements and these results are given in Table 2 together with the results of the Raman measurements.

Following argumentation in [25–27], the increasing FWHM of the G-band and the decreasing ratio of D-band intensity to G-band intensity  $I(D)/I(G)$  indicates an increase of structural disorder of the  $sp^2$  bonded carbon. Therefore, we

TABLE 2: Parameters, found by fitting Lorentzian curves in the measured Raman spectra.

$\text{NH}_3$ (%)	FWHM (G) ( $\text{cm}^{-1}$ )	$I(D)/I(G)$	$\sigma$ (S/cm)
0.35	56.2	1.37	0.2974
1.75	104.5	1.08	0.0113
3.5	125.3	0.72	0.0004

conclude that, for higher amount of  $\text{NH}_3$  addition to the feed gas, the disorder of the grain boundaries increases, leading to a reduction of conductivity. This relation between disorder of grain boundary and conductivity is in agreement with investigations on plasma CVD grown nitrogen doped UNCD films [13, 28].

## 4. Summary

We presented ultrananocrystalline diamond thin films with tuneable electrical n-type conductivity from practically isolating ( $1 \times 10^{-3}$  S/cm) to 200 S/cm. This conductivity is present and only varies slightly over a large temperature range ( $-200^\circ\text{C}$  until  $900^\circ\text{C}$  was measured). A system for electrical contact metallization is shown, which is of importance for general characterization and application of the films in electrical or electromechanic devices. Our electrical measurements confirm that the conductivity is of n-type [10] and together with the spectroscopic measurements we conclude that the conductivity is due to the structure and volume of the grain boundary.

## Conflict of Interests

The authors declare that there is no conflict of interests regarding the publication of this paper.

## Acknowledgment

The authors gratefully acknowledge the financial support by the German ministry of education and research (BMBF) through VDI/VDE-IT, within the projects C-Hybrid (FKZ 16SV5320K) and VIP-DiM (FKZ 16SV6503).

## References

- [1] H. J. Fecht and M. Werner, *The Nano-Micro Interface—Bridging the Micro and Nano Worlds*, Wiley-VCH, 2004.
- [2] H.-J. Fecht, K. Brühne, and P. Gluche, Eds., *Carbon-based Nanomaterials and Hybrids—Synthesis, Properties, and Commercial Applications*, Pan Stanford, Singapore, 2014.
- [3] M. Werner, M. Adamschik, P. Gluche, E. Kohn, and H.-J. Fecht, “Review on diamond based piezoresistive sensors,” in *Proceedings of the IEEE International Symposium on Industrial Electronics (ISIE ’98)*, vol. 1, pp. 147–152, July 1998.
- [4] M. Dipalo, J. Kusterer, K. Janischowsky, and E. Kohn, “N-type doped nano-diamond in a first MEMS application,” *Physica Status Solidi A*, vol. 203, no. 12, pp. 3036–3041, 2006.
- [5] R. Kalish, “The search for donors in diamond,” *Diamond and Related Materials*, vol. 10, no. 9-10, pp. 1749–1755, 2001.

- [6] R. Kalish, "Diamond as a unique high-tech electronic material: difficulties and prospects," *Journal of Physics D: Applied Physics*, vol. 40, no. 20, pp. 6467–6478, 2007.
- [7] J.-P. Lagrange, A. Deneuve, and E. Gheeraert, "Activation energy in low compensated homoepitaxial boron-doped diamond films," *Diamond and Related Materials*, vol. 7, no. 9, pp. 1390–1393, 1998.
- [8] S. Bhattacharyya, O. Auciello, J. Birrell et al., "Synthesis and characterization of highly-conducting nitrogen-doped ultrananocrystalline diamond films," *Applied Physics Letters*, vol. 79, no. 10, pp. 1441–1443, 2001.
- [9] O. A. Williams, S. Curat, J. E. Gerbi, D. M. Gruen und, and R. B. Jackman, "*n*-type conductivity in ultrananocrystalline diamond films," *Applied Physics Letters*, vol. 85, no. 10, pp. 1680–1682, 2004.
- [10] N. Wiora, M. Mertens, M. Mohr, K. Brühne, and H.-J. Fecht, "Synthesis and characterization of *n*-type nitrogenated nanocrystalline diamond," *Micromaterials and Nanomaterials*, vol. 15, no. 96–98, pp. 1619–2486, 2013.
- [11] P. Zapol, M. Sternberg, L. A. Curtis, T. Frauenheim, and D. M. Gruen, "Tight-binding molecular-dynamics simulation of impurities in ultrananocrystalline diamond grain boundaries," *Physical Review B—Condensed Matter and Materials Physics*, vol. 65, no. 4, Article ID 045403, 2001.
- [12] J. Birrell, J. A. Carlisle, O. Auciello, D. M. Gruen, and J. M. Gibson, "Morphology and electronic structure in nitrogen-doped ultrananocrystalline diamond," *Applied Physics Letters*, vol. 81, no. 12, pp. 2235–2237, 2002.
- [13] T. Ikeda, K. Teii, C. Casiraghi, J. Robertson, and A. C. Ferrari, "Effect of the  $sp^2$  carbon phase on *n*-type conduction in nanodiamond films," *Journal of Applied Physics*, vol. 104, no. 7, Article ID 073720, 2008.
- [14] P. Achatz, J. A. Garrido, M. Stutzmann et al., "Optical properties of nanocrystalline diamond thin films," *Applied Physics Letters*, vol. 88, no. 10, Article ID 101908, 2006.
- [15] G. K. Reeves and H. B. Harrison, "Obtaining the specific contact resistance from transmission line model measurements," *IEEE Electron Device Letters*, vol. 3, no. 5, pp. 111–113, 1982.
- [16] H. O. Pierson, *Handbook of Refractory Carbides and Nitrides*, Noyes Publications, 1996.
- [17] K. Das, V. Venkatesan, K. Miyata, D. L. Dreifus, and J. T. Glass, "A review of the electrical characteristics of metal contacts on diamond," *Thin Solid Films*, vol. 212, no. 1-2, pp. 19–24, 1992.
- [18] K. Das, V. Venkatesan, K. Miyata, D. L. Dreifus, and J. T. Glass, "A review of the electrical characteristics of metal contacts on diamond," *Thin Solid Films*, vol. 212, no. 1-2, pp. 19–24, 1992.
- [19] T. C. Tisone and J. Drobek, "Diffusion in thin film Ti–Au, Ti–Pd, and Ti–Pt couples," *Journal of Vacuum Science and Technology*, vol. 9, no. 1, pp. 271–275, 1972.
- [20] L. Valdes, "Resistivity measurements on germanium for transistors," *Proceedings of the IRE*, vol. 42, no. 2, pp. 420–427, 1954.
- [21] P. Koblinski, D. Wolf, S. R. Phillpot, and H. Gleiter, "Role of bonding and coordination in the atomic structure and energy of diamond and silicon grain boundaries," *Journal of Materials Research*, vol. 13, no. 8, pp. 2077–2099, 1998.
- [22] O. A. Williams, "Nanocrystalline diamond," *Diamond and Related Materials*, vol. 20, no. 5-6, pp. 621–640, 2011.
- [23] M. Nesládek, K. Meykens, L. M. Stals, M. Vaněček, and J. Rosa, "Origin of characteristic subgap optical absorption in CVD diamond films," *Physical Review B*, vol. 54, no. 8, pp. 5552–5561, 1996.
- [24] S. R. Sails, D. J. Gardiner, M. Bowden, J. Savage, and D. Rodway, "Monitoring the quality of diamond films using Raman spectra excited at 514.5 nm and 633 nm," *Diamond and Related Materials*, vol. 5, no. 6–8, pp. 589–591, 1996.
- [25] F. Klauser, D. Steinmüller-Nethl, R. Kaindl, E. Bertel, and N. Memmel, "Raman studies of nano- and ultra-nanocrystalline diamond films grown by hot-filament CVD," *Chemical Vapor Deposition*, vol. 16, no. 4–6, pp. 127–135, 2010.
- [26] A. C. Ferrari and J. Robertson, "Raman spectroscopy of amorphous, nanostructured, diamond-like carbon, and nanodiamond," *Philosophical Transactions of the Royal Society A*, vol. 362, no. 1824, pp. 2477–2512, 2004.
- [27] A. C. Ferrari and J. Robertson, "Origin of the 1150  $cm^{-1}$  Raman mode in nanocrystalline diamond," *Physical Review B: Condensed Matter and Materials Physics*, vol. 63, no. 12, Article ID 121405, 2001.
- [28] J. Birrell, J. E. Gerbi, O. Auciello, J. M. Gibson, D. M. Gruen, and J. A. Carlisle, "Bonding structure in nitrogen doped ultrananocrystalline diamond," *Journal of Applied Physics*, vol. 93, no. 9, pp. 5606–5612, 2003.